Multimaterial Fiber Sensors for Physical Measurements

Ruixuan Wang

Dissertation submitted to the faculty of the Virginia Polytechnic Institute and State University in partial fulfillment of the requirements for the degree of

Doctor of Philosophy
in
Electrical Engineering

Anbo Wang, Chair
Gary R. Pickrell
Marius K. Orlowski
Xiaoting Jia
Yizheng Zhu

August 8th, 2024
Blacksburg, Virginia

Keywords: Optical Fiber Sensors, Multi-material Fiber, Strain Sensing, Electromagnetic Sensing

Multimaterial Fiber Sensors for Physical Measurements

Ruixuan Wang

Abstract

Polymer fiber sensors have been extensively explored over the past few decades for biomedical, structural health monitoring, and environmental monitoring applications. Their low melting point and well-established processing methods make them easily integrable with other materials, such as metals, semiconductor devices, and composites, to create multimaterial sensors with versatile sensing capabilities. However, the high viscoelasticity of polymer materials and the limitations of existing sensing mechanisms constrain the precision and stability of these sensors. This research focuses on enhancing the sensitivity of multimaterial polymer sensors by improving both the sensing mechanisms (chapter 2 and 3) and sensor structures (chapter 4 and 5).

Chapters 2 and 3 discuss the integration of silica optical fiber sensors into magnetostrictive composite materials for distributed magnetic field sensing. A series of Fiber Bragg Gratings (FBGs) were inscribed in the core of a silica fiber, which was then thermally embedded at the center of a magnetostrictive composite made of Terfenol-D and thermoplastic elastomers. The magnetostrictive properties of the composite, using various polymer matrices, were thoroughly investigated. A detailed study of the sensor's response under different boundary conditions and applied tensions demonstrated its tunable frequency response and bandwidth capabilities. Furthermore, the sensor's magnetic field sensing performance was characterized under applied AC magnetic fields, showing a responsivity of up to 4.5 ppm/mT and a resolution of 0.1 mT.

Theoretical modeling of the magnetostrictive fiber's behavior was also conducted, with the strain transfer coefficient being calculated and compared to the bulk material's response. This thermally drawn magnetostrictive fiber exhibits significant potential for fully distributed sensing applications.

In Chapters 4 and 5, the development of a stretchable fiber strain sensor is presented, with improvements in sensitivity achieved through structural optimizations. Polymer fibers, known for their high stretchability, flexibility, and softness, are promising candidates for sensing applications. However, their high viscoelasticity often leads to significant hysteresis. To address this, a double-coil strain sensor was introduced in this research. A theoretical model of the double-coil capacitance was developed to inform future sensor designs. Based on this model, a stretchable miniature fiber sensor was constructed, featuring a stretchable core tightly coiled with parallel conductive wires. This sensor demonstrated low hysteresis, a theoretical resolution of 0.015%, a response time of less than 30 milliseconds, and outstanding stability after more than 16,000 cycles of testing. Its potential as a wearable device was showcased by embedding it into belts, gloves, and knee protectors, with applications ranging from bladder monitoring to life safety rope systems.

The dissertation concludes with a discussion of the research findings and suggestions for future directions in the development of multimaterial fiber sensors.

Multimaterial Fiber Sensors for Physical Measurements

Ruixuan Wang

General Audience Abstract

This research focuses on enhancing the sensitivity of polymer fiber sensors, which are widely used in healthcare monitoring, infrastructure safety, and environmental observation. These sensors offer the advantage of integrating with other materials to create versatile, multi-functional devices. However, their soft nature and limited sensing mechanisms pose challenges to measurement accuracy and stability. This dissertation proposes improvements in the sensitivity of multimaterial polymer fiber sensors by enhancing both their sensing mechanisms and structural designs.

In the first part, new techniques were developed to improve magnetic field sensing by embedding optical fibers into magnetically responsive materials. A scalable method called thermal drawing was used to fabricate magnetostrictive fibers, enabling the sensors to measure magnetic fields at various locations with a minimum detectable change of 0.1 mT. This approach enhances the accuracy of magnetic field detection, which is valuable for monitoring magnetic field distributions in industrial applications.

The second part introduces a stretchable sensor designed for strain detection in wearable, biomedical, and structural health monitoring applications. Featuring a double-coil design, this sensor demonstrated stability, durability, and accuracy in real-time monitoring by detecting changes in relative capacitance.

Overall, this research offers significant insights into improving the reliability and effectiveness of polymer fiber sensors, paving the way for future innovations in smart sensing technologies. The dissertation concludes with a discussion of potential improvements and future research directions.

To my Family

To my grandparents, parents, and husband,

Your unconditional support and understanding,

Your encouragement, steadfast and strong,

Made this work possible, shaped who I am today.

Acknowledgements

First and foremost, I would like to express my sincere gratitude to my advisor, Dr. Anbo Wang, for his guidance, patience, and selfless dedication to my research. Dr. Wang not only shared his knowledge of optical fiber sensing but also taught me how to seek the right answers and continuously improve myself. He always encouraged me to "keep my mind open" and to explore the world with curiosity. Thanks to his guidance, patience, and the freedom he provided in my research directions, I was able to explore a broad range of topics from multiple perspectives. The Ph.D. journey is never an easy one, and I am deeply thankful for his support and direction, especially during times when I felt disoriented.

I would also like to thank Dr. Xiaoting Jia, Dr. Gary Pickrell, Dr. Yizheng Zhu, and Dr. Mariusz Orlowski for serving as my committee members. I am grateful for their guidance and encouragement throughout my Ph.D. journey. I want to express special thanks to Dr. Jia for her guidance on my work with multimaterial fiber sensors. Dr. Jia not only shared her expertise in this field and helped me secure the resources needed for experiments but also consistently supported and encouraged me during my research at Virginia Tech. Her passion and optimism have been a source of inspiration during challenging times. I would also like to express my special gratitude to Dr. Yizheng Zhu, Dr. Daniel Homa, Yong Xu, and Dr. Gary Pickrell from Center for Photonics Technologies (CPT) for their guidance and assistance on the projects we worked on and my own research topics.

My gratitude also goes to my friends and colleagues that I have been working with in CPT. I would like to thank Dr. Jiaji He, Dr. Shuo Yang, Dr. Bo Dong, Dr. Li Yu, Dr. Tong Qiu, Mr. Logan Theis, and Dr. Qingzhao Kong from Dr. Anbo Wang's group. Over the past years, I have worked closely with them, and I am very grateful for their help. I would like to express special thanks to Dr. Shuo Yang, Dr. Jiaji He, and Mr. Logan Theis for their tremendous help with my research. As senior students in the group, Dr. Shuo Yang and Dr. Jiaji He provided invaluable assistance in helping me take my first steps in my Ph.D. work and generously shared their experiences on how to conduct research. Mr. Logan Theis offered great guidance on both the ONR projects we worked on together and provided numerous suggestions for my own research. He not only shared his expertise in the field of optical fiber sensors but also encouraged and inspired me. I would like to extend my gratitude to Dr. Yujing Zhang, Dr. Shan Jiang, Dr. Ziang Feng, Dr. Jongwoon Kim, Mr. Hengji Huang, and Ms. Yue Liu from Dr. Xiaoting Jia's group. I am particularly thankful to Dr. Yujing Zhang and Dr. Ziang Feng for their patient and detailed guidance in teaching me how to draw fibers; I could not have accomplished this work without their tremendous help. Additionally, Yujing and I have not only been colleagues but also good friends throughout our daily lives. I appreciate her for sharing both knowledge and joy with me during my Ph.D. journey. I also want to thank Mr. Guannan Shi, Mr. Jacob Black, and Mr. Joseph Thomas from Dr. Yizheng Zhu's group, as well as Dr. Zachery Hillemann, Dr. Hanna Heyl, Mr. Steven Sinder, and Mr. Zachry Dejneka from Dr. Gary Pickrell's group for their numerous discussions and assistance with my research. For the projects I worked on, I am grateful to the co-workers and co-authors who contributed significantly. In the sub-surface thermal measurement project, I thank Dr. Zhenyu Kong, Dr. Rongxuan Wang, and Mr. Chaoran Dou from the Industrial and Systems Engineering Department for their support. For the stretchable fiber sensor project, I appreciate Dr. Michael Rein, Dr. Alexander Stolyarov from AFFOA, Ms. Junru Zhang, Dr. Blake N. Johnson, Dr. Gary D. Siedel, Dr. Michael Philen, Dr. Carson Squibb, and Mr. Viswajit Talluru from the ASML lab, Dr. Thomas Staley from the MSE department, and Mr. William Whitman from Teufelberger. Their contributions were crucial to the success of this project.

Many thanks to the friends I met in this beautiful little town of Blacksburg and through my journey in the US: Ms. Meitong Nie, Dr. Kaiwen Chen, Dr. Mo Hu, Dr. Yunwei Ma, Dr. Shaoran Li, Dr. Xuejiao Ma, Dr. Feng Jin, Ms. Shuangshuang Pan, Dr. Yixuan Dou, Dr. Liyan Zhu, Dr. Siwen Wang, Dr. Feiyang Zhu, and many others. I apologize if I missed anyone's name. I would like to extend special thanks to Ms. Yan Pu, who has provided me with tremendous warmth and made me feel at home in this small town. Her kindness, warmth, and optimism have been a great comfort, and I feel fortunate to have met her. Her wisdom and positive spirit will continue to inspire me even after I leave Blacksburg.

I would also like to thank my colleagues from my internship at Apple. I am grateful for their guidance and encouragement. The time I spent in California was a significant experience during my Ph.D. journey, and the inspiring experiences in the industry provided valuable insights.

Moreover, I would like to express my gratitude to my family. I feel incredibly fortunate that my Ph.D. studies in Blacksburg led me to meet my husband, Shuo Wang. He has been my strongest support throughout this journey, and we have shared many joyful moments in this beautiful and peaceful town. As a fellow Ph.D. student, Shuo has been invaluable in sharing his experiences and offering guidance on my academic and career paths. As my husband, he has always supported the decisions I've made in life. I also would like to express my gratitude to my in-laws for their support! Last but certainly not least, I would like to thank my grandparents and parents. They have shaped my ideas, supported my decisions, and guided me to make all this possible. The warmth and kindness my family has given me are priceless treasures that will continue to enrich my life forever.

Table of Contents

List of Figures

List of Tables

Chapter 1 Introduction

1.1 Overview of Optical Fiber Sensors and Motivations

Invention of optical fibers dates back to late 19th century, but the surge of the optical fiber development and widely commercialized applications happened in 1960s after Charles K. Kao and George A. Hockman from the Standard Telephone and Cables reduced the attenuation of the optical fibers to less than 20 dB/km. After that, high quality optical fibers have been used in the modern telecommunication field to make fast internet connections possible [1]. Nearly at the same time, the development of optical sensors also moves to the field of guided-wave optical sensors in the late 1960s. A work reported in a NATO work first proposed the title of 'Optical Fiber Sensors' [2].

After years of development of optical fiber sensors, optical fiber sensors have found applications in various fields such as telecommunications, medical diagnostics, structural health monitoring, safety warning, and industrial automation. [3–9]. Comparing with the traditional semiconductor-based sensors, optical fiber sensors exhibit several advantages: First, the dielectric fiber materials (usually silica for telecommunication fibers) are chemically inert, this make them suitable for harsh environment where chemical reactions exist, and the environment is corrosive. Second, the dielectric nature of the optical fiber sensor also makes it immune to electromagnetic interference. In addition, unlike semiconductor sensors, optical fiber sensors don't generate electric sparks. With both advantages, optical fiber sensors can be used in high voltage high power environments and cases with the risk of explosion. Third, the size of the optical fibers is miniature, usually in the order of $\sim 100\ \mu m$, where microfibers have even smaller cross-sectional area. In addition to the biocompatibility of fiber material, the optical fiber sensors have minimum interference with the point of measurements. Nowadays, especially after the development of multimaterial fibers, the optical fiber sensor is suitable for biomedical applications. Fourth, with silica as the main material, the optical fiber sensors have very high fusion point. Optical fiber sensors can survive in harsh high temperature environment. The temperature sensing range can even be extended with the development of the sapphire optical fiber sensors [10–12]. Fifth, the compact size and lightweight nature of optical fiber sensors provide a significant advantage when integrating or deploying them on a large scale. Sixth, the extremely low transmission loss of optical fiber sensors makes them ideal for remote sensing applications, allowing interrogation systems to be located far from harsh environments. Seventh, the high stability of silica material and the reliability of optical fiber sensors make them excellent candidates for structural health monitoring, where they can be embedded for long-term measurements. Eighth, optical fiber sensors offer high precision and distributive sensing capabilities. Optical fiber sensors are potentially higher sensitivity, a larger dynamic range, and higher resolution compared to traditional sensors. By leveraging interferometric techniques, optical fiber sensors can surpass the sensitivity limits of conventional sensors. Most importantly, optical fiber sensors uniquely offer multiplexing and distributed sensing capabilities. With advances in interrogation systems and sensing principles, a single optical fiber can cover extended sensing lengths and a large number of sensing points—an ability unmatched by traditional sensors and a key focus in optical fiber sensing research. [13–17]

However, optical fiber sensors also have some disadvantages. First, their high sensitivity can lead to issues with crosstalk from undesired measurands, such as the interference between strain and temperature measurements. Addressing and demodulating these crosstalk issues has been a significant area of research, with considerable progress made in this field. Second, the cost of optical fiber sensors is generally higher than that of traditional sensors. This is a common challenge for optical-based sensors, and optical fiber sensors often require specialized interrogation systems, which can further increase the overall cost of the sensor system. [2].

While these two disadvantages have long been recognized and are continually being addressed within the field, there is another area where traditional optical fiber sensors could be enhanced. Most optical fiber sensors today are made from silica or doped silica and are primarily used for physical measurements, such as temperature and strain. The silica material is chemically inert and has a high Young's modulus, which presents several limitations:

1. **Limited Interaction:** The interaction between the measured parameters and the light propagated within the silica fiber is limited. As a result, functionalizing the optical fiber is essential for expanding its applications.
2. **Limited Flexibility and Stretchability:** The high Young's modulus of silica restricts the flexibility and stretchability of these sensors. Although these properties are not typically required in traditional sensing scenarios, there is a growing demand for 'wearable' and 'stretchable' sensors.

To meet these emerging needs, new materials and structures must be developed that offer greater flexibility and functionality. In this dissertation, we address the limitations of traditional silica optical fiber sensors by introducing enhancements through the development of multimaterial optical fiber sensors. To expand their sensing capabilities, we employed a thermal drawing process that enables silica optical fibers to be thermally co-drawn with multimaterial polymer layers. This approach adds flexibility and functionality while retaining the inherent advantages of commercially available silica fibers. Additionally, we developed a new multimaterial fiber design that balances stretchability with sensitivity, making it suitable for wearable and implantable applications. By adopting this 'multimaterial' fiber approach, we demonstrated that these new designs could meet the demands of specialized sensing applications that traditional optical fiber sensors cannot.

1.2 Principles of Optical Sensing

Under the realm of optical fiber sensing, there are multiple sensing mechanisms that have been adopted. Here, we will briefly cover some of the most common ones to give a general overview of optical fiber sensor technologies and then follow by a dive into the introduction of optical fiber Bragg Gratings as it is the sensor that has been used in this dissertation work.

1.2.1 Point Sensors Overview

Intensity based transduction measurements are one of the first techniques that was used in the field of optical fiber sensing. There are several sensing techniques based on this principle. The first is microbends and macrobaneds. In this case, single mode or multimode fiber or multimode fiber are forced to deform under external compressions. The mode profile mismatch and the exit of the guided light entering the cladding will cause transmitted power loss. With this mechanism [18], the sensor can be used to measure displacement by tracking the movement of the one of the microbenders, pressure by attaching membrane to one of the microbenders [18,19], strain, vibration, temperature and humidity [19–21]. This intensity-based sensor has simple schematics and potentially low cost. However, it suffers from the disadvantage of high crosstalk and performance is dependent on the modal profile of the light source. The second direction of the intensity-based sensor is evanescent field measurement. To have the guided wave penetrate the media under testing, the evanescent field sensor is side-polished, cladding removed or tapered to allow more field getting into the surround field. The evanescent field sensor has been widely used for the application based on refractive index sensing, including chemical sensing, PH and humidity sensing [22–26]. Other intensity-based measurements include coupling based transducers where the light from one optical fiber exit its end face and interact with the measurand and then enter another fiber which served as the 'receiver' [27–29], encoding-based position sensors and so on.

While intensity-based measurements are straight-forward and potentially low-cost, it does not fully show the advantage of the optical sensing since it doesn't take the fully advantage of the wave properties of the optical sensing. Interferometry and polarimetry are the sensing mechanisms that have been used widely for optical sensing applications and show high precisions. Common optical fiber interferometers include the Michealson Interferometer, Mach-Zehnder Interferometer, Sagnac Interferometer and Fabry-Perot Interferometer. Although each interferometer has different schemes, their sensing mechanism is based on the changing phase difference due to the external conditions. For simplicity, let consider a 2-beam interferometer as an example for demonstration:

If the two beam were approximated by two plane waves E_1 and E_2 respectively, the fields are:

$$E_i = A_i \exp(j\phi_i)\,, (i = 1,2) \tag{1-1}$$

The intensity of the interference is:

$$I = |E_1 + E_2|^2 = A_1^2 + A_2^2 + 2A_1A_2\cos(\phi_1 - \phi_2) \tag{1-2}$$

If the optical path difference between the two optical path is $L_{OPD} = nl$ where n is the refractive index and l is the path difference, the phase difference is given by:

$$\phi(\lambda) = 2\pi nl \tag{1-3}$$

The relationship of the measured intensity can be simplified and rewritten as:

$$I(\lambda) = k[1 - Vcos(\phi)] \tag{1-4}$$

With the change of the phase due to the applied measurand, the intensity of the inference signal will be observed. The monotonic changes on the intensity will be observed if the interference signal is between the maximum and minimum cycle. However, a single wave tracking like what is shown in the above equation will leads to phase ambiguities since the interferometer will differentiate between the signals with 2π phase differences. Increasing the wavelength interrogation from single to multiple to broad wavelength interrogations will increase the sensor's phase measurements robustness and demodulation of the interferometer phase without a continuous tracking of the interference signal [2,30,31].

The sensing mechanism of a polarimetric sensor can be analogous to a two-beam interferometer. For a linear polarized source, it can couple to two polarization eigenmodes of the linear birefringent fiber. The phase difference between the states will be measurand dependent. After using the polarization analyzer to convert the two states into the common azimuth, the two polarization states will produce interference pattern like the case of two beam interference.

Fiber Bragg Gratings

Another interference related sensing mechanism is optical fiber Bragg grating (FBG) where the refractive index along the core of the optical fiber was spatially periodic modulated. Just like the case Bragg diffractions of x-Rays for atom lattice, the Bragg condition of the optical fiber Bragg grating is:

$$N\lambda_B = 2n_{eff}\Lambda \tag{1-5}$$

Where λ_B is the central wavelength of the reflected central wavelength, n_{eff} is the effective refractive index of the fiber, Λ is the pitch length of the periodic refractive index modulation, and *N* is the integer to represent the order of the grating. The reflectivity of a grating with constant amplitude of index modulation and length of *l* has the reflectivity of [32,33]:

$$R = \frac{\kappa^2 \sinh^2 \psi l}{\Delta k^2 \sinh^2 \psi l + \psi^2 \cosh^2 \psi l} \tag{1-6}$$

Here $\Delta k = k - \pi/\lambda$ is the detuning vector to show the mismatch between the incident wave vector to the Bragg wavelength wavevector. The ψ and coupling coefficient κ is given by:

$$\psi = \sqrt{\kappa^2 - \Delta\kappa^2} \tag{1-7}$$

$$\kappa = \frac{\pi \Delta n \eta}{\lambda} \tag{1-8}$$

Where Δn is the amplitude of the index modulation and η is the grating efficiency, which shows the overlap between the guided optical mode and the grating, and its value is:

$$\eta \approx 1 - \left(\frac{\lambda_0}{2\pi a}\right)^2 \frac{1}{(n_1^2 - n_2^2)} \tag{1-9}$$

Here, λ_0, a, n_1, n_2 are the free space wavelength, fiber core radius, core and cladding refractive index respectively.

Fiber Bragg gratings are both sensitive to strain $\Delta\varepsilon_z$ and temperature ΔT and strains:

$$\Delta\lambda = \lambda\left(\frac{1}{n}\frac{\partial n}{\partial \varepsilon_z} + 1\right)\Delta\varepsilon_z + \lambda(\varsigma + \alpha)\Delta T \tag{1-10}$$

Where $\alpha = \frac{1}{\Lambda}\frac{\partial \Lambda}{\partial T}, \varsigma = \frac{1}{n}\frac{\partial n}{\partial T}$ are the thermal expansion and thermos-optic coefficient respectively. Here the dominant effect is the thermos-optic effect. For silica optical fiber, here are some of the common numbers used for temperature sensing: $\varsigma = 1.1 \times \frac{10^{-5}}{n_{eff}}$ /°C, and $\alpha = 0.5 \times 10^{-6}/°C$.

The variation of the refractive index due to the axial strain is given by Hooker's Law:

$$\frac{1}{n}\frac{\partial n}{\partial \varepsilon_z} = -\frac{n^2}{2}(p_{12} - \nu(p_{11} + p_{12})) \tag{1-11}$$

Where ν is the Poisson's ratio, p_{11}, p_{12} are the strain-optic tensor. The final conversion between the relative center wavelength shift and strain is $\varepsilon = \frac{1.26\Delta\lambda_B}{\lambda_B}$.

1.2.2 Fully Distributive and Quasi-distributive Optical Fiber Sensors

The ability to sense measurands along the fiber length with fully distributive and quasi-distributive manners is the unique advantage of optical fiber sensors. The current distributive sensing sensors can demonstrate 1-2 cm spatial resolution over kilometers of sensing range. This has made the distributive sensors a cost effective and space-effective solution.

The two major working principles of the fully distributive optical sensors are optical time-domain reflectometry (OTDR) and optical frequency domain reflectometry (OFDR). In OTDR, a short optical pulse is launched into the fiber and the continuous Rayleigh back scatterings reflect the light carrying the information of the local strain, temperature, and vibrations. The location information of the measurand is calculated by the time of flight of the forward propagating light, while the spatial resolution of the sensor is decided by the pulse width of the interrogation pulse. However, the decreasing of the pulse width is at the cost of the broadening of the bandwidth and compromise the signal to noise ratio of the sensing signal. According to the Fourier Transform, a short pulse in the time domain is equivalent to a broad frequency domain signal. OFDR, on the other hand, launches continuous frequency modulated optical waves. Here, the spatial resolution is decided by the frequency tuning range.

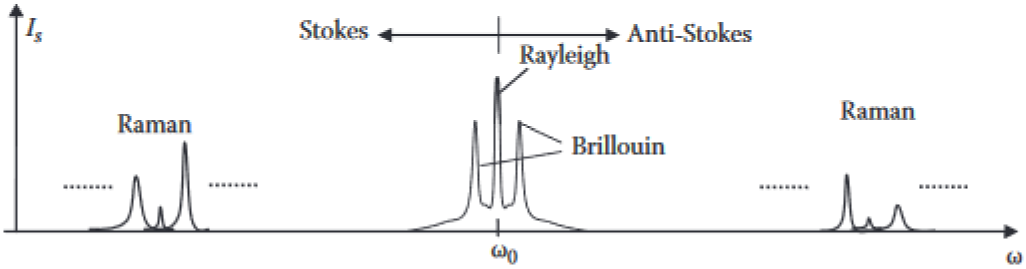

Figure 1-1 Typical spontaneous scattering spectrum in solid-state matter. [32]

For the guided electromagnetic wave, time-dependent polarization dipole can be generated by guided optical waves if it is off-resonance. The secondary scattered electromagnetic wave is called the scattered field. The scattering center in optical fiber rises from the microscopic and macroscopic variations in density, composition and structure defects. There are three types of spontaneous scattering in optical fiber: Rayleigh scattering, Raman scattering, and Brillouin scattering, which are shown in Figure 1-1Figure 1-1 Typical spontaneous scattering spectrum in solid-state matter. [32]. The local dopants and random molecules caused refractive index variations is the origin of Rayleigh scattering. Rayleigh scattering is an elastic scattering effect where the scattered wavelength is the same as the incident wavelength. The lines next to the Rayleigh scatterings are the Brillouin scatterings, which are due to the scattering with the counterpropagating acoustic waves. The downshifted line is called Strokes terms, and the upshifted line is called anti-Strokes terms respectively. The Raman scatterings are due to the molecules' vibrations. The Raman scattering terms are usually broadband with linewidth of THz, and there are several sharp peaks associated with different molecular rotations, reorientation excitations. Since the broadband nature of the Raman scattering peaks, it is hard to differentiate the location information and induced changes. Rayleigh, Raman and Brillouin scatterings based OTDR sensing have been demonstrated, while OFDR sensing requires small spectrum linewidth thus limited the application of Raman based OFDR sensing system. The details of fully distributive sensing can be found in several references [2,34,35], and it is out of the scope of this dissertation thus not covered here.

Quasi-distributive sensing system is another topic for distributive fiber sensing applications. Unlike the fully distributive sensing system, in the quasi-distributive sensing system only prescribed sections are sensitive to the measurand. This applies to the application case that the distance of the sensing locations is known, but the quasi-distributive sensing system allows the customized sensor properties at different locations. Fiber Bragg Grating distributive optical fiber sensors is one of the most widely used examples of the quasi-distributive sensing system. Multiple fiber Bragg gratings can be inscribed in serial and share the same interrogation system. Both the wavelength domain multiplexed FBGs and the time-domain multiplexed FBGs sensing system has been demonstrated over the years [36,37]. In this dissertation, we have demonstrated quasi-distributive magnetic sensing capability by wavelength-multiplexed FBG sensing system.

1.3 Multi Material Fiber Overview

1.4 Overview and Comparisons on Different Methods

As discussed in previous sections, optical fiber sensing systems are highly versatile, offering high precision, stability, and multi-point sensing capabilities. However, the optical fiber itself has a relatively simple composition. Despite the adoption of various polymers and glasses for fiber fabrication, silica remains the predominant material choice. To broaden the sensing capabilities of optical fiber sensors, the concept of multimaterial fibers was introduced. Several strategies have been proposed in this area:

(1) **Thermally Drawn Multimaterial Fiber:** In this approach, materials with distinct optical, electronic, mechanical, and magnetic properties are incorporated into a single preform, which is then monolithically thermally drawn into smaller fibers with complex cross-sectional areas. The traditional high-temperature silica fiber draw tower allows for the melting and integration of these multimaterials into the cladding sections of the optical fiber, while the polymer draw tower can apply functional coatings to the outside of the silica fiber. During the drawing process, the fiber's cross-sectional area is reduced to the micrometer range, and the overall length of the produced fiber can be extended over kilometers.

(2) **Fiber Tip Modifications:** Unsing the nanotechnologies, this method requires the modification of the fiber tip by transferring the photonics chip to the fiber facet [38], direct nano-fabrication with photolithography and electro-beam lithography(EBL) [39], focused Iron Beam (FIB) [40], nano transfer-printing [41], nano-imprint [42]. Another strategy is through the bottom-up fabrication method including self-assembly of polymers [43] and two -photon polymerizations [44]. The multimaterial fiber fabricated by this method has high sensitively, robustness and small sizes that can be applied to biomedical applications and monolithic silicon sensor has the potential to work in harsh temperatures thanks to its mechanical structure integrities. With the integration with special metal materials, the fiber tip can expand its sensing capabilities and increase its sensing sensitivity through enhanced Raman Scattering and surface plasmon propagation effects.

(3) **Special Coating Techniques:** Coating techniques are employed to fabricate multimaterial functional coatings on the surface of silica fibers. The first approach is the deposition method, commonly used in the semiconductor industry. However, the small dimensions, flexibility, and cylindrical or conical shape of optical fibers present challenges for traditional coating methods when applied to fiber platforms [39,45]. Wet coating methods, on the other hand, are more compatible with optical fiber applications, as they can produce more homogeneous and uniform coatings in the azimuthal direction. Two major categories of wet coating methods for silica optical fibers are the Layer-by-Layer technique and sol-gel matrices, with other methods including molecularly imprinted polymers (MIPs) and metallic nanolayer and particle coatings [46]. The Layer-by-Layer technique involves immersing the silica optical fiber in solutions with opposite electric charges, allowing particles to be absorbed through electrostatic attraction. Multiple layers with different compositions can be introduced by alternating the reaction solutions, and the thickness of the coating can be precisely controlled by adjusting the number of deposition layers. This method is simple and adaptable to various fiber shapes, but the selection of solutions is limited, which can restrict its application in certain sensing scenarios [47,48]. The sol-gel method, on the other hand, is based on the polymerization of hydroxides to form glass-like compositions. The resulting sol-gel matrix can serve as a membrane to support sensing materials on the outside of the silica fiber, or it can act as a sensing material itself, based on optical absorption and luminescent emissions [49,50].

1.5 Fabrication of Thermally Drawn Multimaterial Fiber

1.5.1 Optical Fiber Fabrication Method

A thermal drawing method was first proposed and applied for silica optical fiber fabrications. The silica fiber fabrications involve two steps, first preform fabrications and then thermal drawing process [2].Optical preforms are usually 1 meter in length and several centimeters in diameter, with a defined structure of core-cladding. Several methods have been used for the preform fabrications: First is vapor axial deposition process where the basic material is heated and creating fine particles of amorphous glasses and deposit onto the rotating end surface and form a preform. The second method is outside vapor deposition where the concentric layers of amorphous glasses deposit onto the aluminum mandrel. The third method is the most used method called modified chemical vapor deposition developed by AT&T Bell lab. The metal halide gas and oxygen will be pumped into the rotating quartz tube and forms glass vapor. An external burner will travel back and forth and allow a glass layer to form at the inner part of the glass tube. This process allows high flexibility in the silica preform fabrications. A high purity preform could be fabricated and a precise control of the refractive index can be achieved through layer-by -layer controlling of the oxygen-based reactants sent into the tubes [13]. However, the initial quartz tube must have good quality to generate a good optical fiber preform. The plots for optical preform fabrications and thermal drawing process are shown in Figure 1-2 [51].

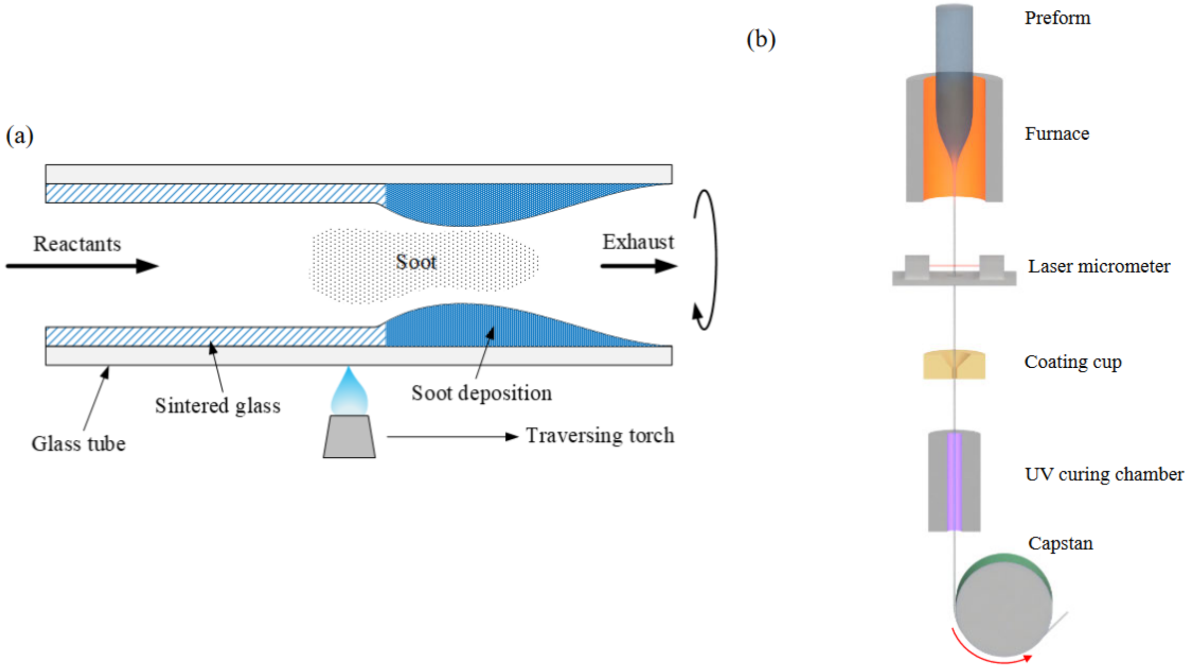

Figure 1-2 (a) Optical preform fabrication with MCVD method (b) Thermal Drawing process.

The fabricated silica optical fiber preform is then transferred to the fiber drawing tower. The preform is heated to over 2000°C until it softens, allowing it to be drawn into fibers with smaller diameters. A laser micrometer positioned below the preform measures the fiber's diameter in real-time. The capstan speed is adjusted based on the micrometer readings until the desired diameter is achieved. Once the target diameter is reached, the fiber is coated with a polymer and cured using UV light. This additional coating alters the strain distribution, enhancing the fiber's robustness against bending. The typical draw-down ratio for silica fiber is approximately 300:1.

1.5.2 Multimaterial Polymer Fiber Fabrications

The same principles used in the silica fiber drawing process have been applied to multimaterial polymer fiber drawing. However, polymer preforms offer several advantages over silica:

1. **Good Machinability:** Polymer preforms are easy to machine, allowing for the creation of side-slots, drilling, and the stacking of multiple layers to form preforms with special functionalities. Microscopic structures can be easily fabricated by constructing them at a macroscopic scale.

2. **Low Drawing Temperatures:** Polymer fibers are typically drawn at temperatures below 500°C, enabling the integration of semiconductor devices, metals, and composite materials into the same preform. This thermal drawing process scales down the structures and, due to the lower temperatures, allows for convergence drawing with high melting point materials like silica. This capability potentially overcomes the challenge of integrating fibers with planar fabrication methods, such as photolithography and molecular beam epitaxy [52].

3. **Low Cost:** Compared to silica fiber drawing, polymer fiber drawing is less expensive due to the lower temperatures required and the affordability of raw materials, making multimaterial fiber fabrication more budget friendly.

4. **High Flexibility:** Polymer materials generally have a Young's Modulus in the MPa range and exhibit high stretchability, making polymer fibers more compatible with wearable and stretchable applications.

The fabrication process for polymer preforms involves thin film rolling, hot pressing, milling, and drilling to create hollow channels, followed by stacking the blocks. Once the preforms are constructed, they undergo a consolidation process in a vacuum oven at temperatures above the preform's softening point to form a solid shape. The preform is then sent to the drawing tower for scale-down processing, as illustrated in Figure 1-3. The preform heating ovens feature three heating zones, with the top and lower zones typically set at lower temperatures than the middle zone, which is maintained above the glass transition temperature of the preform.

Before the drawing process, the preform was sent to the drawing tower and preheated until it softens. During the drawing process, the preform is fed by the down feeding motor with the speed of v_{down} and the scaled down fiber was collected by the capstan with the speed of $v_{capstan}$. During an ideal drawing process, the down fed preform material will be consumed by the fiber. Therefore, the ratio of the diameter between the preform and the polymer fiber will follow the drawdown ratio of ϕ:

$$\phi = \frac{d_{preform}}{d_{fiber}} = \sqrt{\frac{v_{capstan}}{v_{down}}}$$

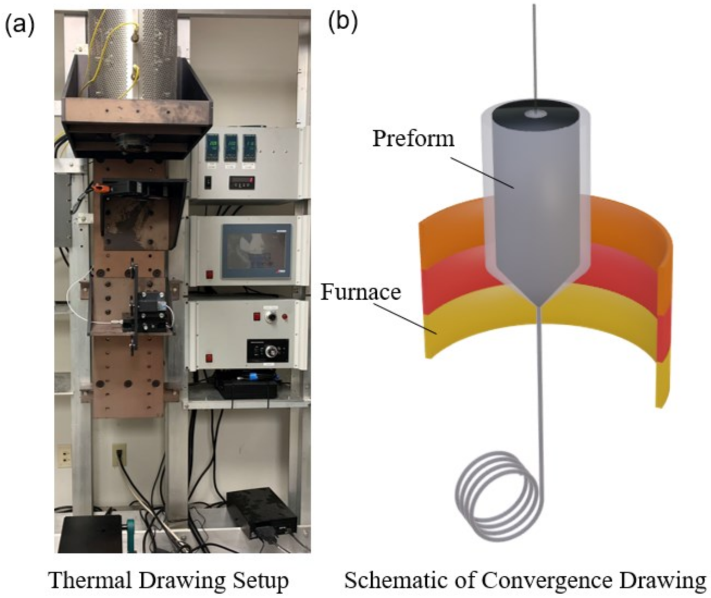

Figure 1-3 (a) Photo of polymer fiber draw tower. (b) Schematic of convergence drawing.

1.6 Proposed Dissertation Outline

Chapter 1 provides an overview of optical fiber sensors and the motivation behind this research. It includes a brief introduction to silica optical fiber sensors and an overview of multimaterial fiber sensors, highlighting the current state of the art and fabrication strategies.

Chapter 2 reports on multi-point magnetic field sensing using a series of Fiber Bragg Gratings (FBGs) and magnetostrictive coatings. It begins with a brief overview of magnetic materials, particularly magnetostrictive materials, followed by the fabrication process of the magnetostrictive fiber and the selection of composite materials.

Chapter 3 focuses on the characterization of the magnetostrictive composite fiber. The chapter discusses the effects of boundary conditions on magnetic sensing capabilities. The sensor's multi-point sensing capabilities are demonstrated through the application of an AC magnetic field.

Chapter 4 introduces a flexible and stretchable double-coil strain sensor, a work published in Advanced Functional Materials [53]. This miniature double-helical fiber sensor features a stretchable core wound with dense double-helical wires. The chapter covers the sensor's design, fabrication, and the development of a theoretical model to calculate relative capacitance changes as a function of applied strain. A numerical simulation model and experimental results are presented to validate the theoretical model, and the chapter concludes with a discussion on the scalable fabrication method.

Chapter 5 details the characterization and application of the double-coil fiber. The sensor demonstrates the ability to withstand up to 100% strain while maintaining low hysteresis, a theoretical resolution of 0.02%, a response time of under 30 milliseconds, and excellent stability after extensive cycling tests. The chapter showcases application scenarios where the sensor is embedded into fabrics and ropes, highlighting its use in sports performance monitoring, structural health monitoring, and implantable applications.

Chapter 6 concludes the dissertation by summarizing the magnetic sensing and strain sensing research. It also outlines potential future research directions.

Chapter 2 Thermally Drawn Magnetostrictive Composite Fiber Design Considerations and Fabrications

2.1 Magnetic Sensing Background

Electromagnetic field sensing has been widely demanded in multiple fields including biomedical applications, space and geophysical researches, machine diagnostics, and electromagnetic pollution monitoring [54–57]. Optical fiber-based magnetic field sensors have garnered significant attention due to their high sensitivity, compact size, remote sensing capability, and multiplexing abilities. The three primary mechanisms utilized in these sensors are the Faraday effect, refractive index modulation of magnetic fluids, and magnetostriction. The Faraday effect involves the rotation of the polarization direction of linearly polarized light as it passes through a magnetic field, with the rotation angle being proportional to the magnetic field strength and the fiber's Verdet constant. This method has been the basis for numerous magnetic sensor designs [58]. However, such magneto-optical material is bulky, fragile and requires complicated interrogation systems. The polarization states of the fiber are vulnerable to environmental perturbations and not suitable for field applications [59]. Magnetic fluid is magnetic nanoparticles dispersed in organic solvent and water [56]. When an external magnetic field is applied to magnetic fluid, the particles within the fluid tend to align and cluster, causing changes in the refractive index and transmittance. While magnetic fluid-based optical sensors offer good sensitivity and simple interrogation schemes, they are constrained by limited dynamic ranges, poor long-term stability, and delayed response times. These limitations restrict the broader application of magnetic fluid sensors.

Fiber Bragg Gratings (FBGs) combined with giant magnetostrictive materials have become a popular choice for optical sensors due to their compact size, large saturation strain, and ease of interrogation. Magnetostriction, a property of ferromagnetic materials, occurs when the magnetic domains within the material rotate and align with an applied magnetic field, leading to changes in the material's dimensions. These strain changes are effectively detected by FBGs. Terfenol-D (TbDyFe), a giant magnetostrictive material, is widely used in magnetic optical sensors. Direct bonding of FBGs to Terfenol-D blocks with epoxy has demonstrated strong sensing capabilities [59–61]. However, pure Terfenol-D blocks are brittle and challenging to machine, making direct bonding of optical fiber sensors to these blocks bulky and impractical for field applications.

Another approach involves coating a thin layer of Terfenol-D onto the optical fiber surface, but this method suffers from low magnetic sensitivity due to the limited thickness of the magnetostrictive layer [62]. Recently, integrating optical fiber sensors into Terfenol-D composite materials has gained attention. These composites consist of a two-phase material with epoxy serving as the supporting matrix and Terfenol-D as the active magnetostrictive phase. The resulting composite material offers enhanced flexibility and exhibits a reasonably linear magnetostrictive response to increasing magnetic field strength, making it a promising solution for advanced sensing applications [54,57,63,64].

While previous work has focused on point sensors where the magnetostrictive material is bonded directly to the location of the Fiber Bragg Gratings (FBGs), fiber optic sensors offer the advantage of distributed sensing. However, the methods limited distributed sensing capabilities due to the restricted bonding or interaction length between the magnetostrictive material and the optical fiber. Distributed measurements are crucial for applications such as electromagnetic pollution monitoring and magnetic field strength mapping.

Two primary strategies for achieving distributed magnetic field sensing have been explored: First, bonding magnetostrictive materials to fiber surfaces: This approach involves attaching materials like Nickel or Fe-Co-V alloy films to the fiber surface and interrogating the strain with Optical Time-Domain Reflectometry (OTDR) [65,66]. While these methods have demonstrated distributed sensing capabilities, the robustness of direct bonding techniques can be improved. Second, integrating nickel wires into fiber cladding: Another method involves thermally drawing Nickel wires into the cladding of the optical fiber, followed by interrogation using Distributed Acoustic Sensing (DAS). This approach enhances the compactness of the fiber but can significantly increase fiber loss due to the metal wires, limiting its effectiveness for remote sensing applications. In this research, we proposed a thermal drawing method to integrate commercially available telecommunications-grade silica fiber with a magnetostrictive polymer coating. This technique facilitates scalable fabrication, overcoming limitations imposed by traditional bonding and coating processes. The convergence drawing process achieves uniformity across the fiber's cross-sectional area, which is critical for distributed or multi-point sensing.

2.2 Magnetostriction Working Principles

2.2.1 Magnetic Materials

According to the classical Bohr model for atoms, electrons follow a circular movement around the nucleus [67,68]. If the orbital radius of the electron is r and the angular velocity is ω. This electron will generate a current of:

$$i = -e\omega \backslash 2\pi \tag{2-1}$$

According to the Ampere's Law, a magnetic momentum is generated due to the current induced by the circular movement of the electron, where for a single electron's moment is:

$$M = -\mu_0 \left(\frac{e\omega}{2\pi}\right)(\pi r^2) = -\frac{\mu_0 e\omega r^2}{2} \tag{2-2}$$

For a single electron, its angular momentum is:

$$P = m\omega r^2 \tag{2-3}$$

The orbital magnetic moment can be rewritten as:

$$M = -\frac{\mu_0 eP}{2m} \tag{2-4}$$

According to quantum theory, the orbital motion of the electron is quantized. Therefore, the magnetic moment of the atom can be rewritten as:

$$M = -\frac{\mu_0 eP}{2m} = -\frac{\mu_0 e\hbar}{2m} l = -M_B l \tag{2-5}$$

Here, $\hbar$ is the plank constant divided by 2π and M_B is the Bohr constant.

In addition to the orbital momentum, the electron also has spin angular momentum. For the spin angular momentum is written as:

$$P = s\hbar \tag{2-6}$$

Here, s is the spin angular momentum quantum number, and it can only be $\pm\frac{1}{2}$. Therefore, the magnetic momentum associated with the spin will be:

$$M = -\frac{\mu_0 eP}{m} \tag{2-7}$$

Considering both the contribution of the magnetic moment due to orbital momentum and spin momentum, the relationship between magnetic moment and momentum is:

$$M = -\frac{g\mu_0 e}{2m} P \tag{2-8}$$

And the g factor is 2 and 1 for spin and orbital motion of the electron respectively, and

$$v = \frac{g\mu_0 e}{2m} = 1.105 \times 10^5 g \ (mA^{-1}s^{-1}) \tag{2-9}$$

And it is called gyromagnetic constant. For an atom, its electrons orbit can be defined by the principle quantum number n and within each of the shell the orbit of the electron depends on the orbital angular momentum $l = 0, 1 ,2, 3,4$ (s, p, d, f, g…). According to the Puali exclusion principle, for each of the atom, with the same principal quantum number *n* and the orbital angular momentum, there will only be two electrons, and those two electrons have the opposite direction of spins.

If the electrons inside a material are all paired, the material is **diamagnetic material**. In this case, the susceptibility of the material is negative and small in the order of 10^{-5}. The negative sign of the susceptibility is due to the acceleration of the electrons due to the applied external magnetic field. Due to Lenz's Law the additional induced magnetic field generate magnetic flux that cancels the external magnetic field. This is called Larmor Precession, and the magnetic momentum of this motion is given by:

$$\mu = -\left(\frac{e^2 r^2}{4m}\right) H \tag{2-10}$$

The induced magnetization is in the direction that cancels the external magnetic field. Materials like Cu, Ag, Pb are demonstrated to have diamagnetism.

However, in the periodic table, most of the atoms have partially filled electron shells, but only nine elements, their metallic alloys, compounds of these elements and a few nonmetallic compounds are ferromagnetic. With the atomic magnetic moment exist in most of the elements, once the atom forms a solid material, the outer layer electrons are redistributed. Consequently, the solids in the periodic table that exhibit strong magnetic moments are those that have unbalanced electrons in the inner shells. Those elements are transition metals, rare earth and actinides. The existence of the unpaired inner shell electrons is due to the Hund's rule for both the restrictions of the resultant spin and orbital moment:

(1) The spin of the electrons is arranged to form a resultant spin ***S*** as large as possible while following Pauli's principle. Due to the Columb repulsion, the electrons tend to take different orbits, and the intra-atomic spin-spin interactions tend to align the spins to be parallel.
(2) Satisfying (1) and Pauli exclusion principle, the orbital vectors of electrons are arranged in the way that the resultant orbital angular momentum ***L*** is maximum.
(3) When the outmost subshell is half-filled or less, the lowest energy level will be the level that has the lowest value of total angular momentum quantum number. If the outmost shell is more than half-filled, the level is the highest value of total angular momentum number has the lowest energy.

Due to the Hund's rule, the transition metal and rare earth elements have more than one unpaired electron in the 3d and 4f shells, which leads to strong atomic moments.

2.2.2 Ferromagnetic Material

With unpaired electrons, the solid material exhibits paramagnetic, ferromagnetism, anti-ferromagnetism and ferrimagnetism. The material's magnetism is temperature related, and the relative comparison between thermal energy and the magnetic energy will transit the material's magnetism from one to another. When it is above the Curie temperature (T_c), the ferromagnetic and ferrimagnetic material transits to paramagnetic materials and when it is above the Néel's Temperature (T_e), the antiferromagnetic material transits to paramagnetic materials.

In paramagnetic, in addition to the same effect as diamagnetism where negative magnetic momentum is induced, the dominant effect for the magnetic moment is atomic momentum alignment under the external magnetic field. However, to align the magnetic moments that are thermally agitated, an enormous external magnetic field is needed. Paramagnetic material usually has positive magnetic moment in the order of $\chi = 10^{-5} \sim 10^{-2}$. The susceptibility of the paramagnetic material is given by Curie's Law, where the susceptibility is inversely proportional to the absolute temperature:

$$\chi = \frac{N\mu^2}{3kT} \tag{2-11}$$

Ferromagnetic material, however, usually has large susceptibility as high as $\chi = 10^3$. This is not only due to the unpaired electrons, but also the exchanged interaction energy between atoms. This theory was proposed by Heisenberg [69] in 1928, which described the exchange interaction between the atoms with spin s_j and s_i:

$$w_{ij} = -2Js_j \cdot s_i \tag{2-12}$$

The exchange integral, J, plays a crucial role in determining the magnetic properties of materials. In antiferromagnetic materials, J is negative, leading to an alignment where all spins are antiparallel to each other, resulting in antiferromagnetism. In this state, the material exhibits no net magnetism without an external magnetic field. However, when an external magnetic field is applied, the material displays a nonzero magnetism because the magnetization of one sublattice differs in strength from the other, creating a net magnetization similar to that seen in ferrimagnetic materials. Conversely, when J is positive, all atomic moments align parallel to each other, resulting in ferromagnetism. The underlying physics of the exchange interaction is driven by the minimization of Coulomb energy and adherence to Pauli's exclusion principle. When atoms are close, if their spins are antiparallel, they share the same molecular orbital, increasing the Coulomb energy but minimizing the overall energy due to spin cancellation. On the other hand, when the spins are parallel, the atoms do not share the same molecular orbital, leading to a lower Coulomb energy. The reduction in Coulomb energy outweighs the energy increase from parallel spins, thus favoring ferromagnetism.

2.2.3 Magnetostriction Theory

Magnetostriction is a property of ferromagnetic material. The first magnetostriction effect was observed in iron by James Jule in 1842 [70]. Magnetostriction is an effect that is shared by all ferromagnetic material. Table 1 listed the saturation strain and Curie Temperature of some magentostrictive materials [71].

Table 1 Magnetostriction Properties of Some Magnetostrictive Materials

Material	**Saturation strain in [ppm]**	**Curie temperature in [K]**
Ni	-50	630
Fe	-14	1040
Fe_3O_4	60	860
Terfenol-D	2000	650
$Tb_{0.5}Zn_{0.5}$	5500	180
$Tb_{0.5}Dy_xZn$	5000	200

The spontaneous magnetization of the ferromagnetic material is due to the exchange of energy. With the exchange of energy, the atomic moments within the ferromagnetic material are aligned with each other. However, the balance between the magnetostatic energy and the exchange energy makes the material split into mesoscopic domains. Within the magnetic domains, the atoms maintain the same magnetization directions. When an external magnetic field is applied, the magnetic domain boundaries shift, and the magnetic domains rotates. The overall shape of the magnetostrictive material changes. The physics behind magnetostriction is magnetocrystalline anisotropy. With magnetocrystalline anisotropy, the magnetic material has an easy axis, and they tend to rearrange their easy axis with the external magnetic field to lower the free energy of the system. The material will exhibit different dimensions with different crystal directions, therefore, strain is generated in the material. Magnetostrictive materials are associated with four magnetomechanical effects listed in Figure 2-1 [72].

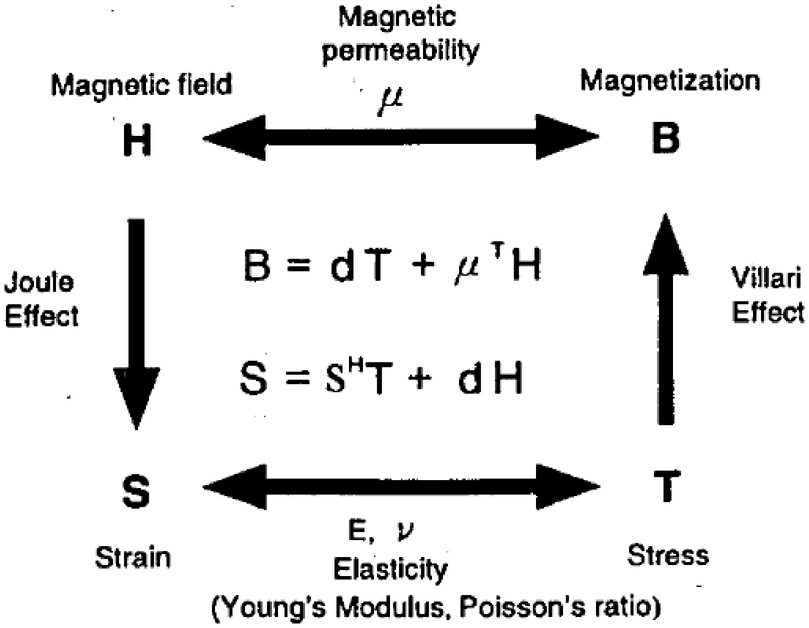

Figure 2-1 Four magnetomechnical coupling in magnetostrictive materials.

Among all the effects, the Joule effect has been studied extensively. Although most of the ferromagnetic material exhibits magnetostrictions, most of the material only has magnetostriction in the order of 10^{-6}. There are a few materials that exhibit high magnetostrictions. Cobalt exhibits the largest room-temperature magnetostriction (60 ppm) among all the pure elements. To utilize the magnetostrictive effects, several alloys have been developed to demonstrate high magnetostrictions. The giant magnetostrictive material (GMM) was developed by A.E. Clark in the 1960s. Among all the materials, Terfenol-D ('Te' for Terbium, 'Fe' for iron, 'NOL' for Naval Ordnance Laboratory and D for Dysprosium) [71] has the best balance between operating temperature, high magnetostriction and saturation magnetic field. Depending on the composition ratio of the Terfenol-D materials, their magnetostrictions vary from each other (shown in Figure 2-2), but all exhibit around 2,000 ppm with 160 kA/m external magnetic field. Other magnetostrictive alloys such as Galfenol and amorphous alloy FeSiBC (trade name Metglas) have lower saturation fields at lower applied external magnetic fields. Galfenol has 200-400 ppm strain with around 200 Oe magnetic field (equivalently 20 mT magnetic flux density). Metglas exhibits 20 ppm strain with less than 1 kA/m magnetic field [73–75].

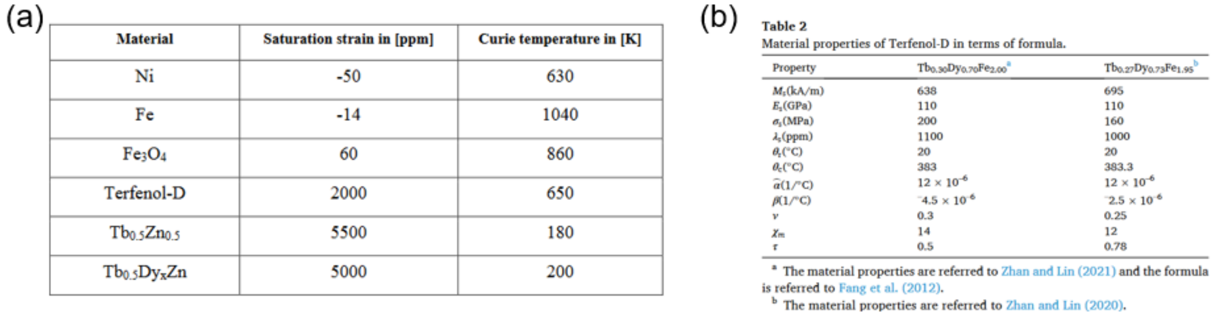

(a)

Material	Saturation strain in [ppm]	Curie temperature in [K]
Ni	-50	630
Fe	-14	1040
Fe_3O_4	60	860
Terfenol-D	2000	650
$Tb_{0.5}Zn_{0.5}$	5500	180
$Tb_{0.5}Dy_xZn$	5000	200

(b)

Table 2
Material properties of Terfenol-D in terms of formula.

Property	$Tb_{0.30}Dy_{0.70}Fe_{2.00}$[a]	$Tb_{0.27}Dy_{0.73}Fe_{1.95}$[b]
M_s(kA/m)	638	695
E_s(GPa)	110	110
σ_s(MPa)	200	160
λ_s(ppm)	1100	1000
θ_r(°C)	20	20
θ_c(°C)	383	383.3
$\widehat{\alpha}$(1/°C)	12×10^{-6}	12×10^{-6}
β(1/°C)	$^{-}4.5 \times 10^{-6}$	$^{-}2.5 \times 10^{-6}$
ν	0.3	0.25
χ_m	14	12
τ	0.5	0.78

[a] The material properties are referred to Zhan and Lin (2021) and the formula is referred to Fang et al. (2012).
[b] The material properties are referred to Zhan and Lin (2020).

Figure 2-2 (a) Saturation strains and Curie temperatures of serval common magnetostrictive materials. (b) Magnetic properties of Terfenol-D with different compositions.

Considering the material availability, we choose Terfenol-D as the active phase of the magnetostrictive material. A constitutive equation was adopted to theoretically fit the magnetostrictive properties of the pure bulk Terfenol-D material. According to the model built by Zhan and Lin [74], the magnetostrictive property of the Terfenol-D material can be expressed as a function of the magnetic field, thermal field and its own elastic properties:

$$\begin{aligned}\varepsilon_{ij} &= \frac{1}{E_s}\left[(1+\nu)\sigma_{ij} - \nu\sigma_{kk}\delta_{ij}\right] + \lambda_s\left(\frac{\frac{3}{2}\exp\left[\eta\sigma_{ij}\right]}{\Sigma} - \frac{1}{2}\right)\delta_{ij} + \hat{a}\delta_{ij}(\theta-\theta_r) \\ &\quad + \frac{\frac{3}{2}\lambda_s}{\left(M_s(\theta)\right)^2}\left[M_iM_j - \left(\frac{\exp\left(\eta\sigma_{ij}\right)}{\Sigma} - \frac{\frac{2}{3}\beta(\theta-\theta_r)}{\lambda_s}\right)\delta_{ij}M_kM_k\right]\end{aligned} \tag{2-13}$$

Here $E_s, \nu, \lambda_s, \hat{a}$ and β are the saturation Young's modulus, Poission's ratio, saturation magnetostriction constant, thermal expansion coefficient, and the slope between the magnetostriction and thermal expansion coefficient. Additionally, θ_r is the reference temperature, δ_{ij} is the Kronecker delta. $M_s(\theta)$ is the temperature dependent staturation magnetization. Its relationship with eh Cuire temperature θ_c, saturation magnetization M_s and material coefficient τ is:

$$M_s(\theta) = M_s\left(1 - \frac{\theta-\theta_r}{\theta_c-\theta_r}\right)^{\tau} \tag{2-14}$$

Additionally, η and $\overline{\Sigma}$ are derived as:

$$\eta = \frac{3}{\sigma_s} \tag{2-15}$$

$$\overline{\Sigma} = \sum_{i=1}^{3} \exp\left[\eta\sigma_{ii}\right] \tag{2-16}$$

Here, σ_s is the stress needed for all domain rotation in an applied magnetic field. In addition, ignoring the hysteresis effect of the Terfenol-D material, the magnetic field is expressed as the function of stress, magnetization, and temperature:

$$H_k = \frac{1}{k(\theta)} \tan\left(\frac{\pi M_l}{2M_s(\theta)}\right) \delta_{kl} \tag{2-17}$$

$$- \frac{\frac{3}{\mu_0}\lambda_s}{\left(M_s(\theta)\right)^2} \left[\sigma_{kl} - \frac{1}{\eta} ln \left|\frac{\bar{\Sigma}}{1 - (\exp[\eta\sigma_{mn}] - \bar{\Sigma})}\right| \sigma_{mn}\delta_{kl} + \frac{2}{3}\frac{\beta\sigma_{ij}(\theta - \theta_r)\sigma_{kl}}{\lambda_s}\sigma_{ij}\right] M_l \tag{2-18}$$

Here,μ_0, $k(\theta)$ are the permeability of the free space and relaxation factor, which is related to the magnetic susceptibility and saturation magnetostriction χ_m and $M_s(\theta)$:

$$k(\theta) = \frac{\pi}{2}\chi_m / M_s(\theta) \tag{2-19}$$

In addition, the magnetic field strength and the magnetic flux density are related by

$$B_i = \mu_0(H_i + M_i) \tag{2-20}$$

For our following investigations, we are trying to first simulate the properties of the active phase, the magnetostrictive Terfernol-D material for its magnetostriction properties, then expand its property to the magnetostrictive composite material.

Here, we used the data obtained from the Tefernol-D power supplier (TdVib, LLC.) and try to use the equations to fit its magnetostriction properties. In our case, the temperature and anisotropy of the material was ignored, therefore, the magnetostrictive property of the material can be simplified as:

$$M = 2 \cdot \frac{M_s}{\pi} \cdot \tan^{-1}(H \cdot k) \tag{2-21}$$

$$\varepsilon(H) = 1.5 \cdot \lambda_s \cdot \frac{M^2}{M_s^2} \tag{2-22}$$

Where M is the magnetization, M_s is the saturation magnetization, H is the magnetic field strength, k is the relaxation factor, $k = \frac{\pi}{2}\frac{\chi}{M_s}$, χ is the magnetic susceptibility,λ_s is the saturation magnetostriction. The fitted curve as well as the raw measured data from the supplier is plotted in Figure 2-3.

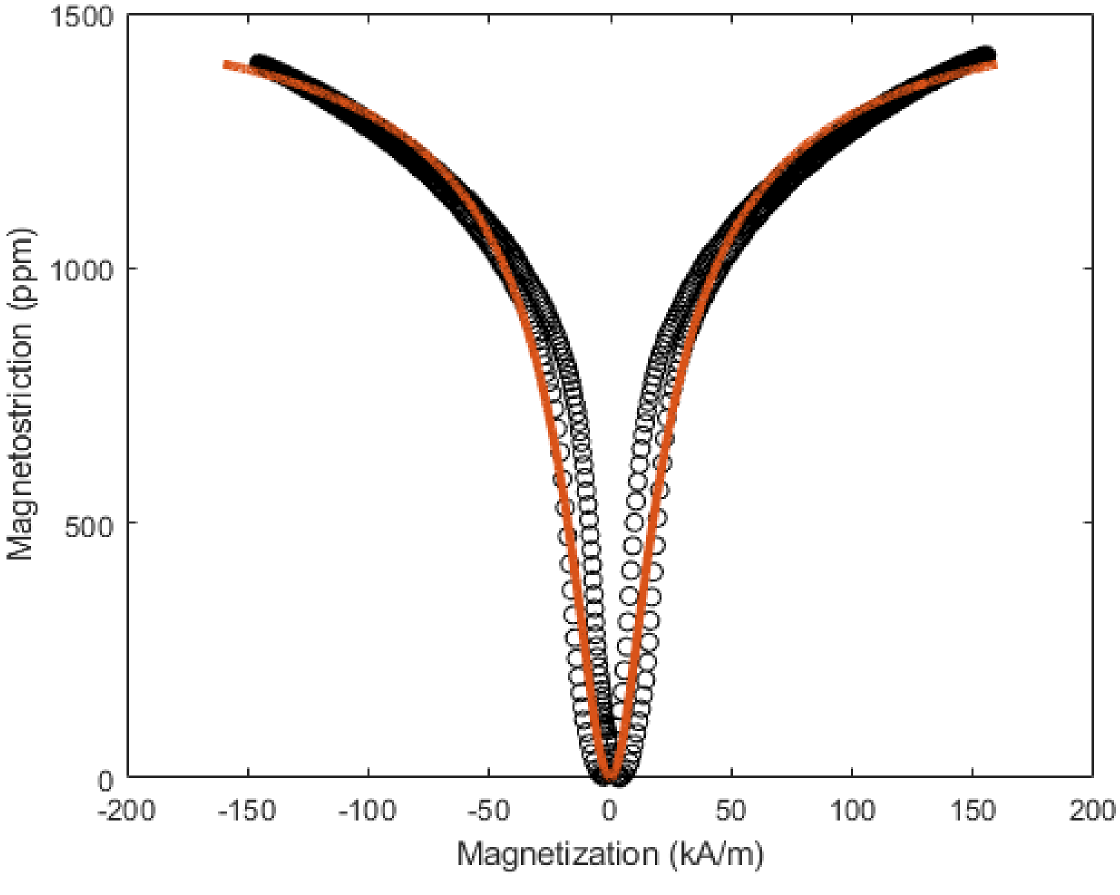

Figure 2-3 Measured magnetostriction data for $Tb_{0.3}Dy_{0.7}Fe_{1.92}$ (black dots) and fitted line by the model.

Here, the fitted line shows good agreement with the overall magnetostrivtive properties of the measured Terfenol-D materials. While the hysteresis effects are ignored in this simplified model, this model is good for our later characterization on the magnetostrictive effects of the Terfenol-D material and its composite materials.

2.2.4 Magnetostrictive Composite Material

As mentioned in the previous section, the giant magnetostrictive material Terfenol-D is an alloy material composing terbium, dysprosium, and iron, and it has the highest room-temperature saturation strain among all the giant magnetostrictive material [76]. See Figure 2-4 for the magnetostriction curve of the Terfenol-D. Magnetostriction comes from the spin-spin and spin-orbital interactions between the intermetallic phases inside the alloy. The Terfenol-D material possesses high shape anisotropy. In this same figure, it shows the magnetostriction behavior of parallel and transverse magnetic fields [77].

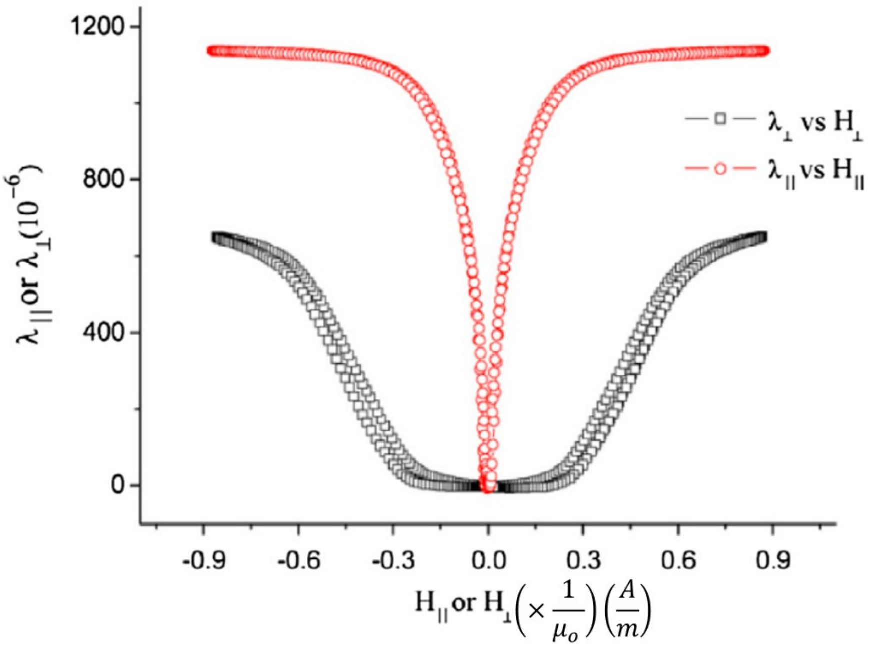

Figure 2-4 Magnetostriction responses of the Terfenol-D with anisotropy.

Despite the advantages of monolithic magnetostrictive materials, such as their strong magnetostrictive properties, they are inherently brittle and difficult to shape into desired forms. To overcome these limitations, dispersing magnetostrictive materials within a polymer matrix has proven to be highly beneficial for transducer production. This approach offers several advantages, including greater flexibility in shaping the material into various forms, making it more suitable for diverse applications. Additionally, the polymer matrix, with its high electrical resistance, serves as an interlayer that significantly reduces eddy current effects, thereby extending the dynamic response range of the transducer from 1 kHz to up to 100 kHz, which enhances the overall performance of the device. Furthermore, the magnetostrictive composite material allows for tunability in particle orientation within the matrix. By aligning the magnetostrictive particles in the longitudinal direction to form a chain-like structure, the material's responsiveness to magnetic fields is significantly improved, making it more efficient and effective as a transducer.

Multiple binding polymer materials have been investigated for the magnetostrictive composite material in literatures . For the consideration of the strength and low temperature operations, thermal setting material like epoxy has been adopted. With epoxy/T-D composite material, response could be improved by alignment and forming a 1-3 composite which has higher magneto-striction than 0-3 composite materials. Another method to increase the composite material response is prestress. Researches has reported 5 times increase on the magnetostrictions with 50 MPa preload [78].

Another option of the binding material is elastomers, which allows the magnetostrictive composite material been thermally drawn into fiber coatings. Here we proposed a magnetostrictive composite material consisting of thermal plastic polymers and Terfenol-D particles.

Table 2 Thermal plastic material properties.

Material	*PMMA*	*ABS*	*TPE*	*PEI*	*HDPE*	*LDPE*	*PET*	*PP*
E(Mpa)	2855	2588	2	6000	1000	300	2950	1325
γ	0.37	0.37	0.49	0.34	0.42	0.34	0.34	0.42

To investigate the properties of the composite material with various thermoplastic elastomers, we conducted a Finite Element Analysis (FEA) simulation using COMSOL, sweeping the material responses across different polymer choices. As illustrated in Figure 2-5(a), a simplified 2D model was constructed to represent a composite with 20% volume fraction of Terfenol-D particles. For this first-order approximation, the particles were modeled with a round shape. A range of commonly used thermoplastic materials were tested within the model to identify the optimal material choice. As depicted in Figure 2-5(b), the blue dots represent the strain observed in the magnetostrictive material when subjected to a transverse offset sinusoidal wave. The applied magnetic field was set at 1 kA/m with an offset of 0.5 kA/m, ensuring that the magnetic field direction remained constant. The frequency of the magnetic field was 20 Hz, and the magnetostrictive properties of the composite material were analyzed under these conditions. In Figure 2-5(b), the blue dots indicate the strain observed within the Terfenol-D particles, while the green dots represent the overall integrated strain within the composite material. The results show that the composite material incorporating the Thermoplastic Elastomer (TPE, Styrene-Ethylene-Butadiene-Styrene, SEBS) exhibited the lowest Young's modulus and the highest strain within the composite matrix.

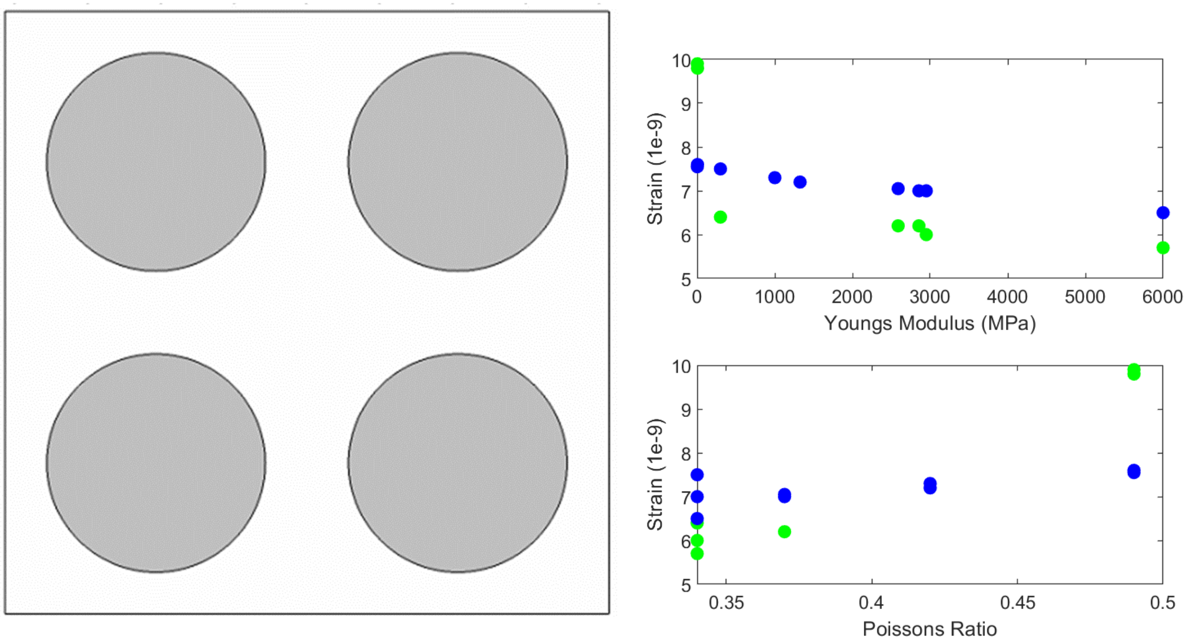

Figure 2-5 FEA simulations of the magneto strictive material. (a) the 2D model (b) simulated results

Additionally, the frequency responses of the composite material in comparison to the applied magnetic field and the pure magneto strictive particles have also been investigated. In

Figure 2-6, the time domain responses of the composite material and the pure particles, in combination with the applied off-centered magnetic field was plotted. Both the pure magnetic material and the composite material show the same fundamental frequency responses to the applied magnetic field, and the pure and composite material shows a similar waveform but at different scaling. This shows that the magneto-strive material follows the same trend of magnetostriction as the pure material and polymer matrix will be compressed and expanded in the same direction as the applied magnetic field. However, for the case where the magnetic field is centered, the composite material exhibits second harmonic responses.

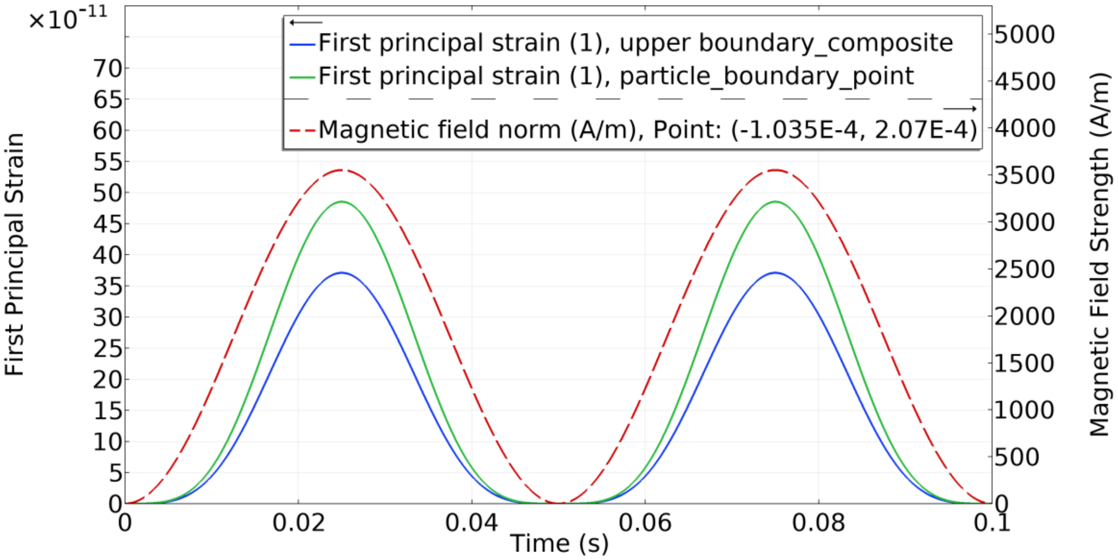

Figure 2-6 Magnetostrictive composite material time domain responses.

2.3 Magnetostrictive Composite Fiber Fabrications

2.3.1 Point by point Fiber Bragg Grating Inscriptions

A series of Fiber Bragg Gratings (FBGs) multiplexed in the wavelength domain were inscribed using a femtosecond laser system with the Point-by-Point (PbP) technique, as shown in Figure 2-7 (a). The FBGs were fabricated with an 800 nm Ti: Sapphire femtosecond laser system operating at a repetition rate of 500 Hz, and the laser power was set to 160 μW, corresponding to a pulse energy of 320 nJ. The femtosecond laser pulse was focused using a 100x oil-immersed objective. Single-mode silica fiber (SMF 28e, Corning) with an acrylate coating was mounted on an air-bearing stage (ABL10050L-LN, Aerotech Corp.) moving at a speed around 0.8 mm/s. The acrylate coating was retained on the silica fiber to maintain its mechanical integrity during the subsequent thermal drawing process. Details of the femtosecond laser writing setup can be found in our previous work. [10,11]

While the width of the grating (the wavelength interval between the first zeroes) depends on both grating's coupling constant κ and grating length L, given by equation:

$$\Delta\lambda = \frac{\lambda_B^2}{2n_{eff}}\sqrt{\frac{\kappa^2}{\pi^2}+\frac{1}{L^2}}$$

Where $\Delta\lambda$ is the width of the grating, λ_B is the Bragg wavelength and the n_{eff} is the effective refractive index. A longer grating length results in a narrower linewidth and sharper edges in the FBG spectrum. However, FBGs fabricated using the point-by-point method experience significant broad out-of-band loss due to Mie scattering from the micro-void damage points [79,80]. The point-by-point inscription method allows for tuning of the laser's writing power, grating order, grating length, and lateral positions to balance out-of-band scattering loss and FBG sensitivity. After several trials with different parameters, we tuned our FBGs to the 2nd order, written barely above the damaging threshold and offset by 1.5 μm to minimize DC scattering loss while maintaining the desired FBG sensitivity. Figure 2-7 (b) shows microscopic images of the fabricated FBGs from front and side views. Figure 2-7 (c) displays the reflection spectrum of the FBG series, where the maximum sensitivity is around 8 mW/(nm·mW). Each

FBG spectrum was measured independently using an optical interrogator (Micron Optics, SM125), and the derivative of the spectrum was calculated after smoothing the data.

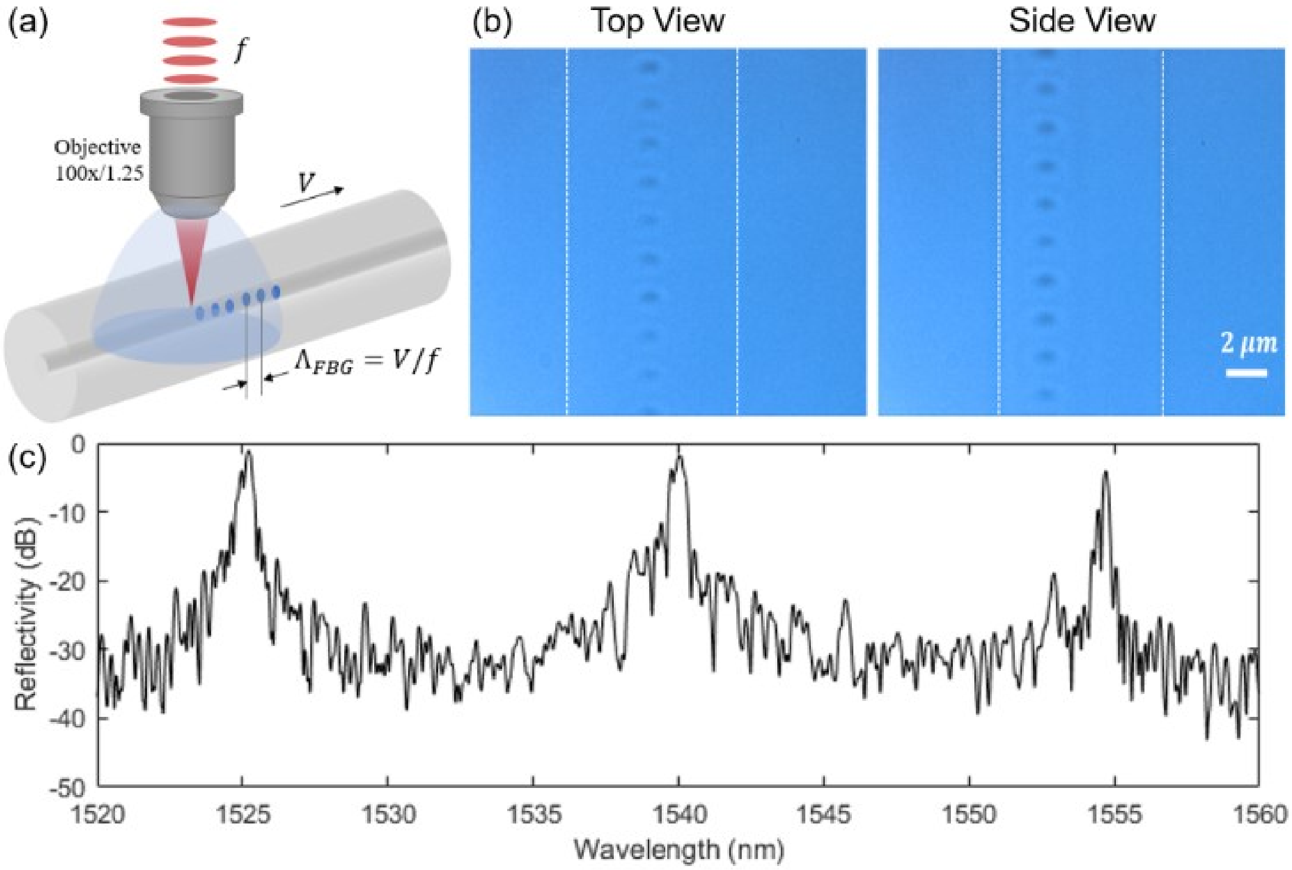

Figure 2-7. (a) Femtosecond laser point-by-point inscription of the Fiber Bragg Gratings (FBGs) in SMF 28 fiber. (b) Microscopic images of fabricated gratings. (c) Reflection spectrum of the inscribed FBGs.

2.3.2 Thermal Drawing Process of Magnetostrictive Fiber

To fabricate the magnetostrictive composite fiber, we utilize a scalable thermal drawing process. The first step involves constructing a macroscopic “preform.” The preform fabrication process is illustrated in Figure 2-8 (a). Initially, magnetostrictive Terfenol-D particles (TdVib, LLC, ETREMA) are dispersed into a thermoplastic elastomer matrix (Styrene-ethylene-butylene-styrene, SEBS) on a hot plate at 200°C. Due to the increased viscosity of the composite material with higher particle volume concentration [81], a 20% volume percentage of Terfenol-D particles is chosen to balance sensor sensitivity and thermal drawing stability. The magnetostrictive composite films are then rolled onto a ¼’’ Teflon rod, followed by a layer of elastic Cyclic Olefin Copolymer (eCOC). The eCOC layer serves as a protective layer during the etching process due to its elasticity and resistance to acetone. The preform is consolidated in a vacuum furnace at 190℃ for 10 minutes.

After cooling, additional PMMA films are rolled onto the preform and consolidated at 165℃ for 20 minutes. The PMMA layer acts as a sacrificial layer to improve the stability of the thermal drawing process. The consolidated preform results in a 6-inch-long tube with a ¼-inch inner diameter and approximately 1-inch outer diameter. Optical fibers with FBGs, fabricated in the previous steps, are fed into the hollow core of the preform during the thermal drawing process. As shown in Figure 2-8 (b), using a custom-built fiber drawing tower and applying a thermal gradient across three zones (120-280℃), the magnetostrictive layer collapses and merges with the outer layer of the acrylate-coated optical fiber. Figure 2-8 (c) displays an image of the drawn magnetostrictive fiber, which has an overall diameter of approximately 1 mm before the PMMA sacrificial layer is etched away. This scalable fabrication method allows for the continuous production of tens of meters of magnetostrictive fibers for distributed sensing applications. Figure 2-8 (d) shows an image of the drawn magnetostrictive fiber wound on a fiber spool. The spliced section of the uncoated silica fiber serves as the lead-in fiber for remote sensing applications.

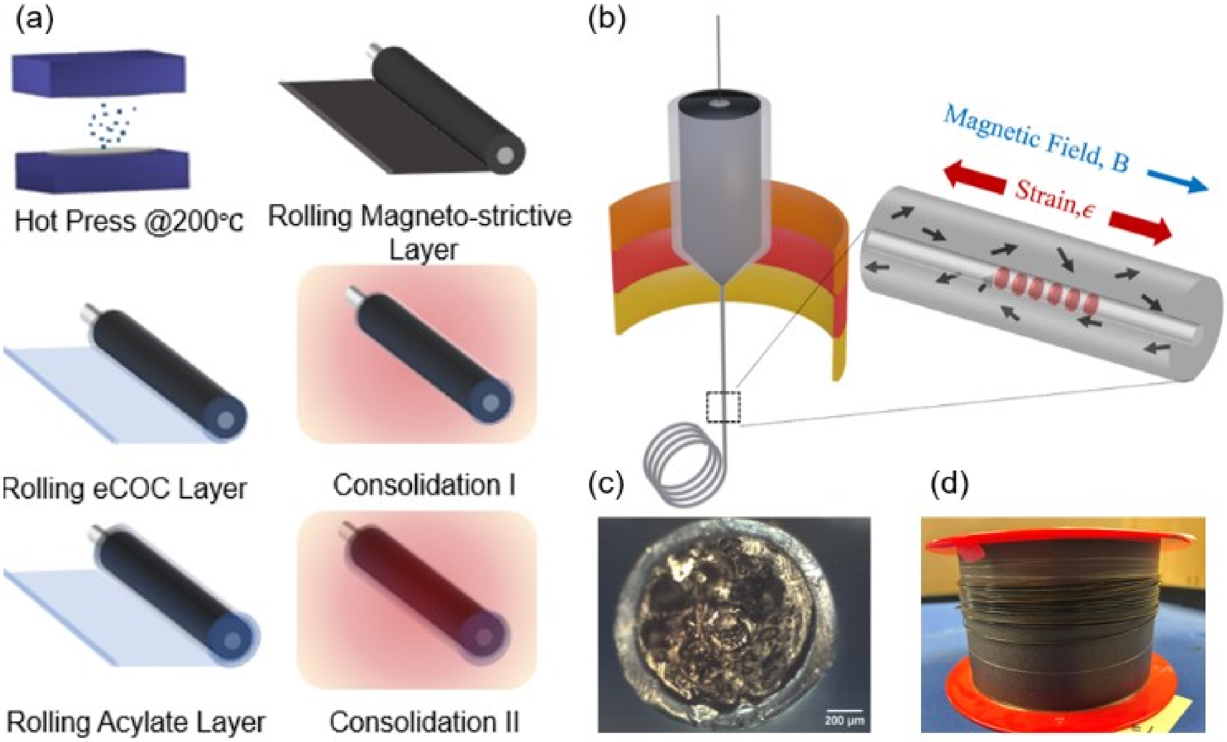

Figure 2-8 (a) Thermal drawing setup (b) Schematic convergence drawing (c) Photo of a series FBG with magnetostrictive coating (d) Cross-sectional area of the thermally drawn fiber.

Chapter 3 Thermally Drawn Magnetostrictive Composite Fiber Characterizations

3.1 Interrogation System

An optical sensing interrogation system was built to measure the real-time strain signal in the fiber, as shown in Figure 3-1 (a). The magnetostrictive fiber was connected to the port 2 of a single-mode circulator (S/N-12240010), with the input arm (port 1) connected to a 50:50 coupler containing a broadband super-luminescent diode (Thorlabs, S5FC-1005P) and a C-band tunable laser (New Focus, TLB-6728-P). Port 3 of the circulator was connected to a 99:1 fiber coupler, where the 99% split arm went to the photodetectors, and the 1% split arm went to the Optical Spectrum Analyzer (OSA) to obtain the system spectrum.

After obtaining the spectrum of the FBG and calculating its bias point, the tunable laser served as the probe light and was tuned to the most sensitive bias point of the FBG. The reflected light from the FBG was split into two arms by another 50:50 coupler. One arm of the coupler went to an unbalanced photodetector (New Focus, Model 2117) to monitor the position of the probe light on the spectrum, allowing for active adjustments if there were ambient temperature variations. The other arm of the reflected signal and an arm connected directly to the light source passing through a variable optical attenuator (VOA) were connected to a balanced photodetector (New Focus, Model 2117) to eliminate the DC component of the measured signal and allow the detector to work at the highest possible gain.

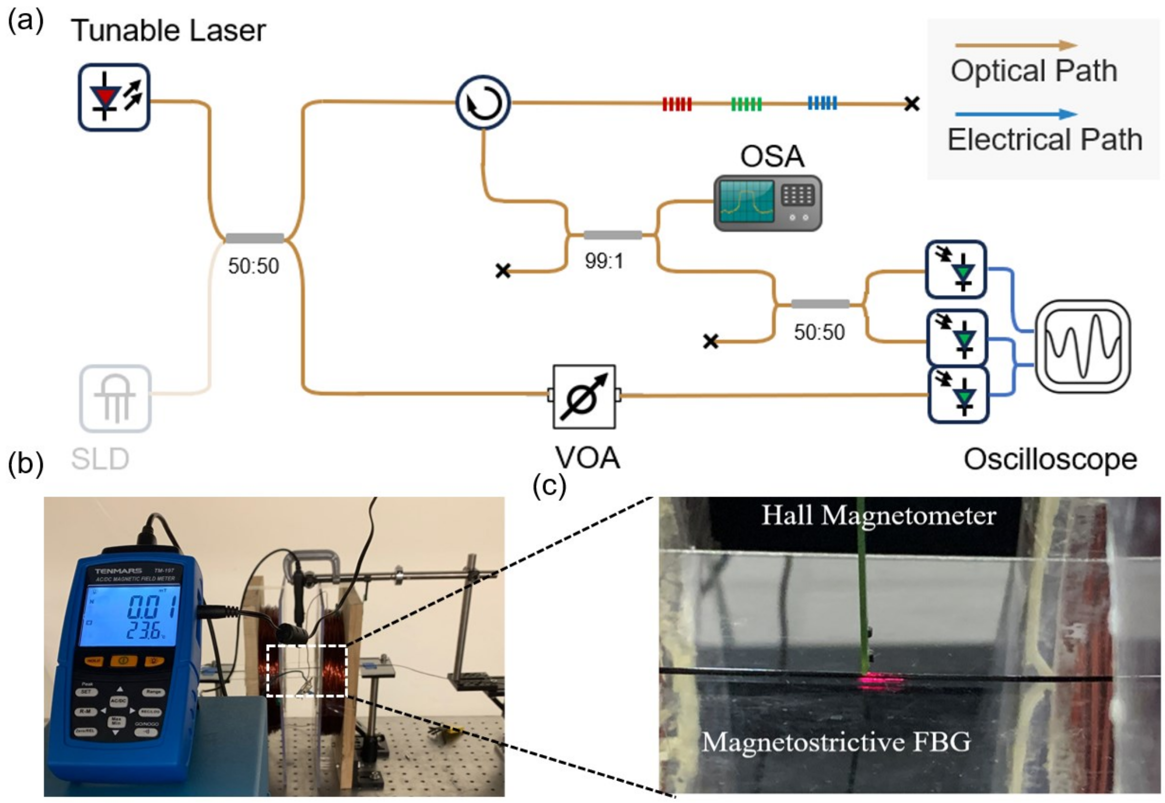

Figure 3-1 (a) Schematic of interrogation system. (b) Photo of magnetic field generation setup and zoomed in picture showing the location of FBG and reference Hall sensor

A function generator (Tektronix, AFG 3252) was programmed to output sinusoidal signals with various peak-to-peak amplitudes. This signal was then amplified by a power amplifier (NF, HAS-4011) with the gain of 20, and the amplified driving voltage was connected to a custom-built Helmholtz coil with a diameter of 5 inches. Both the signal from the photodetectors and the function generator are triggered by the same pulse signal and were connected to an oscilloscope for recording. The thermally drawn magnetostrictive fiber passed through the Helmholtz coil center and was either clamped down to two firmly screwed frame or leave it free at two ends, maintaining the location of the FBG at the center of the Helmholtz coil, where the magnetic field is uniform (Figure 3-1 (b)). Additionally, a one-axis Hall sensor (TENMARS TM197) was placed at the center region of the Helmholtz coil, right above the FBG, to serve as the reference value of the magnetic field measurements.

To minimize possible electromagnetic interference from the Helmholtz coil to the photodetectors and other interrogation units, the coil was placed 10 meters away from the interrogation system, and the magnetostrictive fiber was connected to the interrogation system by a 10+ meter lead-in fiber with no magnetostrictive coating.

3.2 Magnetostrictive Material Characterization

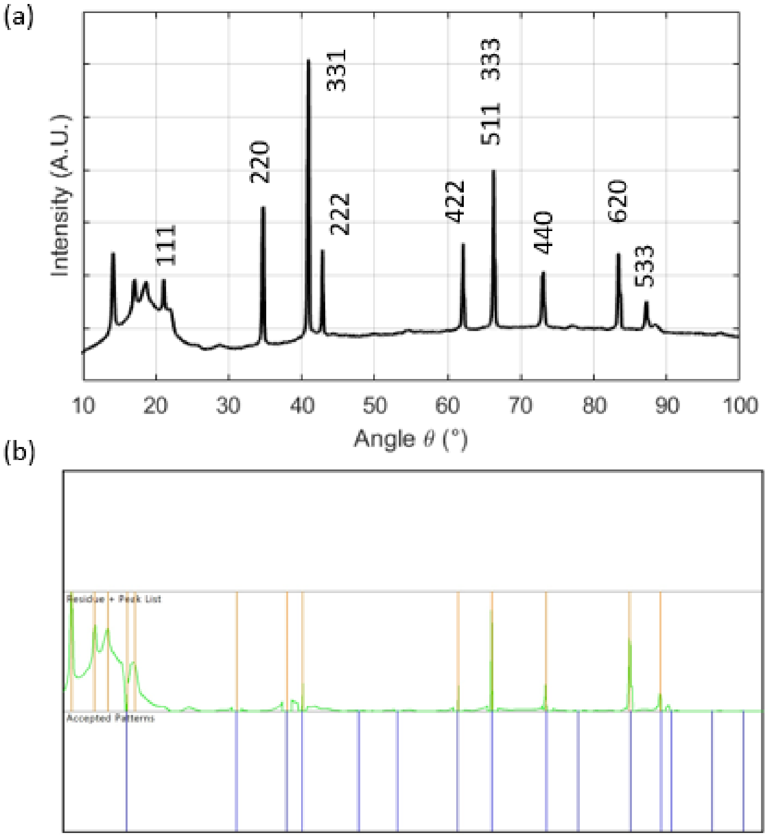

Figure 3-2 X ray diffraction measurement results. (a) Measured diffraction pattern by refractometry. (b) The post-processed X ray diffraction data with the comparison with the standard Terfenol-D diffraction data in the database.

The magnetostrictive composite material was characterized using X-ray diffraction (XRD). A circular film, fabricated through thermal hot-pressing, was prepared to fit the sample tray of a Malvern Panalytical Empyrean diffractometer with a Cu source. The XRD analysis, covering angle ranges of $10° < \theta < 100°$ is shown in Figure 3-2. The diffraction peaks corresponding to the (220), (311), and (333/511) planes exhibit nearly equal intensities, suggesting that the composite material exhibits minimal anisotropy at room temperature, consistent with literature findings.

3.3 Sensing Mechanism and Boundary Condition Discussions

A periodic magnetic field generated by the Helmholtz coil induces a periodic strain in the magnetostrictive composite layer. This strain arises from the magnetostriction effects of the Terfenol-D particles and the dynamic magnetic force acting on the ferromagnetic composite material. In the composite, the active Terfenol-D phase exhibits magnetostriction, where the alignment of its inner domains changes the material's overall shape when subjected to a magnetic field. This causes the magnetostrictive layer to elongate in the direction of the applied field. Additionally, the ferromagnetic material experiences a time-varying magnetic force as the magnetic field changes. These combined effects cause the composite layer within the AC magnetic field to respond to the external magnetic field. The uniform bonding between the magnetostrictive layer and the acrylate coating ensures that the strain induced by the magnetic field is transferred to the inner silica fiber. By tracking the wavelength shifting of the FBG, the strain inside the fiber was calculated by (3-1) [3,82]:

$$\frac{\Delta\lambda_B}{\varepsilon} = \lambda_B(1 - \frac{n^2}{2}[p_{11} - \nu(p_{11} + p_{12})]) \tag{3-1}$$

Where n is the effective refractive index, p_{11}, p_{12} are strain optic tensor and are 0.1 and 0.28 respectively. The final conversion between the relative center wavelength shift and strain is $\varepsilon = \frac{1.26\Delta\lambda_B}{\lambda_B}$. As the central wavelength of the FBG periodically shifts, the reflected power from the edge of the FBG will show a periodic pattern and will be recorded by the balanced photodetector for our magnetic field measurements.

Although the 5-mm inscribed FBG acts as a point sensor for strain measurement, unlike other FBG-based magnetic field sensors where the magnetostrictive layer is locally bonded at the FBG location, the magnetic field response discussed here is dependent on boundary conditions. With a uniform magnetostrictive layer coating, the section of the fiber within the magnetic field acts as a transducer, generating acoustic waves that propagate throughout the entire coated multimaterial fiber. The FBG then measures the local strain within this acoustic waveguide. While polymer materials typically exhibit high damping due to viscoelastic and hysteresis effects, the acoustic damping in polymers is linearly proportional to the acoustic frequency [83,84]. As we mainly focus our study on low frequency components where the applied AC magnetic field is below 100 Hz and the acoustic waveguide is less than 1 meter, the acoustic damping effects can be ignored.

We examined the local strain measured by the FBG under both fixed boundary conditions with varying tension and a free boundary condition. As shown in the inset schematic in Figure 3-3(a), the magnetic fiber was clamped using two customized plastic clamps, leaving the section between them freely suspended in the air. A micrometer was attached beneath one of the clamps to adjust the tension in the fiber, which was estimated by tracking the central wavelength of the FBG. The distance between the clamps was approximately 41 cm. Figure 3-3 (a) displays the frequency characteristics of one of the fiber sensors under tension. By sweeping the frequency of the magnetic field f_0 from 10 Hz to 100 Hz with a normalized constant peak-to-peak amplitude, we observed several resonance peaks due to standing wave effects under the fixed boundary condition. Figure 3-3 (c) presents the time-domain signals and frequency spectrum at (i) 20 Hz, (ii) 40 Hz, and (iii) 80 Hz, respectively. The data show that the measured sensor signal f_m predominantly corresponded to the second harmonic of the applied signal f_0. This is consistent with the properties of the magnetostrictive Terfenol-D particles in the composite material, where the second harmonic response is expected due to the symmetry of the magnetostriction curve [85].

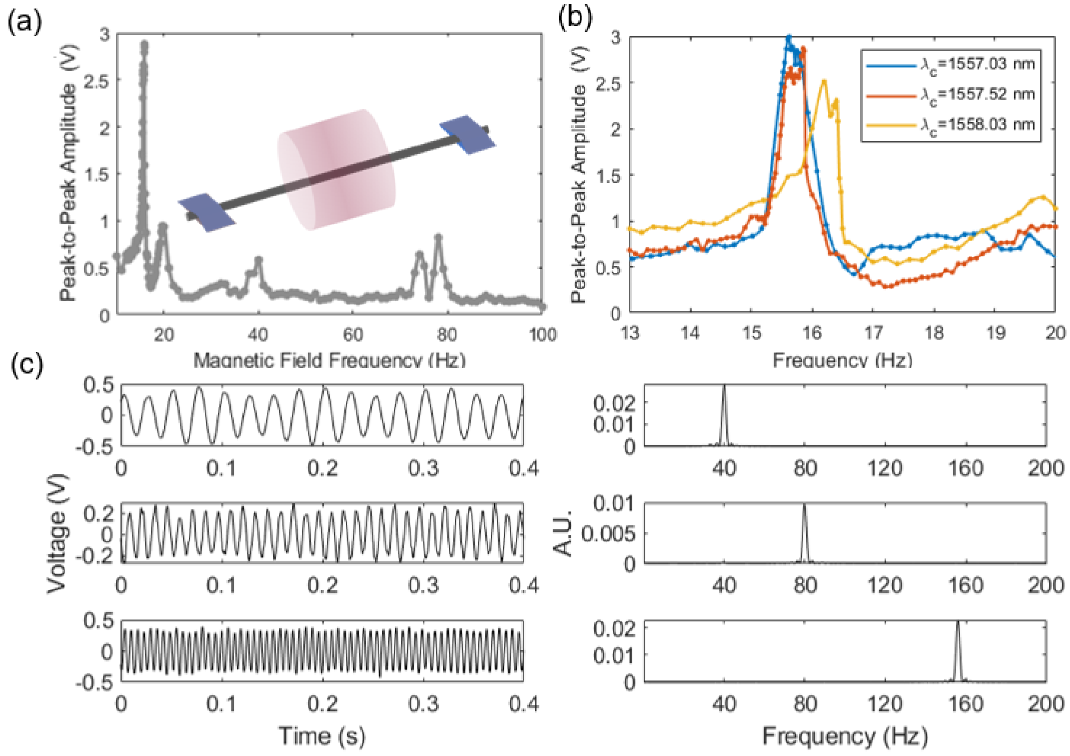

Figure 3-3 (a) Frequency spectrum Time domain signal with 20, 40, 80 Hz AC magnetic field. (b) Location of the first resonance peak under different strains. (c) The time and frequency domain of the sensor's signal with 20 Hz, 40 Hz, and 80 Hz input.

To understand how the tension applied to fiber changes the resonance peaks, we adjusted the position of the micrometers and measured the positions of the first resonance peaks under different tensions. According to string vibration theory, the natural frequencies of the string under tension is:

$$f_n = \frac{n}{2L}\sqrt{\frac{T}{\mu}} \tag{3-2}$$

Where n, L, T, μ are the order of the harmonics, length of between the clamps, and the linear density of the string, respectively. In Figure 3-3 (b), we plotted the zoomed-in plot of the measured first resonance peak of the sensor as tension increases. The resonance central frequency shifts from 15.61 Hz to 16.2 Hz as the tension increases, with the central wavelength of the FBG shifting from 1557.03 nm to 1558.03 nm. By adjusting the tension and the length between the fixed boundaries, the resonance frequency of the sensor can be tuned to match the external magnetic field frequency, improving the sensor's signal-to-noise ratio and sensitivity.

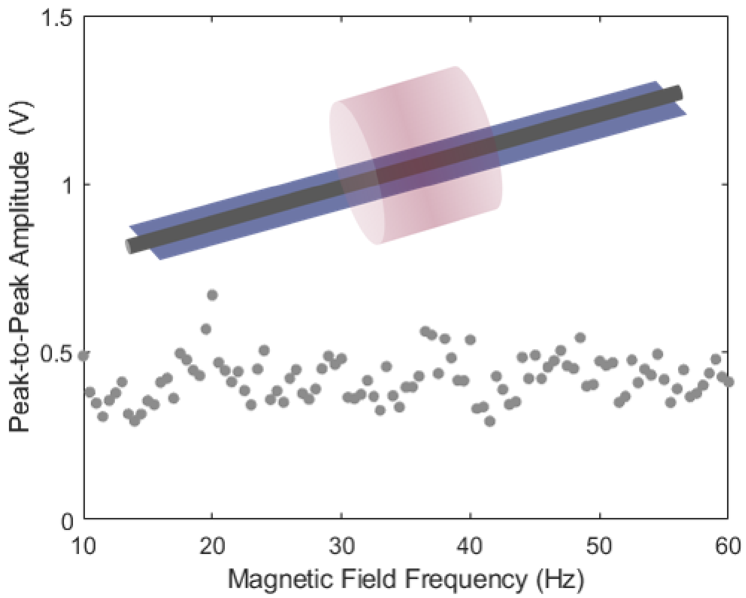

Figure 3-4 Frequency characteristic of sensor with free boundary conditions

However, for multifrequency detection applications and for a general application scenario, a flat frequency characteristic is preferred. Therefore, free boundary conditions should be considered where two ends of the magnetic fiber are left free and the magnetic fiber are placed onto a plastic board crossing the center of the Helmholtz coil (inset image of Figure 3-4). Unlike the case with fixed boundary conditions, the frequency responses of the fiber are relatively flat across the frequency range under testing. The acoustic wave generated by the section of the magnetic fiber within the magnetic field generates traveling wave in the magnetic fiber. As shown in Figure 3-4, less frequency dependencies were observed. For the rest of the measurements, we will consider this case to characterize the sensor’s sensing capabilities on magnetic field measurements.

3.4 Magnetic Field Measurements

Given the sensor's flat frequency response, we selected a 20 Hz magnetic field to characterize its response.

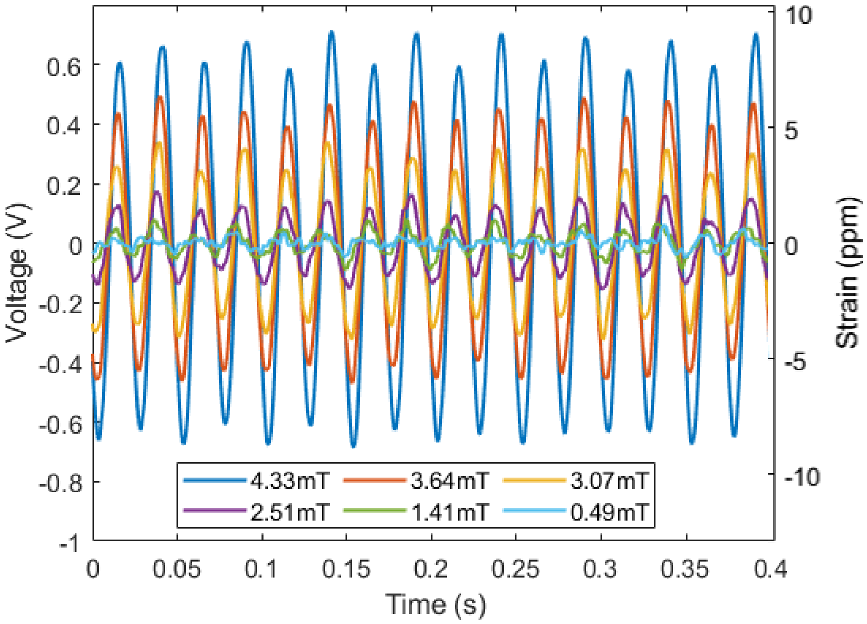

Figure 3-5 Sensor responses under different magnetic field

Here, the balanced photodetector was adjusted to apply a bandpass filter between 10~100Hz. Figure 3-5 shows the measured time domain signal of the sensor under different magnetic field strength after averaging 100 times. It shows that the measured photodetector signal is dominantly a 40 Hz sinusoidal signal, which monotonically increases in amplitude as the external magnetic field increases. With known sensitivity of the FBGs, input laser power, and photodetector responsivity and amplification factors, the measured photodetector voltage signal can be converted to strain estimations, which is plotted in the right y axis in Figure 3-5.

To calibrate the sensor and determine the relationship between strain amplitude and the applied magnetic field, we measured the sensor responses under varying magnetic field strengths, with ~0.5 mT steps at each FBG location under free boundary conditions as previously discussed in Figure 3-6. For each FBG sensor location, five independent measurements were taken with a constant 20 Hz magnetic field. This procedure was repeated for all three fabricated sensors. For each magnetic field strength, five independent measurements were taken, and the error bars in represent the 1σ standard deviation of these measurements. To fit the sensor's magnetostriction relations, a simplified theoretical model using the arctangent function was chosen. Here, the magnetization and magnetostriction property of the Terfenol-D is [73–75]:

$$M = 2 \cdot \frac{M_s}{\pi} \cdot \tan^{-1}(H \cdot k) \tag{3-3}$$

$$\varepsilon(H) = 1.5 \cdot \lambda_s \cdot \frac{M^2}{M_s^2} \tag{3-4}$$

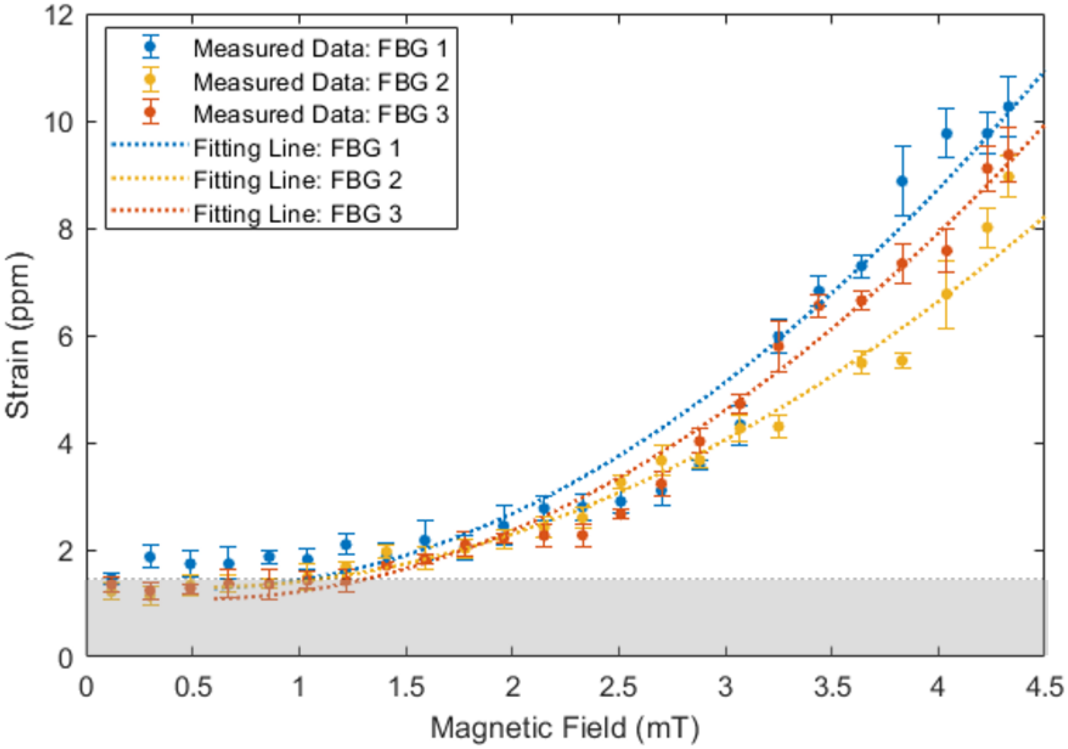

Figure 3-6 Summary on the magnetic field measurements

Where M is the magnetization, M_s is the saturation magnetization, H is the magnetic field strength, k is the relaxation factor, $k = \frac{\pi}{2}\frac{\chi}{M_s}$, χ is the magnetic susceptibility, λ_s is the saturation magnetostriction. To fit the magnetization data from the Terfenol-D particle supplier (TdVib, LLC.), the properties of the Terfenol-D bulk material are listed in Table 3. Due to the nonlinear relationship between the measured magnetostriction over magnetic field at each of the sensor locations, we used the same arctangent function format to characterize the measured magnetostriction effect of the three sensor points and introduced scaling factor a, offset factors H_0, and ε_{off} to fit the measured experimental results.

$$\varepsilon(H) = 6a\lambda_s \cdot \frac{1}{\pi^2} \cdot [\tan^{-1}((H - H_0) \cdot k)]^2 + \varepsilon_{off} \tag{3-5}$$

The fitted parameters for FBG 1-3 were listed in Table 4. According to the measured data in Figure 3-6, the sensor shows a nonlinear response, and the responsivity of the sensor increases as the external magnetic field increases. Here, for FBG 1 to 3, the averaged responsivity over the measured range is $r_1 = 2.37\,ppm/mT$, $r_2 = 1.77\,ppm/mT$, $r_3 = 2.27\,ppm/mT$, respectively, where the measured maximum responsivity is around 4.5 mT, and are $r_1 = 4.5\frac{ppm}{mT}$, $r_2 = 3.3\,ppm/mT$, $r_3 = 4.2\,ppm/mT$, respectively. The noise level of the measured data was measured as around 100 mV with the current detection settings and 100 times average. This is due to the detector noise and can be improved by increasing the average time. With a 1σ standard deviation of around 0.2 ppm, considering the variation in the sensor's responsivity, the resolution of the sensors is approximately 0.1 to 0.12 mT. The primary sources of noise contributing to this resolution are thermal variations, laser output power drifts, and electronic circuit noise. The average sensitivity of the magnetic field sensor reported here is around 2 ppm/mT, which is close to the previously reported unaligned Terfenol-D [31]. However, instead of locally bonding or molding the sensor, this fabrication process successfully demonstrated multi-point magnetic field sensors with a single drawing process.

TABLE 3 MAGNETIC PROPERTIES OF BULK TERFENOL-D

Property	$\mathbf{Tb_{0.3}Dy_{0.7}Fe_{1.92}}$
$\boldsymbol{M_s}$ (kA/m)	700
$\boldsymbol{\lambda_s}$ (ppm)	1050
$\boldsymbol{\chi_m}$	31
$\boldsymbol{B_s}$ (T)	1
$\boldsymbol{\mu_r}$	2-10

TABLE 4 FITTED PARAMETERS FOR SENSORS

Parameters	**FBG 1**	**FBG 2**	**FBG 3**
$\boldsymbol{a}$	0.31	0.23	0.30
$\boldsymbol{H_0}$ (kA/m)	*0.5	*0.5	*0.5
$\boldsymbol{\varepsilon_{off}}$ (ppm)	1.13	1.29	1.08

3.5 Conclusions

In Chapters 2 and 3, magnetostrictive fibers were fabricated using a scalable thermal drawing process. A series of FBGs, written via the Point-by-Point method, was embedded into the magnetostrictive layers to demonstrate multi-point sensing capabilities. After drawing, the fibers had a diameter of around 1 mm and a length exceeding 10 meters. The sensor’s response was measured under different tension using a custom-built interrogation system. The sensor's magnetoelastic and magnetostrictive properties were discussed, and its acoustic properties in a uniform magnetic field were analyzed. Multi-point sensing was demonstrated with a responsivity of up to 4.5 ppm/mT and a resolution of 0.1 mT. The sensitivity among the three sensing points was consistent, indicating good uniformity in the thermal drawing process.

However, the sensor’s capabilities should not be limited to multi-point sensing as suggested by the preliminary tests. With fully distributed sensing mechanisms, these thermally drawn multimaterial fibers have the potential to achieve comprehensive distributed sensing. The multimaterial thermal drawing process effectively integrates silica fiber with low-melting-point materials like polymers. The polymers' excellent encapsulation ability can significantly extend the sensing capabilities of silica fiber. By incorporating different active phases into the composite material, the sensor can be adapted to measure various parameters, such as using pH-responsive materials for pH sensing.

Chapter 4 Fiber-based Stretchable Strain Sensor Analytical Modeling and Fabrications

4.1 Introduction

Soft strain sensors are important components for the application of wearable electronics, structure health monitoring and implantable applications, requiring high flexibility and a wide dynamic range to ensure minimal discomfort and disruption to the monitored structures. Conventional strain sensors made of metals and semiconductors are unsuitable due to their small gauge factor and high rigidity [86,87].

To the data, there are several proposed designs of highly stretchable strain sensors. Classified by their sensing mechanism, it can be subdivided into piezoelectric, triboelectric, optical, resistive, and capacitive sensors. The piezoelectric [88–90] and triboelectric [91] sensors usually have fast charge transfer and cannot work with the low frequency and quasi-static cases in the wearable applications. Optical sensors are usually waveguiding structures which consists of a core and cladding structure. The interrogations are usually transmission-based, where the optical source is connected to one end of the optical waveguided and photodetectors are connected to the other end. Intensities [92–96] and color [14] (spectrum) of the transmitted light are recorded to track the bending and strain. However, the transmission-based interrogation scheme usually needs two-end access which limits the flexibility of the wearable sensor and is unsuitable for long haul detections. Reflection based measurements such as fiber Bragg gratings (FBGs) have been demonstrated, but the stretchability of the sensor is limited, and the interrogation system is complicated and expansive [97,98]. Resistive and capacitive sensors are two types of sensors that have been widely adopted for wearable strain measuring applications.

Stretchable resistive sensors are either soft supporting matrix with conductive fillers like semiconductor material, carbon nanomaterial and metal particles or elastic material with conductive coating [93,99–111]. Upon stretching the resistance of the composite material will change due to the dimensional changes. In addition, large gauge factors can be achieved due to the conductive network disturbance of the composite material or the intrinsic resistance changes of the conductive fillers such as tunneling effects, disconnection effects or cracking growth [112]. However, the resistive sensors usually have large hysteresis due to the viscoelastic effect of the soft supporting matrix and the interaction between the hard supporting fillers and soft matrix. Especially for the case that the fillers and the soft supporting materials have large Young's modulus differences, the delamination of the composite will made irreversible effects on the conductive network and compromise the sensor's stabilities [105]. For wearable applications, dynamic loading, and random strain patterns with various strain rates, holding time and long-time testing are common. Therefore, sensors with low hysteresis and repeatable performance are desired.

Capacitive sensors, on the other hand, have less hysteresis effects. The capacitive sensors usually include a dielectric layer sandwiched between two conductive layers. Under applied voltage, the free charges will distribute on opposite electrodes. Once strain is applied, the free charges will be redistributed along the electrodes. The dominant sensing principles of capacitive sensors are geometrical changes, while the electrode separation distance and the effective overlapping surface area between electrodes change against strain. Independent of conductance of the electrodes, the capacitive sensors usually exhibit low hysteresis. Several stretchable capacitive strain sensors have been proposed by wrapping conductive material around elastic material [113], doping conductive particles into soft matrix [114,115], injecting liquid metal [116,117], or multi-shell printing [118]. However, most of the capacitive sensors have less than 1 gauge factor. This is because depending on the geometrical effects, the theoretical gauge factor upper limit of the capacitive sensor is 1. Further improving the gauge factor involves modifications on the electrode geometries, for example introduce wrinkles [119] and material modifications [120]. However, sensors with geometry and material modifications can't be compatible with scalable fabrications. In addition, the involving soft material as electrodes can still suffer the issue of hysteresis.

Alternatively, hard materials such as solid metals could be incorporated into flexible structures by inter-twisting or winding into helical structures, which can avoid high viscoelasticity but maintains high flexibility and softness. Here we proposed a design of double helical capacitive sensor by winding two rigid conductive wires around the elastic core. Opposed to other proposed double helical capacitive sensors [114,116,121], the double helical sensor proposed requires the pitch length of the helical structure much smaller than the coil diameter. With the dense windings, the straightening of the helical structure under strains extends the stretchability of the rigid material. When voltage was applied to the electrodes of the capacitor, the electric field between electrodes tends to pass along the nearest path. Therefore, the capacitance between the two electrodes of the double coil fiber comes from two neighboring turns instead of opposite turns in Lee, J. *et al.'s* work [114]. The curve surface of the electrodes offers the dense wound double coil fiber has gauge factor (GF) larger than unity, which exceeds the unity limit of gauge factor offered by the planar capacitors [112].This sensor design allows large gauge factor at small strain, which facilitate sensitive sensing without pre-stretching. Eliminating soft material from the electrodes enhances this sensor's hysteresis, repeatability, and response time. With those virtues, we applied these capacitive strains sensor onto the real time detections on multiple psychological signal recordings including body movement, finger posture and breathing, structure health monitoring and implantable applications (shown in the schematic view in Figure 4-1).

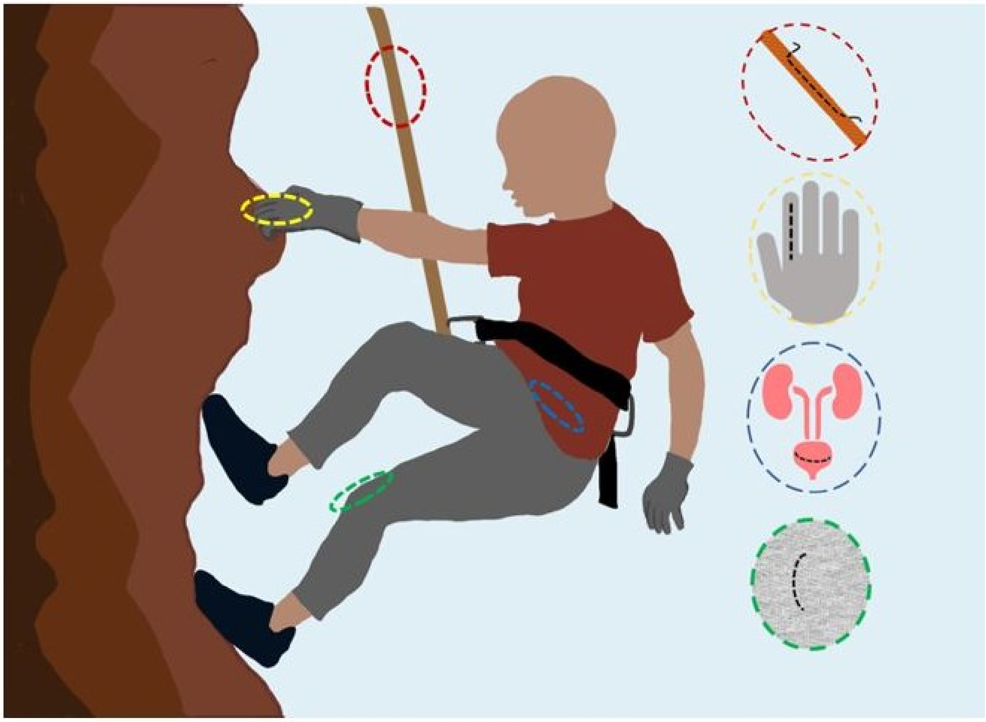

Figure 4-1 Schematic representation of the multifunctional fiber strain sensors integrated into life safety ropes, gloves, clothing, and implantable applications.

4.2 Equivalent Impedance Model for double Coil Structure

For the double coil structure proposed here, we built a simplified equivalent impedance model to understand its electrical properties.

4.2.1 Equivalent Impedance Network Model of the Double Coil Fiber:

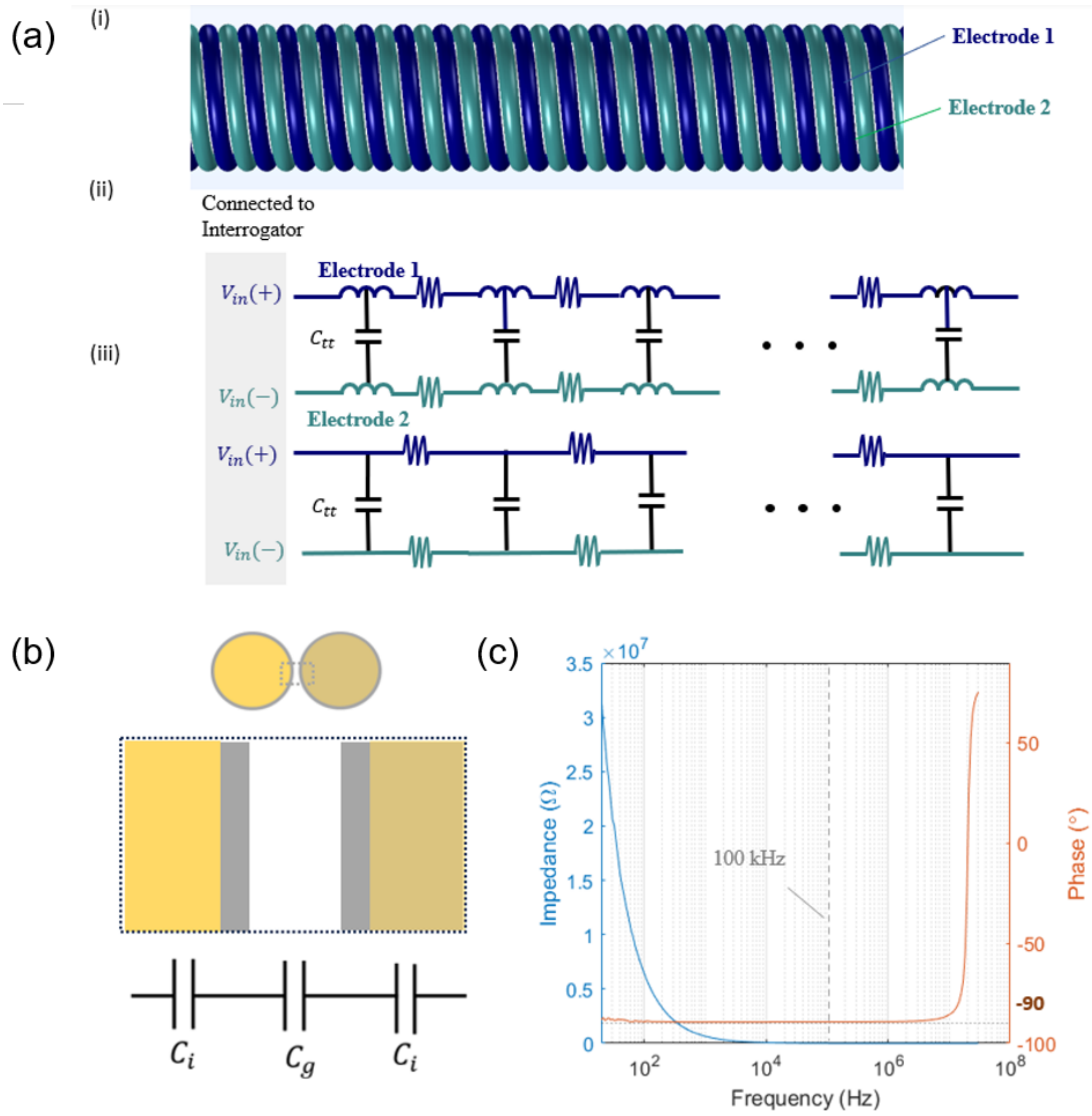

Figure 4-2 Equivalent Impedance Network of the Double Coil Fiber (a) Transmission line model for the open-ended double coil structure (b) Turn to turn capacitance model (c) Impedance measurement of double coil fiber as a function of frequency.

With open-ended double coil fiber, when a voltage $V_{in}+$ was applied to one electrode and $V_{in}-$ to another electrode on the same end, the double coil fiber can be modelled using a transmission line model in Figure 4-2(a) (ii). Measured by the impedance analyzer, when the input frequency is under 1 MHz, the impedance of this circuit is close to -90°, which means that the circuit's inductance can be ignored. For the rest of the investigations, our interrogation frequency is 100 kHz. Therefore, we ignore the inductance units in the circuit, the circuit model can be further simplified to Figure 4-2 (a) (iii).

However, as a comparison and to fully understand the working principle of the double coil structure. We should compare the case with closed ended cases to the open-ended cases discussed in this paper. For the close ended case, we connected two electrodes from one end of the double coil structure to the impedance analyzer and connected the far ends of the coil. Figure 4-3 shows the same double coil structure with (a) the connected cases and (b) the unconnected cases. For the connected cases, its circuit model can be simplified to the circuit model in the inset image when frequency is under 20 MHz. When frequency is under 10 kHz, most of the impedance is due to the resistance effects. Between 10 kHz to 10 MHz, the circuit's impedance is inductive dominant, and its inductance increases. Between ~10 MHz to 16.2 MHz, the impedance decreases as the impedance of the capacitance decreases. Later, at 16.2 MHz, the impedance due to the capacitance is the same as the impedance from the inductance, and this is the circuit's self-resonant frequency. After 20 MHz, the circuit model of the double coil fiber with ends connected cannot be simplified by a simple circuit model. When the far ends of the double coil fiber were unconnected, its measured impedance is plotted in Figure 4-3 (b). To simplify the problem, for the content of this chapter, we only investigated the case of the double coil fiber with the far ends open.

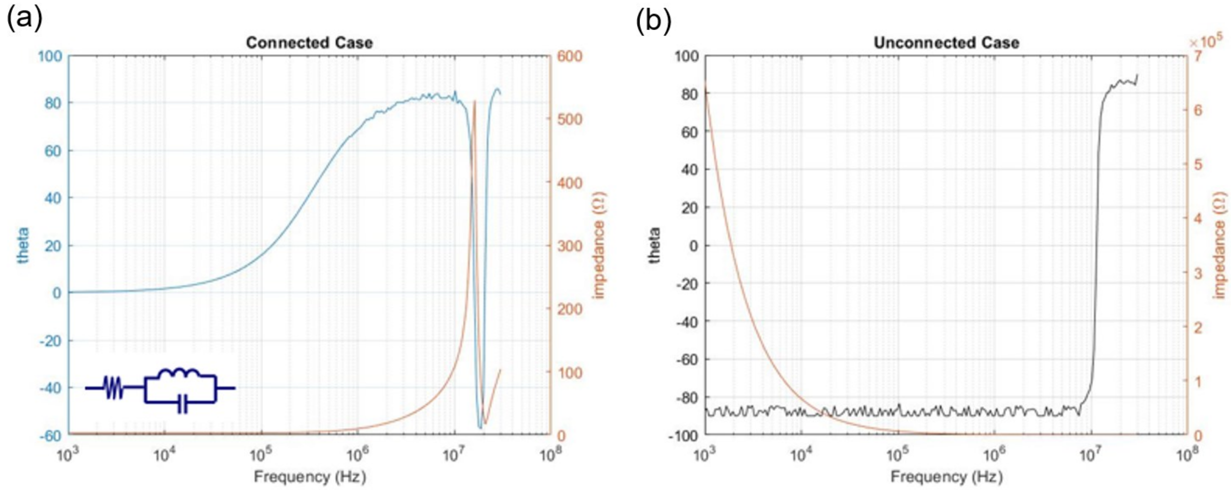

Figure 4-3 Impedance measurement of double coil fiber as a function of frequency for (a) connected end case (b) unconnected end case.

4.2.2 Modeling of Double Coil Capacitive Sensor

To better understand the working principle of the densely wound double coil sensor and quantify the relative capacitance change as a function of strain, an analytical expression was derived. The analytical expression predictions were then compared with the Finite Element Analysis (FEA) simulations as well as experimental measurements to verify its accuracy.

The schematic view of the double coil strain sensor is presented in Figure 4-4(a) with one turn of helical structure highlighted in red. The length of a single turn of the coil is:

$$l_t = \sqrt{\left(\pi d_{coil_0}\right)^2 + (2\Lambda_0)^2} = \sqrt{(\pi(D_0 + d))^2 + (2\Lambda_0)^2} \qquad \text{(4-1)}$$

Where d_{coil_0} is the major diameter of unstretched the coil structure, d is the diameter of the unstretched elastic core, D_0 is the diameter of the conductor, and the winding angle under unstretched condition is:

$$\alpha_0 = \arctan\left(\frac{\pi(d + D_0)}{2\Lambda_0}\right) \qquad \text{(4-2}$$

)

With external tensile strain ϵ applied to the elastic core, the double coil will not apply pressure onto the elastic core in the lateral direction, but it will follow the expansion of the core and straighten its windings while keeping the length of a single turn a constant value. The winding angle will decrease to:

$$\alpha = \arctan\left(\frac{\pi d_{coil}}{2\Lambda}\right) = \arctan\left(\frac{\pi d_{coil}}{2(1+\epsilon)\Lambda_0}\right)$$

(4-3

)

Where d_{coil} is the major diameter of the coil structure after stretching:

$$d_{coil} = \frac{\sqrt{l_t^2 - (2\Lambda)^2}}{\pi}$$

(4-4

)

When the winding angle (α) is less than 45°, it corresponds to a scenario of sparse winding. In this case, the electric field predominantly distributes between two facing turns that across the elastic core, and the capacitance arises from the spacings between these two facing turns [114]. In contrast, for the sensor discussed here, the two electrodes are densely wound around the elastic core with the winding angle α significantly greater than 45° so that the electric field predominantly distributes between adjacent turns, resulting in turn-to-turn capacitance being dominant.

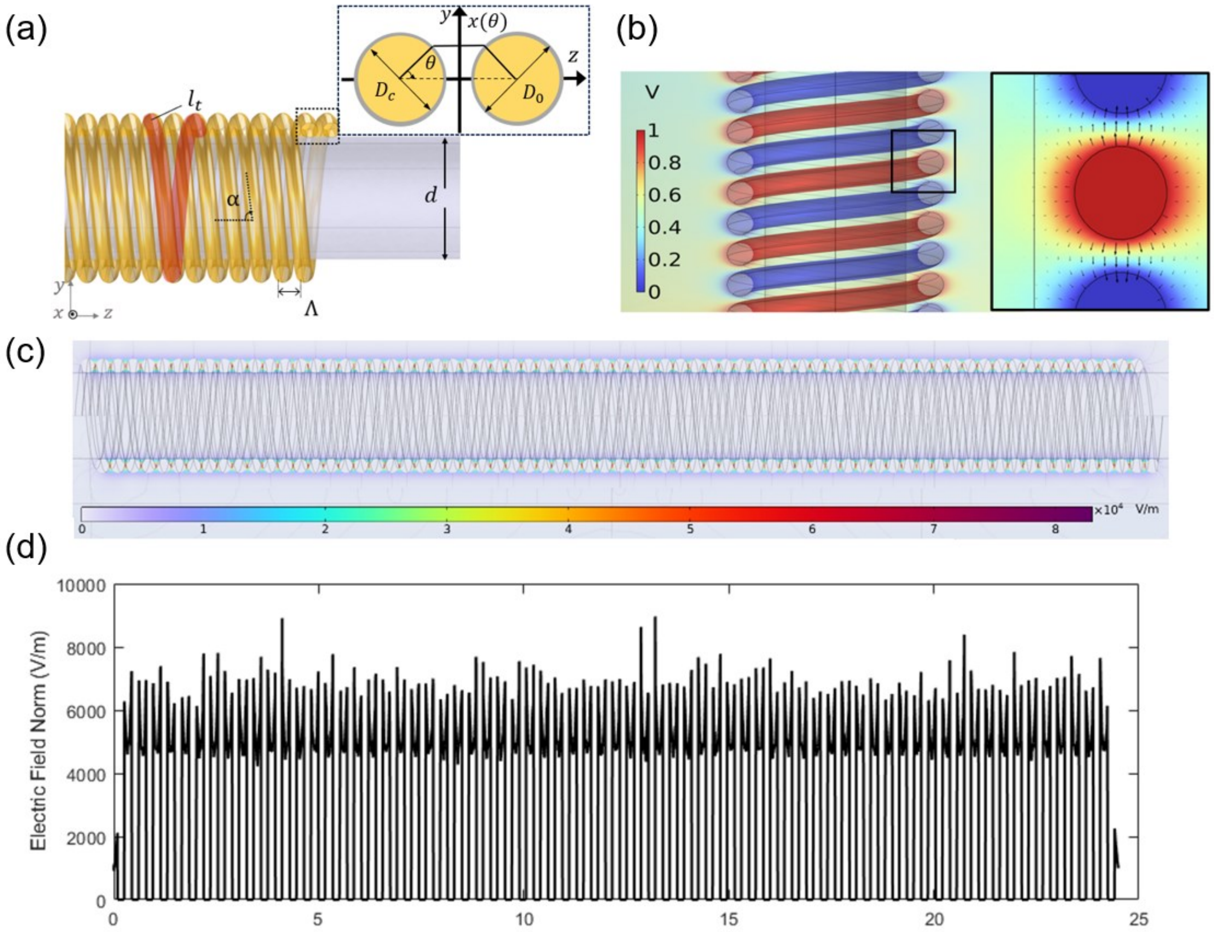

Figure 4-4 FEA simulation results of the double coil fiber (a) Schematic representation of the double coil fiber with key geometric parameters marked. Inset: Schematic cross-section of consecutive electrodes with insulating coating. (b) Numerical simulations showing electric field distributions in the double coil fiber, highlighting voltage distribution and electric field direction within one turn. The arrows represent electric field distributions, with the length of each arrow corresponding to the electric field strength in logarithmic scale. (c) Cross-section of the 3D FEA simulation results of electric field distributions around the double coil fiber. (d) Electric field distributions along the center of the electrodes, showing the periodic distribution of the electric field between turns.

To further confirm our analysis on the electric field distributions, FEA models were built to analyze the electrical field distributions between the electrodes. The simulation results, presented in Figure 4-4 (b), illustrate that the electric fields distribute periodically (shown in Figure 4-4 (c)(d)) and concentrate primarily between adjacent turns, and within two turns, the center of the circular shape exhibits the strongest amplitude of electric field. To further comprehend the relationship between the lump and turn-to-turn capacitance, we experimentally measured and plotted the total capacitance of the double coil structure against the number of turns, as shown in Figure 4-5(a). As the number of turns exceeds 60, the total capacitance linearly increases with a slope of 358 *fF/*rad. The deviation from the linear relationships with less than 60 turns possibly comes from the significant impact of the stray field near the ends of the double coil structure. Therefore, the modeling of lump capacitance changes can be simplified to modeling the turn-to-turn capacitance changes. A circuit model and impedance measurements of the double capacitor structure presented in Figure 4-2 further confirm our conclusions:

$$\frac{\Delta C}{C_0} = \frac{C - C_0}{C_0} = \frac{C_{tt} - C_{tt0}}{C_{tt0}} \tag{4-5}$$

In the given expressions, C_0 and C represent the initial lump capacitance and the lump capacitance after stretching, respectively. Likewise, C_{tt0} and C_{tt} denote the initial turn-to-turn capacitance and the turn-to-turn capacitance after stretching.

An analytical model of the turn-to turn capacitance is derived by referring to the model of the self-capacitance and parasitic capacitance of inductors [122–127]. The cross-section of one pair of adjacent turns is presented in the inset of Figure 4-4 (a). The capacitance between two adjacent turns can be treated as the capacitance of the insulating layer C_i in series with the capacitance of the gap between the electrodes C_g (shown in Figure 4-2(b)). Considering an elementary cell of the insulating layer, the capacitance is expressed as:

$$dc_{io} = \frac{r\varepsilon_{ri}\varepsilon_0 d\theta dl}{dr} \tag{4-6}$$

where ε_{ri} and ε_0 are the relative permittivity of the coating material and free space permittivity respectively. The unit capacitance per angle is given by integrating (4-6) over radius r from conductor radius $r_c = \frac{D_c}{2}$ to coating radius $r_0 = \frac{D_0}{2}$ and over length l from 0 to the length of one turn s_0:

$$\frac{dc_{io}}{d\theta} = \varepsilon_{ri}\varepsilon_0 \int_0^{l_t} dl \int_{r_c}^{r_0} \frac{r}{dr} = \frac{\varepsilon_{ri}\varepsilon_0 l_t}{\ln\left(\frac{r_0}{r_c}\right)} \tag{4-7}$$

According to the FEA simulation results of the electric field distribution in Figure 4-4(b), the electric field is non-uniformly distributed within the gap of two adjacent turns due to the curvature of the electrode. For simplicity, the capacitance at the gap between the electrodes is analyzed under the assumption that the electric field follows the shortest possible distance between the electrodes and the total capacitance between the curvature can be divided into elements of capacitance in parallel with each other, which is a reasonable assumption referring to the electric field directions presented by arrows in Figure 4-4(b). The distance between the electrodes is a function of the angle *θ*, where the separation is:

$$x(\theta) = \Lambda - D_0 cos\theta = \Lambda_0 * (1 + \epsilon) - D_0 cos\theta \tag{4-8}$$

Therefore, for a unit angle *dθ,* the capacitance is:

$$\frac{dC_{g0}}{d\theta} = \frac{\varepsilon_0 \varepsilon_{rg} l_t}{2} \frac{1}{\frac{\Lambda}{D_0} - cos\theta} \tag{4-9}$$

where Λ_0 is the spacing between the center of two adjacent turns before stretching, and ε_{rg} is the relative permittivity of the gap at the angle θ. The capacitance between two electrodes can be equivalently treated as three capacitance in series (Figure 4-4): C_{i0}, C_{g0}, and C_{i0}, so that the total capacitance for one turn dC_{unit} is:

$$\frac{1}{dC_{unit}} = \frac{1}{dC_{i0}} + \frac{1}{dC_{g0}} + \frac{1}{dC_{i0}} \tag{4-10}$$

$$\frac{dC_{unit}}{d\theta} = \frac{\varepsilon_0 l_t}{2} \frac{1}{\frac{1}{\varepsilon_{ri}} \ln\left(\frac{r_0}{r_c}\right) + \frac{1}{\varepsilon_{rg}} (\frac{\Lambda}{D_0} - cos\theta)} \tag{4-11}$$

The turn-to-turn capacitance for one turn is the integration over *-π/2* to *π/2.* As shown in Figure 4-4 (b), the electric field is mainly distributed in the air gap between the turns, and only the stray field at the two ends of the double coil structure crosses through the elastic core. For all the cases we discuss here, the turns are stacking tightly, the effects of the stray electric field near the two ends of the double coil structure are ignored. For the turn-to-turn capacitance between two turns (highlighted in Figure 4-4 (a)), the total capacitance of the capacitor is calculated by integrating the capacitance across all the angles θ. As an approximation, we assume that the dielectric material between the electrodes is air with a relative permittivity taken as:

$$\varepsilon_{rg} = 1 \tag{4-12}$$

The total turn-to-turn capacitance between one pitch of the coil is calculated as:

$$C_{tt} = \int_{-\frac{\pi}{2}}^{\frac{\pi}{2}} C_{unit} d\theta$$

$$= \int_{-\frac{\pi}{2}}^{\frac{\pi}{2}} \frac{\varepsilon_0 l_t}{2} \frac{1}{\frac{1}{\varepsilon_{ri}} \ln\left(\frac{r_0}{r_c}\right) + \frac{1}{\varepsilon_{rg}} (\frac{\Lambda}{D_0} - cos\theta)} d\theta \tag{4-13}$$

$$= \frac{4b}{\sqrt{a^2 - 1}} \arctan\left(\frac{\sqrt{a+1}}{\sqrt{a-1}}\right)$$

where $a = \frac{1}{\varepsilon_{ri}} \ln\left(\frac{r_0}{r_c}\right) + \frac{\Lambda}{D_0}$, and $b = \frac{\varepsilon_0 l_t}{2}$.

Substituting the turn-to-turn capacitance expressions from (4-13) into the calculations for relative capacitance change in Equation (4-5), we calculated the relative capacitance changes under different strains.

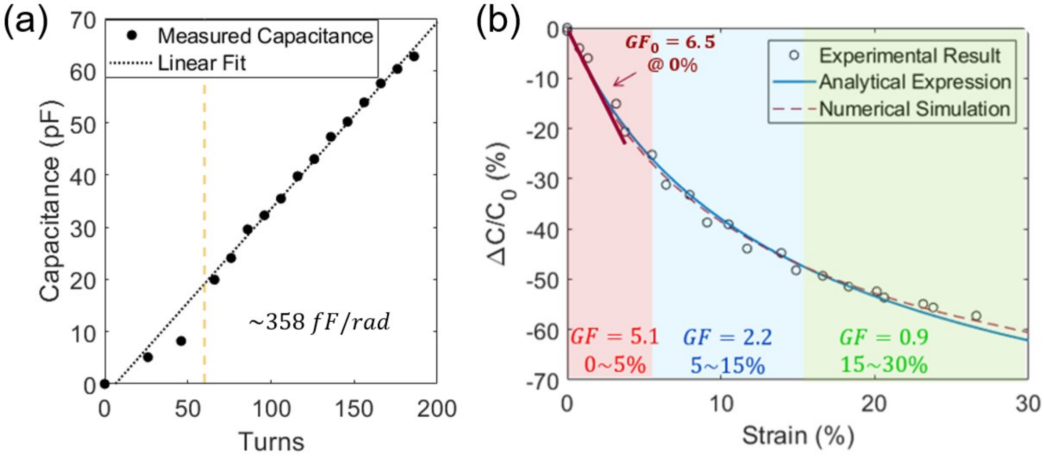

Figure 4-5 (a) Measured lump capacitance of the double coil fiber as a function of the number of turns and linear regressions. (b) Relative capacitance changes under different strains. The analytical expressions (solid line, equation 3-13) show good consistency with experimental data (dots), and numerical simulations (dash line).

The analytical capacitance expressions are plotted alongside FEA simulations and experimental measurements in Figure 4-5(b). The analytical expressions show excellent agreement with the FEA simulations and the experimental results in the tested range, justifying our analysis. In the context of dense windings, the sensor has the best sensitivity at small strain and then the gauge factor decreases after stretching. For the sensor design we presented here, the maximum GF is up to 6.5 in the tiny strain range, while the averaged GF is 5.1 under 0%~5% strain, 2.2 under 5%~15% and 0.9 under 15%~30% strain. This exceeds the maximum achievable unity GF of the parallel-plate structure capacitive sensor [112,119,128] and demonstrates higher sensitivity than the reported capacitive sensor at small strains [113–115,129–132].

4.3 Design Considerations of the Double Coil Fiber

4.3.1 Coil Density Choices

To further understand the sensor's sensitivity and its dependency on strain and the density of the coil, i.e. pitch length Λ_0, we plotted the relative capacitance changes as a function strain with different pitch lengths in Figure 4-6 (a). To quantify the sensitivity, we calculated the gauge factors of the sensor by taking the derivative of the relative capacitance changes with respect to strain and plotted the gauge factor in the inset plot. As it is shown by Figure 4-5 (b) and Figure 4-6(a), the sensitivity decreases as the strain increases. We thus define the operative stretchability as the strain range that has higher sensitivity than a required sensitivity level. As an example, we marked the operative stretchability for $S=3$ in Figure 4-6 (a). For denser pitch length cases, the sensor tends to have higher sensitivity and larger operative stretchability for a given required sensitivity. Therefore, unlike sparse winding cases [114], in the context of dense winding, the sensor can increase both operative stretchability and sensitivity simultaneously by increasing its pitch density.

4.3.2 Coil and Elastic Core Diameter Choices

The geometrical choice of elastic core and coil diameters are based on the considerations of sensor performance, durability, material availability and manufacturability.

To understand how the diameters of the elastic core and the wires change the sensor performance, we swept those parameters and plotted the sensor's response using the theoretical relationships. Under the condition of *densely* coiled case, where the turn-turn capacitance follows equation (4-14) in the main text:

$$C_{tt} = \int_{-\frac{\pi}{2}}^{\frac{\pi}{2}} C_{unit} d\theta$$

$$= \int_{-\frac{\pi}{2}}^{\frac{\pi}{2}} \frac{\varepsilon_0 l_t}{2} \frac{1}{\frac{1}{\varepsilon_{ri}} \ln\left(\frac{r_0}{r_c}\right) + \frac{1}{\varepsilon_{rg}} (\frac{\Lambda}{D_0} - cos\theta)} d\theta \qquad (4\text{-}14)$$

$$= \frac{4b}{\sqrt{a^2 - 1}} \arctan\left(\frac{\sqrt{a+1}}{\sqrt{a-1}}\right)$$

where $a = \frac{1}{\varepsilon_{ri}} \ln\left(\frac{r_0}{r_c}\right) + \frac{\epsilon\Lambda_0}{D_0}$, and $b = \frac{\varepsilon_0 l_t}{2}$.

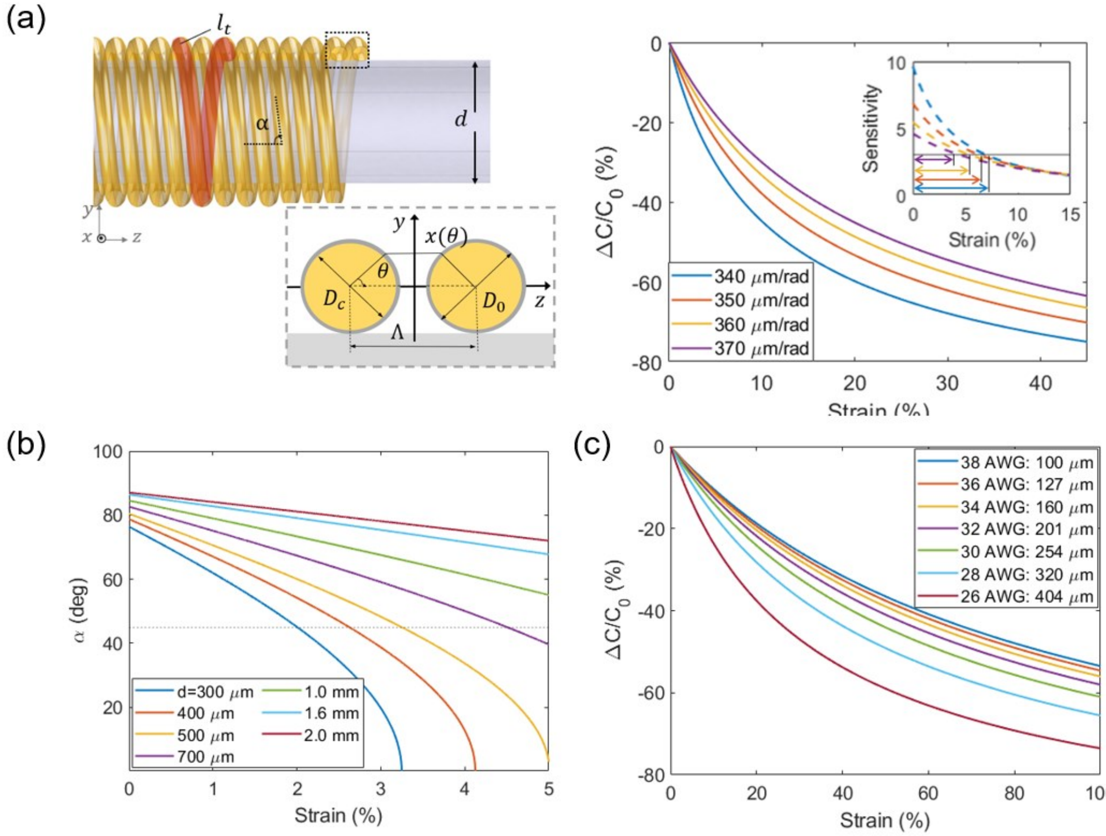

Figure 4-6 (a) Capacitive and sensitivity response of the sensor with different pitch densities. (b) Winding angle as function of strain with different pitch length. (c) Capacitive response of the sensor with different wire diameters.

Elastic core diameter *d*: the turn-to-turn capacitance is independent of the elastic core diameter. However, the density of the winding is characterized by the winding angle (α), where $\alpha = \arctan\left(\frac{\pi d_{coil}}{2\Lambda}\right) = \arctan\left(\frac{\pi d_{coil}}{2\epsilon\Lambda_0}\right)$, we plotted the relationship between the winding angle α and the strain with different elastic core diameters in (4-6) (b). As it is discussed by the theoretical model of the double coil fiber, our condition of densely wound requires the winding angle greater than $45°$. While keeping the winding density at a constant value, a smaller core diameter will have less operational strains under the densely wound conditions.

Coil diameter D_0: according to equation (4-14), the turn-to-turn capacitance is a function of the ratio between the pitch length and the wire diameter Λ/D_0. While keeping this ratio as a constant value, scaling down and up the coil diameter will not change the sensor's performance. Like Figure 4-6 (a), we picked the wire diameters varied between 26 AWG to 38 AWG and plotted the relative capacitances changes and sensitivity of the sensor as a function of the strain (Figure 4-6 (c)). While keeping the pitch length as a constant value, decreasing the wire diameter will decrease the sensor's sensitivity.

In addition to considering the sensor performance, we also take the sensors' durability, material availability and manufacturability into considerations: a small elastic core diameter and coil diameter will compromise the sensor's durability and challenge the manufacturing process. On the other hand, a larger core and conductive wire will compromise the flexibility of the sensor and increase its stiffness. In our case, we designed sensors for wearable, biomedical and structural health monitoring applications, where the sensor needs to possess a balance of flexibility and durability. We chose 1 mm elastic core and 34 AWG conductive wires for demonstrations. However, with the general analytical expressions derived, double coil capacitive sensors should not be limited to dimensions outlined in the paper, allowing for tailored designs based on specific application requirements.

4.4 Fabrication of the Double Coil Fiber Sensor

To demonstrate the double coil capacitive sensing idea, we fabricated the capacitive sensor by winding the insulted copper wire around a stretchable core, illustrated by the schematic view in Figure 4-7(a). The elastic core which is driven simultaneously by a linear motor and a rotator (not shown in this figure) rotates with angular speed ω_R and translates with speed v_L. Two parallel conductive wires from the wire spools pass the clamp and attach to the dielectric elastic core. With the stress applied by the clamp, the two conductive wires are firmly wound around the elastic core. We define the pitch length Λ_0 as the separation between two consecutive turns and equal to the ratio between the translation speed and the rotational angular speed:

$$\Lambda_0 = \frac{\pi}{\omega_R} v_L \tag{4-15}$$

One example of the fabricated double coil fiber is shown in Figure 4-7 (b) and Figure 4-7c). The electrodes of the double coil capacitor are insulted copper wires (ELS, 34 AWG, uncoated diameter 160 μm) with 175 μm pitch length (350 μm/rad) and 1 mm elastic core. Image of the unstretched (left) and 100% stretched sensors (right) are shown in Figure 4-7 (b), along with the microscopic images in Figure 4-7 (c). Following the same definition conventions from J. et al.'s work [114], we define a winding angle, denoted as α, to quantify the density of the windings. Here, the winding angle is approximately 90°as the coil is densely wound.

Two types of elastic cores were chosen in this work: the polyester (PES) elastic core was chosen for sensor characterizations and structural health monitoring applications as it has good stability and durability. The thermally drawn (Figure 4-8) thermal plastic elastomer (TPE, styrene and ethylene/butylene, SEBS) fibers with 1 mm diameter were used in implantable applications to extend the stretchability, minimize disruptions, and increase the sensitivities of the sensor. Although the electrodes of the sensor are stiff materials, the sensor has good flexibility (Figure 4-7 (d)) and stretchability due to the dense coil structure. The densely wound sensor can undergo significant expansions while the conductive wires have no plastic deformations due to the dense winding and the large span of the coil.

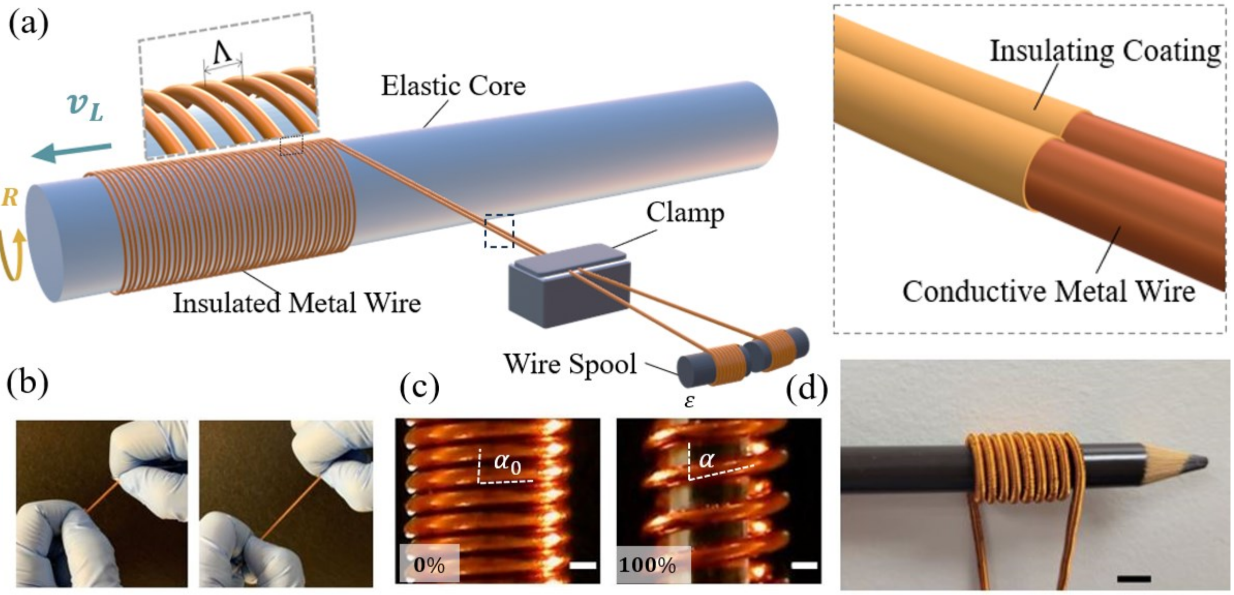

Figure 4-7 (a) Schematic detailing the fabrication process of the double coil fiber. The double coil structure was wound onto the stretchable core by synchronized motion of the linear motor and rotator. Zoomed-in view highlights the structure of the insulated copper wires. (b) Comparison photographs and (c) microscopic images of the double coil fiber under 0% (left) and 100% stretching (right), demonstrating its flexibility and stretchability. The unstretched double coil fiber sensor has a 1 mm diameter stretchable core and 160 µm insulated copper wires with 350 µm/rad windings (scale bar, 200 µm). The winding angles α are highlighted in the picture with $\boldsymbol{\alpha_0} \approx \mathbf{85}°$ and $\boldsymbol{\alpha} \approx \mathbf{80}°$. (d) Photograph of a double coil sensor wound around a pencil (scale bar, 5mm).

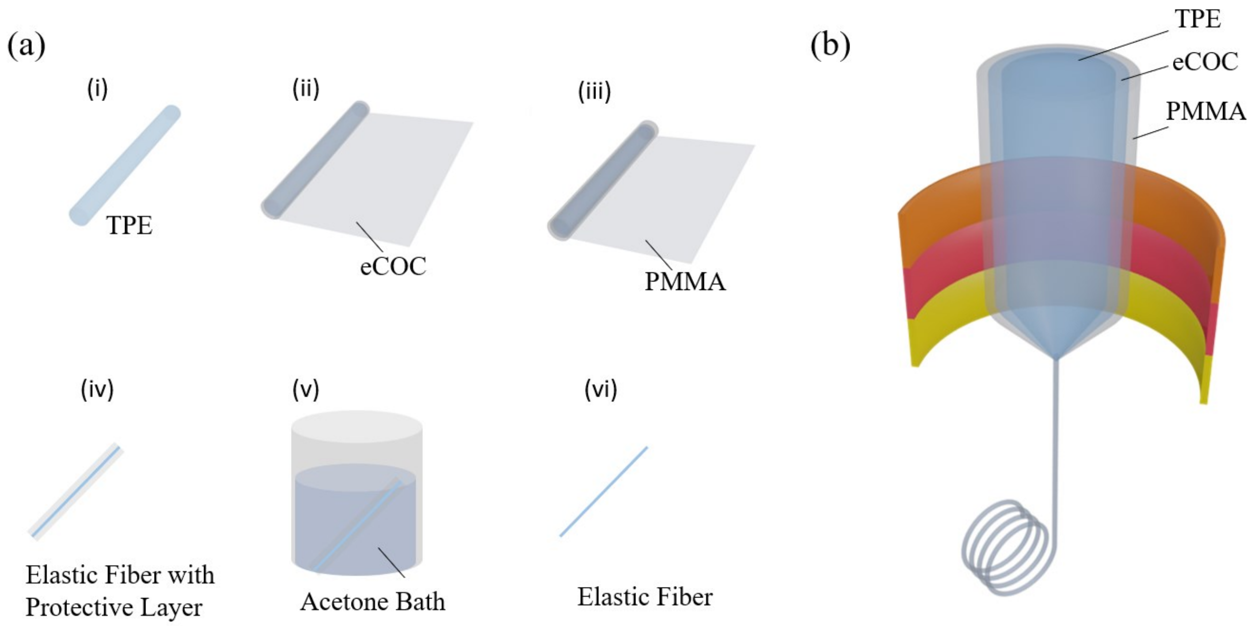

Figure 4-8 Elastic Fiber Fabrication Process (a) The preform fabrication process of the elastic fiber for implantable and wearable applications. (i) The thermal plastic elastomer (TPE, SEBS) polymer pellets were consolidated in the oven at 190 ℃ to form a rod. (ii) The TPE rod was then rolled by a thin film of eCOC fabricated by hot press at 200 ℃, (iii) followed by another layer of PMMA to serve as the sacrificial layer. (b) Schematic of thermal drawing process. (iv) Schematic of thermally drawn fiber (v) Acetone bath of the produced fiber to etch away the sacrificial layer (vi) Fabricated elastic fiber.

Chapter 5 Fiber Based Stretchable Strain Sensor Characterizations and Applications

5.1 Mechanical Property Characterizations

With both ends of the coil structure glued to the elastic core, the double coil conductive wires follow the elongation and retraction of the elastic core. Notably, the mechanical properties of the sensors, illustrated in the strain-stress relations in Figure 5-1, are primarily dominant by the elastic core, where the coil structure exerts minimal impact on the overall mechanical properties. The mechanical hysteresis at different strain ranges is due to the viscoelasticity of the elastic core, which is typical for soft and stretchable strain sensors. However, the capacitance of the double coil fiber, which is a function of overlapped area and wire separations, is independent on the strain-stress relations and exhibits low hysteresis. Detailed hysteresis analysis will be presented in the following sections. Mechanical Property Characterizations

(1) Strain-stress Relations.

The double coil's mechanical properties were characterized by dynamic mechanical analyzer (DMA Q800). In tensile test mode, the mechanical properties of the pure elastic core with and without the double coil structure were tested and plotted in Figure 5-1 (a) and Figure 5-1 (c) respectively. The comparison between the cases with and without double coil structures shows that the additional double coils have minimal impact on the fiber's overall mechanical properties. In Figure 5-1 (a), the cases with double coil structure show similar tensile strength compared with the cases without the coil structure. In Figure 5-1 (b), cyclic tests with various strain ranges for cases with and without coil structures are plotted and compared. Both the cases with and without the double coil structure would exhibit hysteresis. To quantify the hysteresis, we use the value of H_p to quantify the hysteresis in the stress-strain curves, which is defined as the ratio of the difference area between the loading A_L and unloading curves A_U: [133]

$$H_p = \frac{A_L - A_U}{A_L} \tag{5-1}$$

The comparison on H_p shows that the mechanical hysteresis of the fiber is dominant by the elastic core and the double coil structure has minimum impact on the overall hysteresis.

In addition, we did additional tests on the fibers' mechanical stabilities by applying cyclic strain between 2%~30% and recorded the stress responses in Figure 5-1 (d). As shown in the figure below, both the double coil sensor with PES and TPE core exhibit repeatable responses after the first few cycles.

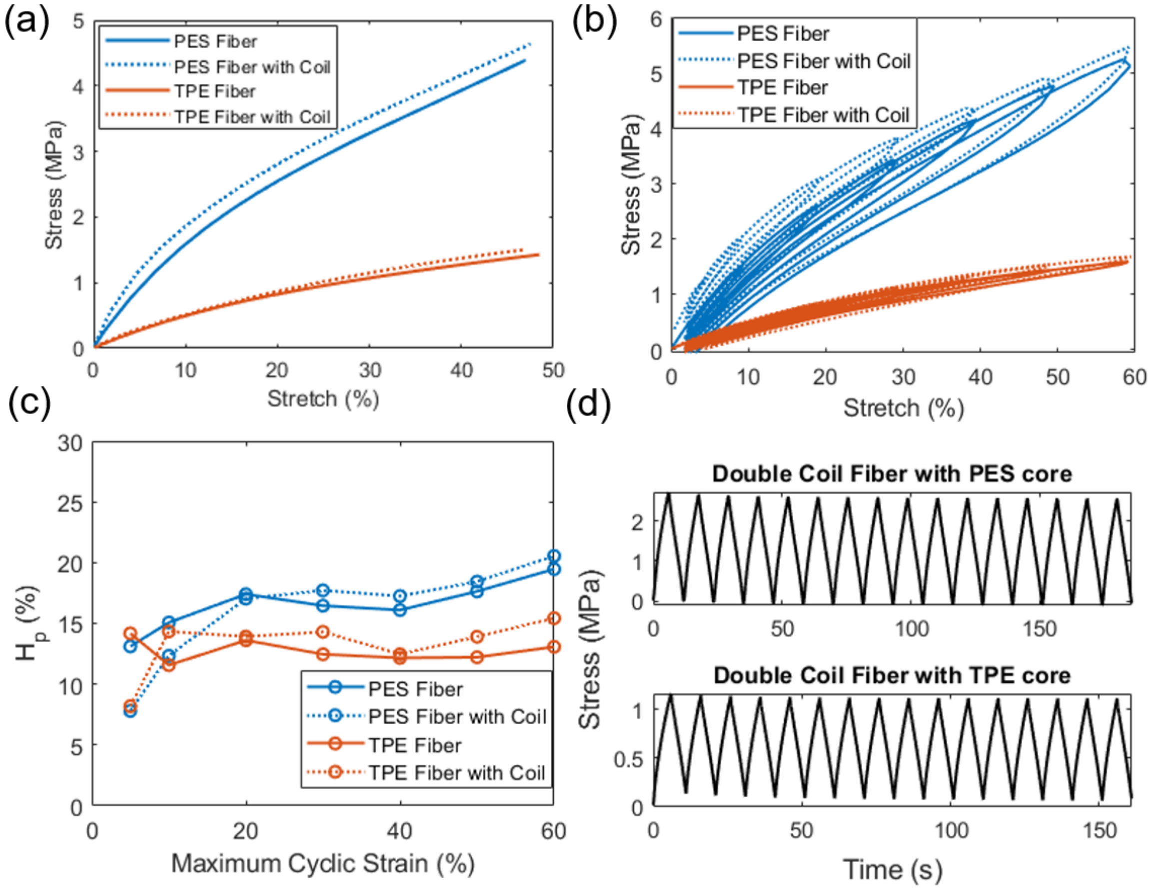

Figure 5-1 Mechanical Properties of the Double Coil Fiber (a) Comparison on the stress-strain curves for bare cores made of PES and TPE (poly(styrene-(ethylene-co-butylene)-styrene) triblock copolymer, SEBS) and cores with double coil structures, which shows that the double coil structure has minimum impact on fiber's tensile strength. (b) Stress−strain curves of bare elastic cores (PES and TPE), showing hysteresis under 10%, 20%, 30%, 40%, 50%, and 60% strain cycles. (c) Hysteresis percentage ($\boldsymbol{H_p}$) of the cyclic tests with different maximum cyclic strains. (d) Cyclic strain- stress measurements on double coil fiber with PES and TPE cores.

(2) Flexural Stiffness.

Over 50 cycles of bending tests were performed on the double coil elastic fiber with a bending radius of 6 mm, which is close to the bending radius for wearable applications. In Figure 5-2(a), the images of the double coil fiber bending at the 1st and 50th cycles are presented. It shows that the sensor has no plastic deformations after bending. Additionally, we measured the flexural strength of the double coil fiber and compared it with 1 mm polymethyl methacrylate (PMMA) in Figure 5-2((b). It shows that the double coil fiber fabricated here is much lower stiffness compared to the 1 mm PMMA fiber. Additionally, the double coil fiber with TPE core has less flexural strength compared to the cases with PES cores, making it a good candidate for strain sensing in wearable and biomedical applications.

(3) Elastic Limit of the Coil Structure.

For each of the coil wounded onto the elastic core, the shear stress τ onto the coil follows:

$$\tau = \frac{8kPd_{coil}}{\pi D_o^3} \tag{5-2}$$

And the conditions for elastic deformation of the coil structure is:

$$\tau < \tau_a \tag{5-3}$$

k is the Wahl stress concentration factor [134]:

$$k = \frac{4d_{coil} - D_0}{4(d_{coil} - D_0)} + \frac{0.615D_0}{d_{coil}} \tag{5-4}$$

and P is the loaded deflection equation:

$$P = K\delta \tag{5-5}$$

K is the spring constant of the coil:

$$K = \frac{D_0^4 G}{8d_{coil}^3 N} \tag{5-6}$$

Where D_0 is the diameter of the wire, d_{coil} is the diameter of the coil structure, τ_a is the yield shear stress of the coil material, G is the shear modulus of the wire material, N is the number of turns, δ is the deflection of the coil along its axis, where:

$$\delta = \varepsilon L = \varepsilon N * \Lambda_t \tag{5-7}$$

$$P = K\delta = \frac{D_0^4 G}{8d_{coil}^3 N} \cdot \varepsilon N * \Lambda_t = \frac{D_0^4 G}{8d_{coil}^3} \cdot \varepsilon * \Lambda_t \tag{5-8}$$

Where ε, Λ_t are the strain and the pitch length per turn of the coil structure. Here we plotted the shear stress of the coil structure as a function of strain when the copper wire diameter is 160 μm, and coil diameter are 0.9 mm, 1.16 mm, and 1.5 mm respectively. The yield shear stress was taken as 175 MPa [135]. In our designed case, where the elastic core diameter is 1 mm, the elastic limit of the coils in the structure equals 53%.

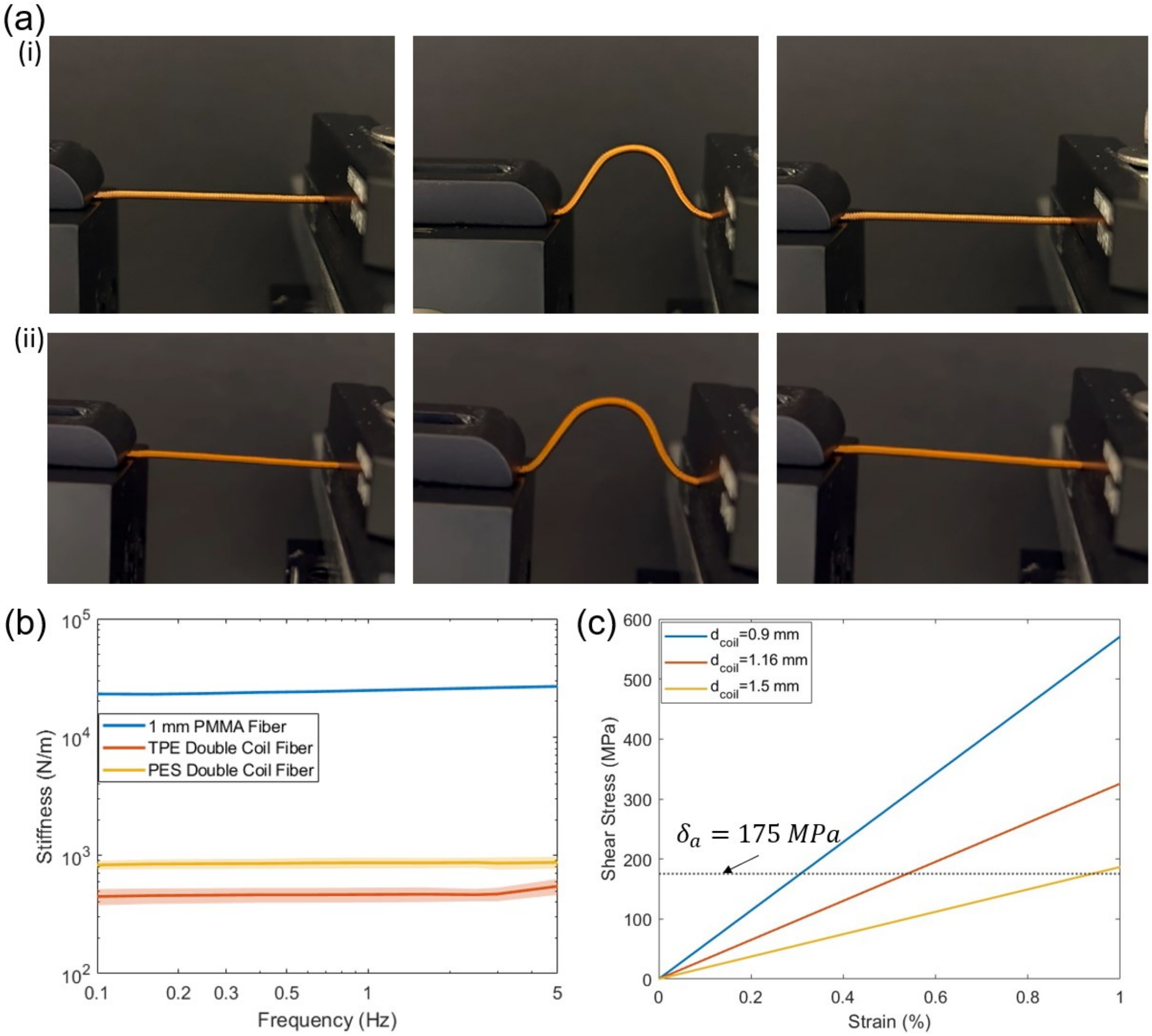

Figure 5-2 Double Coil Fiber Softness Measurement (a) Bend-stretch testing over 50 cycles. From left to right: (i) 1st bending cycle, and (ii) 50th bending cycles. (b) Bending stiffness measurements of TPE coil double coil fibers, and PES double coil fibers. (c) Elastic limit of the double coil fiber with different pitch length.

5.2 Electrical Property Characterizations

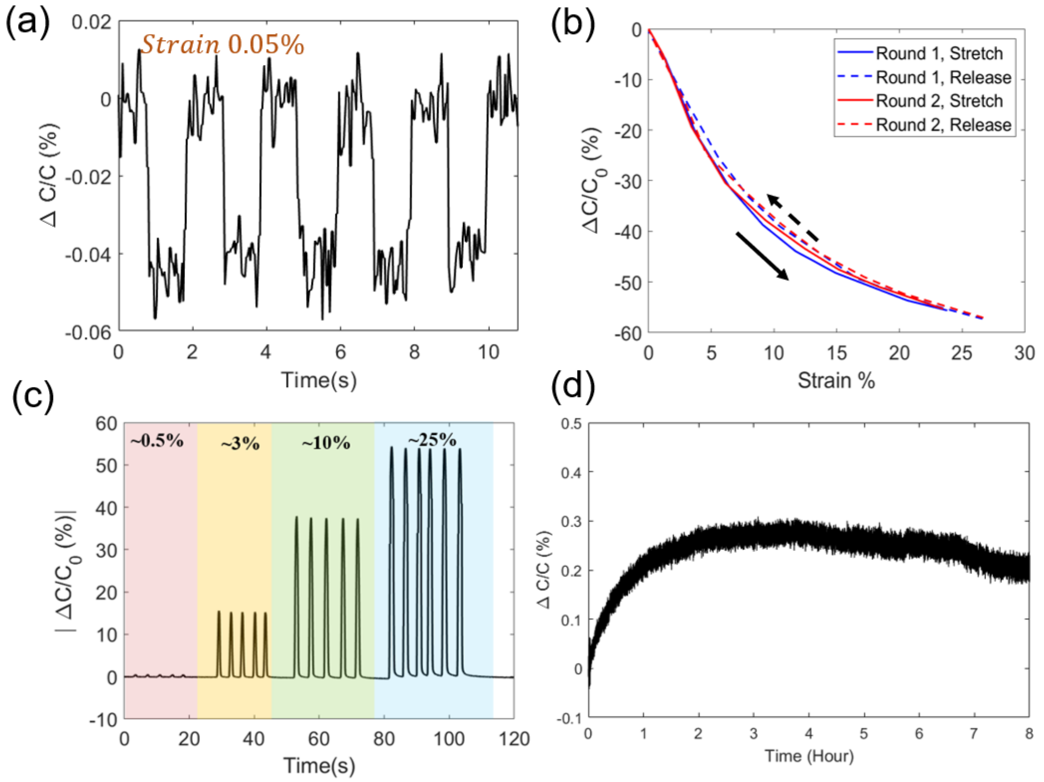

Figure 5-3 Performance Characterization of the Double Coil Fiber. (a), Relative capacitance changes under 0.5 Hz frequency and 0.05% tiny strain. (b), Relative capacitance changes concerning two rounds of stretch (solid line) and release cycles (dashed line). (c), Sensor response exhibited against cyclic strains ranging from 0.5 % to 25 %. (d), Long Time Stability Testing Relative capacitance changes of the stretched sensor as a function of time. Showing less than 0.3% changes after 8 hours testing.

Thanks to the initial large GF, the sensor can be applied to sense miniature strains without pre-stretching. The relative capacitance changes of the sensor against 0.5 Hz square-wave strain as low as 0.05% are plotted in Figure 5-3 (a). The relative capacitance exhibits periodic changes following the applied strain changes. The spike of the plot comes from the noise of the system. The standard deviation of the noise is 0.04 pF, which corresponds to a theoretical capacitive sensitivity of 0.10% (3 σ). Therefore, when operating at small strain range with GF of 5.1, the theoretical resolution of the sensor is 0.02 %. Detailed analysis of the theoretical resolution of sensor is discussed in the supplementary information. The fact that the sensor can work with small strains without pre-stretching enables its application in biomedical applications where the object under monitoring is delicate and can only bare small strains.

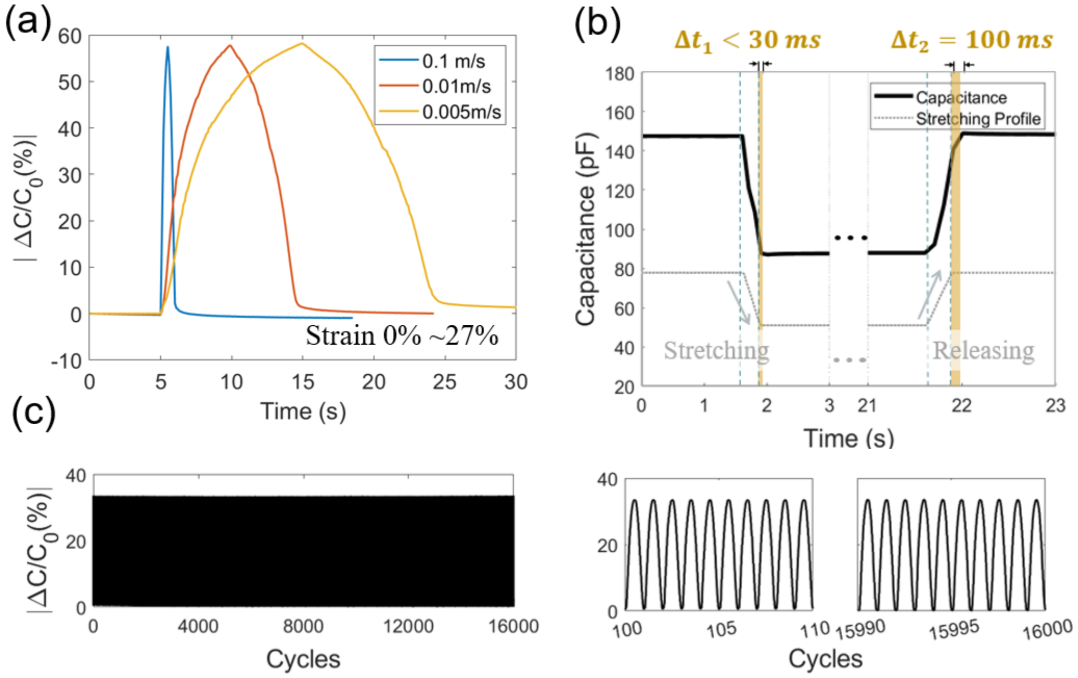

Figure 5-4 (a) Normalized capacitance changes in response to stretch and release strains under various strain rates. (b) Sensor response time measurement involving stretching, holding, and releasing the sensor, illustrating the sensor's quick response and recovery times. (c) Durability assessment of the sensor through over 16,000 cyclic tests, with zoomed-in views of the sensor response during the initial and final 10 cycles.

The stability and hysteresis of the sensor were also investigated. Two rounds of stretching and releasing pattern between 0% to over 25% strain were recorded and the relative capacitance changes are plotted in Figure 5-3 (a). As a comparison, the mechanical response of stretching and releasing cycles is plotted by black traces in Figure 5-1, unlike the large hysteresis observed in the stress-strain graph, the sensor shows small hysteresis and high repeatability in capacitive response. This is due to the fact despite the polyester core is highly viscoelastic, the copper electrodes involve in this sensor has low viscoelasticity and the working principle of the sensor avoid the intrinsic stretching of the electrode material but just straightening of the windings. The high stability of the sensor can also be proved by the time evolution of the capacitance for an overnight test plotted in Figure 5-3 (d). The long-time testing results show the sensor has stable capacitance readouts with neglectable creeping effects. Due to its exceptional stability, the sensor exhibits consistent and distinguishable responses for repeated strains of 0.5%, 3%, 10% 25%, plotted in Figure 5-3 (c). In addition, due to the low viscoelasticity of the sensor, the relative capacitance readouts of the sensor are independent of the stretching and releasing speed. As it is shown in Figure 5-4 (a), the sensor was stretched and released at 0.1 m/s to 0.005 m/s, but the sensor shows a similar level of relative capacitance change. In contrast to highly viscoelastic sensors, the sensor response is remarkably consistent, and the readout remains unaffected by the strain rate, thereby enhancing the reliability of the sensor. Another key advantage brought by the low viscoelasticity is the fast response of the sensor. As it is plotted in Figure 5-4 (b), the sensor response times were extracted by comparing the real time sensor location synchronized with the readout of the sensor. The stretching response time is less than 30 mS (around 4%~23%) and the releasing response time is around 100 mS. The delay of the releasing response time is attributed to the delayed recovery of the coil structure due to the friction between the coil and elastic core. The overall response time is less than 1 second, which qualifies for most the wearable and mechanical monitoring systems. The durability of the sensor was tested by the cycling tests plotted in Figure 5-4 (c). The repeatable relative capacitance was maintained over 16000 cycles between 5% to 15% strain and the zoomed in waveform after 100 cycles and last 10th cycles show the minimum degradation across the cycling tests.

5.3 Sensor Applications

5.3.1 Wearable Applications

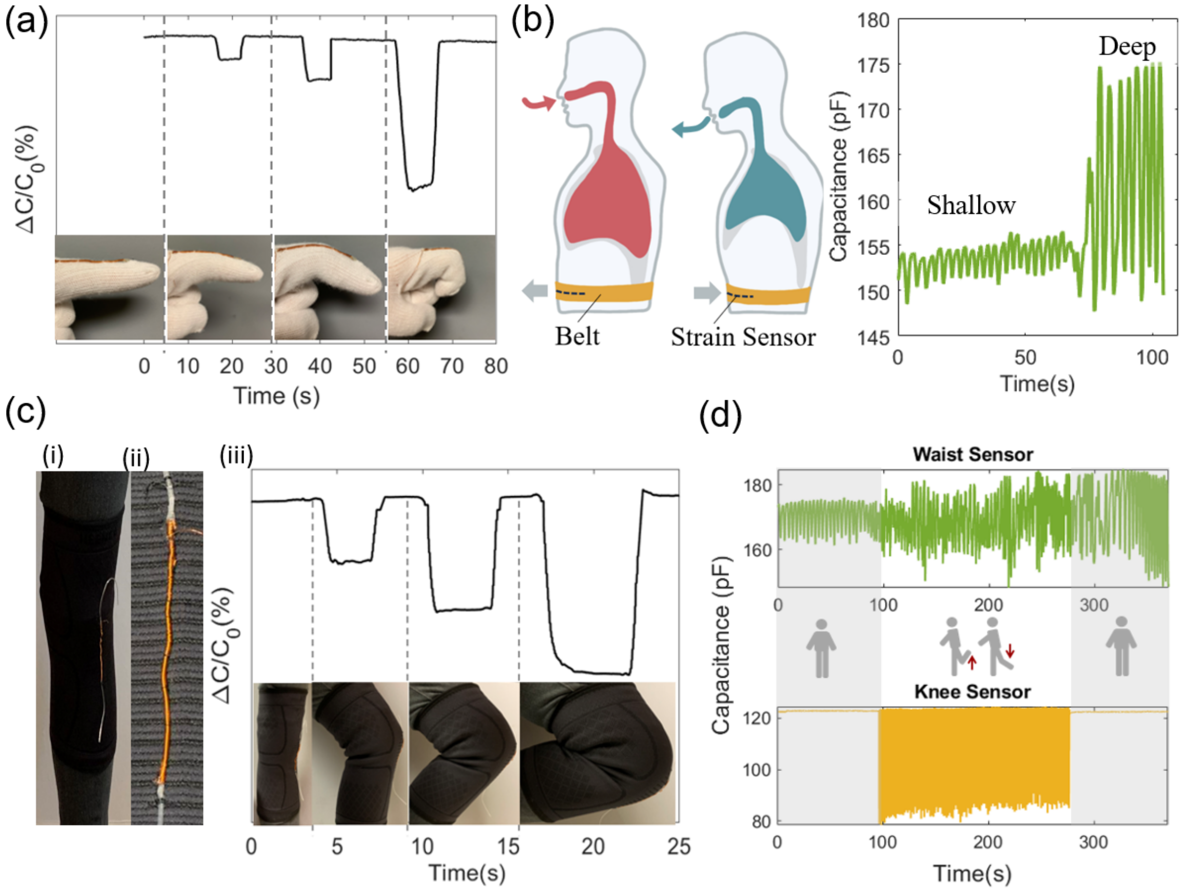

Figure 5-5 Wearable demonstrations of the sensor. (a) Smart gloves demonstration: Capacitance changes of the embedded strain sensor with varying finger bending angles, with inset images displaying different finger gestures while wearing the smart gloves. (b) Breathing monitoring: (i) Schematic illustration of human breathing. (ii) Sensor capacitance changes corresponding to both shallow and deep breathing patterns. (c) (i) Knee bending pattern tracking: image of the strain sensor embedded in a knee support sleeve. (ii) Detailed view of the embedded strain sensor. (iii) Strain sensor readings change as the knee bends at different angles (d) Sport Performance Monitoring: response of the strain sensors attached to the belt and knee during a back-kicking motion, demonstrating the sensor's real-time monitoring capabilities in athletic movements.

By weaving and braiding the stretchable double coil fiber, this sensor can be integrated into several wearable applications. The stretchable strain sensors were stitched onto the index finger of the commercial gloves (Figure 5-5 (a). Thanks to the high sensitivity and stability of the strain sensor, it can monitor the bending gesture of the finger at different angles without deterioration. (Figure 5-5 (a)). By stretching the sensor to a stretchable run storage belt (Figure 5-6) the sensor can monitor the breathing motion in real time ((Figure 5-5 (b)), with distinct signatures between different breathing manners. Deep breathing usually involves more contraction and expansion of the lung, and a much larger relative capacitance change can be observed. Like finger bending monitoring, the knee motion postures can be monitored ((Figure 5-5c)) when the stretchable sensor was integrated into the knee protectors ((Figure 5-5c)). With high stretchability of the sensor, the sensor could follow the knee bending to nearly 180º, and with the fast response speed and high stability, the sensor can monitor the knee bending angles in real time. Together with breathing monitoring, this sensor could be used for health monitoring and sports performance tracking. Shown in (Figure 5-5 (d), a back-kicking exercise motion was recorded both by the breathing sensor and the knee sensor. The breathing data was shown in the top graph, where the breathing amplitude increases as user exercises and more oxygen was needed for the body motion. The knee data recorded the body motion where the user started with a static standing gesture, followed by repeated back-kicking motion and then ended with another standing rest session. The breathing data shows the transition from shallow breathing to deep breathing after the aerobatic movement and the knee data shows the periodic knee bending patterns. The combination of multiple wearable sensors could provide the health monitoring data for the user under test and could potentially give the instructions for the exercise and provide safety warnings.

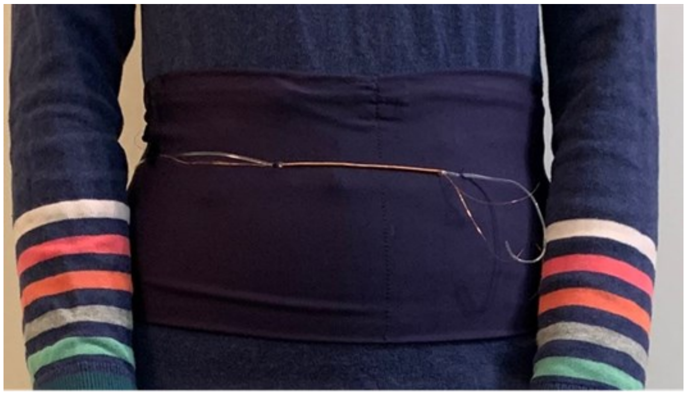

Figure 5-6 Picture of Respiration Sensor A double coil fiber was stitched onto a running storage belt.

5.3.2 Implantable Applications

In addition, this sensor can have other potential applications such as implantable applications and equipment health monitoring. Bladder dysfunction is a prevalent issue impacting over 200 million people globally [136], significantly compromising their quality of life. A strain technique that can effectively monitor the expansion of the bladder is highly desirable. However, the bladder loading process is random and can involve several stages of hold, loading and unload. Most the stretchable sensors suffer high viscoelasticity and can have high hysteresis between measurements which can compromise the precision of the liquid loading level estimation of the bladder monitoring. The stretchable double coil fiber we developed here, however, has low hysteresis and high stability at a held strain and can be a solution to address current issues. To prove the capability of bladder monitoring, double coil fibers with thermal plastic elastomer (SEBS) cores with silicone protected layers were fabricated for testing, and the additional silicone layer was added to improve the sensor's biocompatibility. The strain sensors were knot around the bladder and two electrodes from the same end were connected to the LCR meter (BK Precision 891, Operate at 100 kHz and parallel mode) to monitor the capacitance change in real time (Figure 5-7 (a)). Several sensor locations were tried and the sensor at the upper part of the bladder was picked as it has high sensitivity. The relative capacitance change with two loading processes was plotted in Figure 5-7 (b), showing high repeatability of the sensor responses. The additional loading and holding process was plotted in the bottom figure in Figure 5-7 (b)(ii). The sensor shows fast response as the loading and holding events alternate and the minimum drifting were observed while there is no liquid loading.

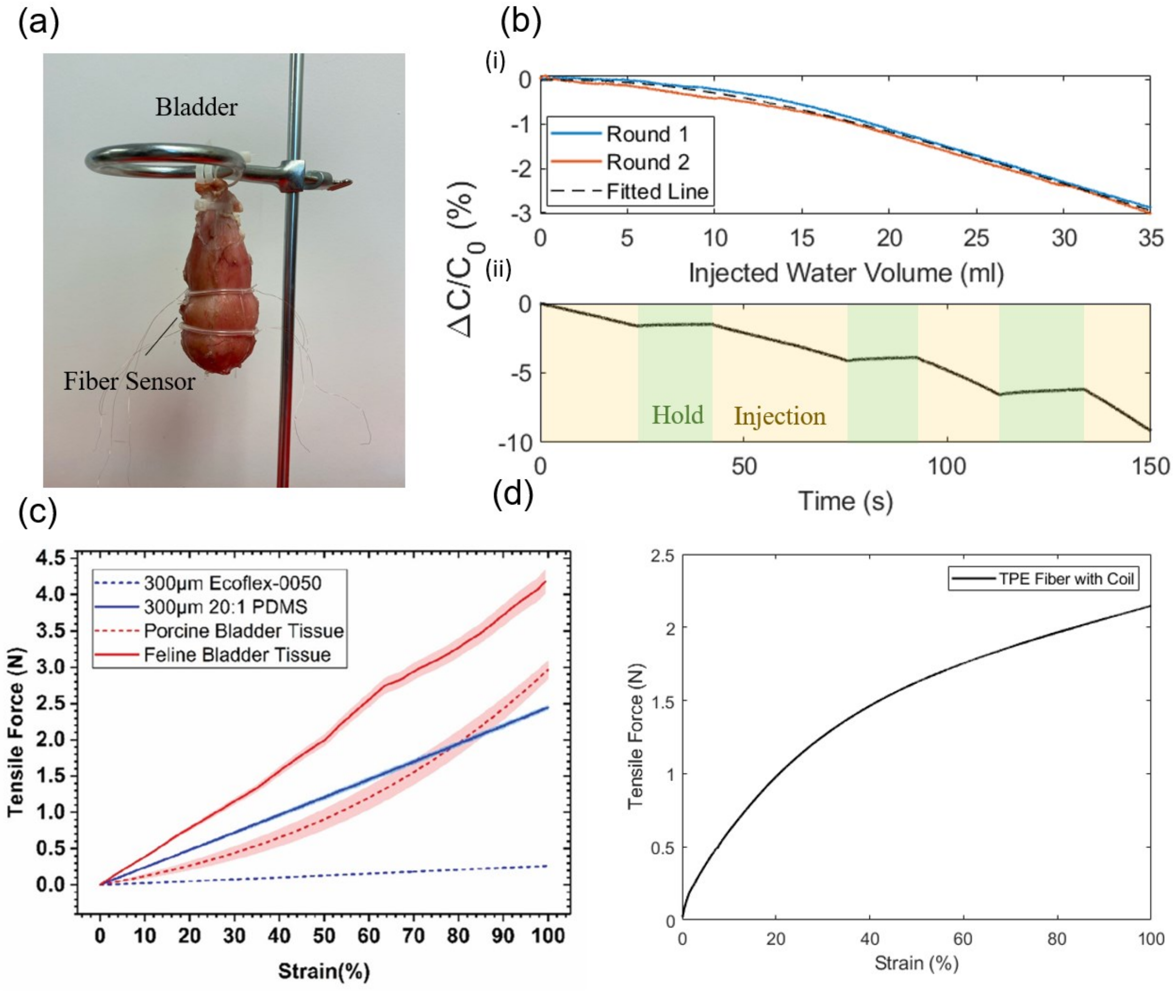

Figure 5-7 (a) Photograph showing the elastic fiber sensor securely looped around a porcine bladder. (b) Relative capacitance changes of the sensor looped around the bladder in response to (i) two rounds of water loading and (ii) alternating water loading and holding patterns. (c) Tensile force as a function of the strain for porcine and feline bladders (d) Tensile force as a function of strain for TPE core double coil fiber.

Additionally, the softness justifications were also investigated. We conducted elasticity measurements on the double coil fiber with TPE cores and compared it with the elasticity of porcine bladder and feline bladder in the literature [137]. In Figure 5-7 (a), with 100% strain, the porcine bladder and feline bladder shows 3 N and 4.2 N respectively where the double coil fiber with TPE core shows a smaller tensile force at 2.2 N. Within 100% strain, the tensile force on the double coil fiber is close to the tensile force on the bladder, therefore the double coil fiber only applied limited amount of force onto the bladder (Figure 5-7 (b)). For future implantable applications, softer material and smaller diameter core can be chosen accordingly to match the softness of the organ undertesting and apply minimum disturbance on the system.

In addition, the sensor can be embedded to structures to monitor the operation conditions of the structure, provide structure lifetime estimations, and share messages of the safety warnings. Life safety ropes are commonly used for rock climbing to provide protection for drop and fall events. However, there will be permanent stretching effects on the life safety rope, and it will compromise its performance. Monitoring the degradation of the life safety rope, i.e., the permanent expansions is important for the life safety rope health monitoring and the sensor proposed here can be applied for this application due to its high stretchability and stability. The sensor was embedded at the core of the life safety rope (Teufelberger) with two ends protruded out of the rope outer layer, which allows the sensor to follow the stretching behavior of the life safety rope. Two eyelet endings were fabricated in the rope to allow it to have good connection with the tester fixtures. The rope with stretchable sensor was tested under several stretch and hold steps with a tensile tester (Instron 5969). The first cycle of the testing with small strain range (0~14%) was used to calibrate the sensor with the ground truth, which are readings from the Instron video extensometer and then the rope was stretched, and the response of the data was plotted with the ground truth in the same plot with the difference of the prediction and the ground truth plotted by the black trace in Figure 5-8. The predicted strain exhibits the real time prediction of the rope strain with minimal lag, high stability at the holding stage and less than 0.5% discrepancy with the reference strain, showing our sensor can provide an accurate prediction on the life safety rope health monitoring.

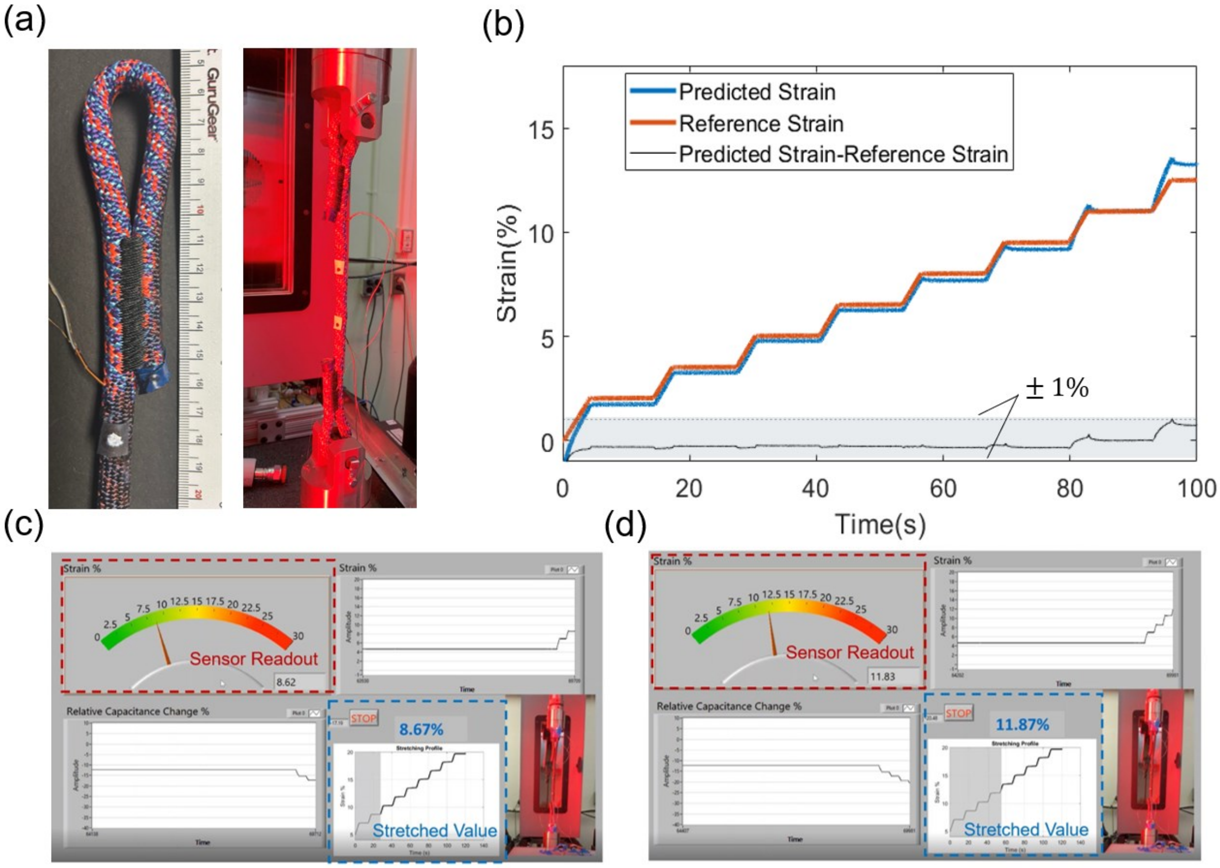

Figure 5-8 (a) (i) Photo displaying the strain sensor braided inside a life safety rope. (ii) Image of the rope stretching lab test setup. (b) Demonstration of the real time measurements on the rope strain. The predicted strain based on relative capacitance measurements is plotted in blue, while the reference strain measured by the video extensometer is plotted in red. The difference between the predicted strain and the true reference strain is plotted in the black trace. (c,d) Software Interface of the Life Safety rope Strain Measurement. Real-time screenshot when the rope was stretched by (c) 8.67%, and (d) 11.87%.

5.4 Experiment Section

Fabrication of the double coil fiber: A pair of insulated copper wires (ELS, 34 AWG, uncoated diameter 160 *μm* were attached to the elastic core. The elastic core was held by the capstan attached to the rotator (ZYT520) and a translational motor (Montomatic motor generator, Electro-craft corporation). The translational motor was tuned to operate at the speed of 7.5 mm/min and the rotator was tuned to synchronize with the translational motor to produce the designed pitch. After the winding process, the two ends of the coil were glued to the elastic core with cyanoacrylate (Loctite, 4310) to allow the double coil structure to follow the elastic core expansions.

Elastic SEBS fiber fabrication: The thermal drawing process is shown in supplementary information. The preform diameter was around 1 inch and the length about 6 inches. The core of the preform is made of poly(styrene-(ethylene-co-butylene)-styrene) triblock copolymer (SEBS, Kraton G1657M), followed by a layer of eCOC and a sacrificial layer of PMMA (Rowland Technologies). The preform was drawn at the temperatures of 150 *℃,* 260 *℃* and 120 *℃*, and the final diameter of the fiber is around 1 mm. The PMMA sacrificial layer was etched by soaking in acetone (Sigma-Aldrich) and peeled off.

Finite element method simulation: Numerical simulations were built to explain the electric field distribution in the densely wound double coil fiber structure and its capacitance changes under different strains. The double coil fiber was simulated with COMSOL Multiphysics (version 6.0). The double coil fiber structure was modelled by a PES core with double coil structure following the parameters given by the experiment measurement. A model with 70 turns (35 turns for each conductor) was simulated, and the diameter of the copper wire is 160 *μm* with the pitch length of 350 *μm/rad*. The FEA model was meshed using the physics controlled free tetrahedra with 458366 vertices. The material of PE elastic core was chosen using the default material library, with the relative permittivity as 3.1. The copper wire was chosen from the library as well, and the electrical properties are as follows: electric conductivity σ= 5.998×10^7 [S/m], relative permittivity ϵ_{rCu} =1, reference resistivity 1.667×10^{-8}. As an approximation for the analytical calculations and FEA models, we assume that the double coil windings are equally spaced. For simplicity, the insulating layer was ignored in both FEA simulations and analytical expressions considering the insulating layer for 34 AWG wires is thin. For the simulation of capacitance under different strains, the double coil structure pitch was stretched uniformly respect to the applied strain and the diameter of the coil structure was assumed to decrease according to the function of: $(\sqrt{l_t^2 - (2\Lambda)^2})/\pi$, where l_t is the length of one turn and Λ is the pitch length after stretching. The elastic total capacitance was calculated through the global evaluation parameter Maxwell capacitance.

Sensor characterizations: (1) Impedance measurement: two electrodes from the same side of the sensor were connected to the Lcur and Hcur port of the impedance analyzer (Keysight 4990A) and the impedance between 1 kHz to 30 MHz was recorded. (2) LCR meter measurement: The electrodes from the tested sensor were connected to the LCR meter (BK precision 891) for the measurement. The LCR meter was set to parameter mode at 100 kHz, 0.5VRMS and fast speed mode. The LCR was connected to the PC and the real time capacitance data was recorded by LabVIEW (National Instrument). (3) Small strain range measurement: one end of the sensor was securely tightened to the stage and the other end of the sensor was attached to a stage driven by micrometer (LTA-HS motorized actuator). The micrometer was programmed to generate 0.5Hz square wave. (4) Theoretical strain sensitivity: we calculated capacitance sensitivity by calculating the 3σ variations of the capacitance when the sensor was held at a constant strain.

Then, the theoretical strain sensitivity is calculated as: $S(\varepsilon) = S(\Delta C/C_0)/GF.$ (5) Hysteresis, strain rate, response time and stability test: the sensor was attached to the programmable linear motor (LinMot 015-5080) and the motor was programmed to the designed waveform. (6) Mechanical responses: Mechanical stress–strain tests and cyclic tests were measured using a dynamic mechanical analysis (TA Instrument, DMA Q800). (7) Relationship between number of turn and lump capacitance: The relationship plotted in Figure 5-5(a) is measured experimentally. We counted the total number of turns of the double coil structures and measured its capacitance after unwinding the coil.

Sensor Demonstrations: (1) Wearable applications: The double coil sensor was stitched to the commercial gloves, running storage belt and knee protector, and the real time data was recorded by the customized LabVIEW script. The finger and the knee bent at different angles and then held the posture for a few seconds for data recordings. The belt with stretchable sensor was placed at the stomach of the subject. The subject was asked to take shallow and deep breath, and the pattern of the capacitive changes are recorded in the same way as the joint movement. (2) Bladder demonstrations: The SEBS core double coil fiber was packaged inside the silicone and then tightened around the porcine bladder. A silicone tubing was inserted into the top of the bladder. Water was pumped into and extracted the bladder through tubing (Pump Tubing, 3-Stop, Tygon® S3™ E-Lab) with peristaltic pump (ISMATEC ISM829B). The loading and extraction speed is ~0.63 ml/s. (4) Life safety rope demonstrations: the double coil fiber was braided into the core of the life safety rope (Teufelberger), with two ends of the fiber protruding through the cladding. The total length of the sample, including the eyelet section, is around 34 cm and the separations between the extruded position is 12.5 cm. The rope passed through the fixture of the tester (Instron 5969) and was stretched under programmed procedures as described in the previous section. The recorded relative capacitance changes were fitted with the reference strain from the video extensometer (Instron, AVE) by a customized MATLAB code using the 3rd order polynomial function. The prediction of strain in real time is achieved by the customized LabVIEW code shown in Figure 5-8(a).

5.5 Conclusions

In summary, we proposed a densely winded double coil strain sensor design that can be scalable fabricated. The strain sensing capabilities of the sensor were characterized, and numerical simulations and analytical expressions were performed to explain its strain sensing capabilities. This strain sensor was demonstrated to feature a high GF (5.1) without pre-strain, which exceeds the geometrical limitations of the capacitive sensor with the GF of 1. An analytical expression was proposed here to understand the helical capacitive sensor sensing mechanisms. The analytical expression is compared with the measurement data and FEA simulations, proving good accuracies. Without the intrinsic stretching on the conductive wires, this sensor has high repeatability, low hysteresis, insensitive to strain rate changes, fast response, and good durability. With the forementioned merits, the sensors were embedded into the fabrics for wearable demonstrations and proved to have capabilities on human sports performance monitoring and health monitoring as it can track the finger, joint and breathing patterns. Additionally, by braiding the sensors to the life safety ropes, the sensors were proved able to track and predict strain of the rope. The strain sensor can also apply as implantable biomedical devices with our demonstration on porcine bladder proves that this sensor can track the bladder expansion in a repeatable and stable manner. This sensor demonstrates good potential in fields including sports performance monitoring, human-machine interface, structural health monitoring and biomedical applications.

Chapter 6 Overview and Future Directions

6.1 Overview

This dissertation explores the potential of multimaterial fiber sensors to measure physical parameters. The idea of developing multimaterial fibers is to explore how the innovation on introducing new fiber materials will expand the sensing capability of pure silica fiber. Under this motivation, two different sensors were explored here:

The first is the magnetostrictive composite fiber for distributive magnetic field sensing applications. The contribution of this work can be summarized in three aspects: (1) Fabrication: taking advantage the thermal drawing process, this sensor combines the high precision and distributive sensing capabilities with the versatility of the polymer material. The scalable thermal drawing process provides a new way for distributive multimaterial optical fiber sensing which potentially applies to more material combinations comparing with the bonding and coating methods. (2) Quasi-distributive Sensing: unlike other magnetostrictive composite fiber sensors and generally most of the magnetic field sensors based on magnetostrictive effects, this sensor uniquely demonstrated distributive sensing capabilities. Here, three FBGs were written in series in the commercially available silica fiber, and we demonstrated three points for magnetic field sensing with the resolution of 0.1 mT. (3) A novel bandwidth-tunable sensor: for the sensor we demonstrated in this work. We demonstrated that the bandwidth of the sensor can be tunable with different boundary conditions. With a fixed boundary condition, the sensor is narrow-banded, and we can potentially tune the resonance peak of the sensor to match the external pre-know field. With a free boundary condition, the sensor is a broadband sensor which can find applications for broadband magnetic field measurement and unknown frequency cases. The strategy of thermally drawing the silica optical fiber sensor to the polymer matrix should not be limited to the example of magnetic field sensing we gave here. Additional work can be explored in the future. The future directions will be listed in the following section.

The second work is a soft and stretchable strain sensor with double coil structure. Independent from the traditional silica fiber, this work focuses on using soft polymer materials to extend the sensor's flexibility. However, the soft polymers often bring up the cost of high hysteresis and delayed response. Therefore, we focus on the improvement of the sensor designs to address those concerns while maintaining sensor's softness and stretchability. The contribution of this work comes in two aspects: (1) First report of analytical expressions for the *densely* wound double coil capacitors. Unlike the findings of the sparsely wounded double coil capacitors as reported in previous work. Our theoretical analysis shows that it is possible to simultaneously increase the sensor's sensitivity and operative stretchability in *densely* wound double coil capacitors. Furthermore, the newly derived analytical expressions, in conjunction with existing theories, collectively form a comprehensive theoretical analysis for double coil capacitors. (2) Scalable fabricated and demonstrated a soft, stretchable strain sensor with low hysteresis, fast response and high stabilities. By coiling stiff electrodes around soft material, the sensor possesses good flexibility and stretchability while minimizing hysteresis effect associated with soft polymer materials. The sensor is shown to have repeatable response under varying strain rates, negligible degradation after over 16,000 cycles, a fast response time of less than 30 milliseconds, and a remarkable strain resolution of 0.015%.

6.2 Future Directions

6.2.1 Magnetostrictive Composite Fiber

Improvements on the Sensitivity

Terfenol-D composite material has been widely investigated on its magnetostrictive effects. Most of the works focus on the randomly distributed composite material, which is called [0-3] material, and bond it with FBGs. [57,138]Several different composite material structures were investigated in the FEA simulations to show the dependency of the magnetostriction effects on the shape. In previous studies using FBGs with magnetostrictive composites, the composite material was randomly distributed.

However, there are a lot of material properties research shows that the chain like structure can significantly increase the overall magnetostrictive responses. Researcher has created chain-like structures inside the magnetostrictive composite material with compression and magnetic field alignment [139,140]. Additionally, some theoretical analysis on the chain like structures is presented in the work, showing that the alignment of the particles can significantly increase the magnetic field strength [85].

Additionally, some of the research works about optical fiber sensors has also investigated the effects of particle alignment. Research works has presented the effects of side alignment of the particles by applying a pair of magnets on each side of the composite material [64]. They proved that with the oriented regions, the sensitivity of the sensor can be improved up to 100%. Additional research shows further improvements in the sensing structure optimization. The attached a metal tube to the FBGs and proved that the metal tube could improve the sensitivity of

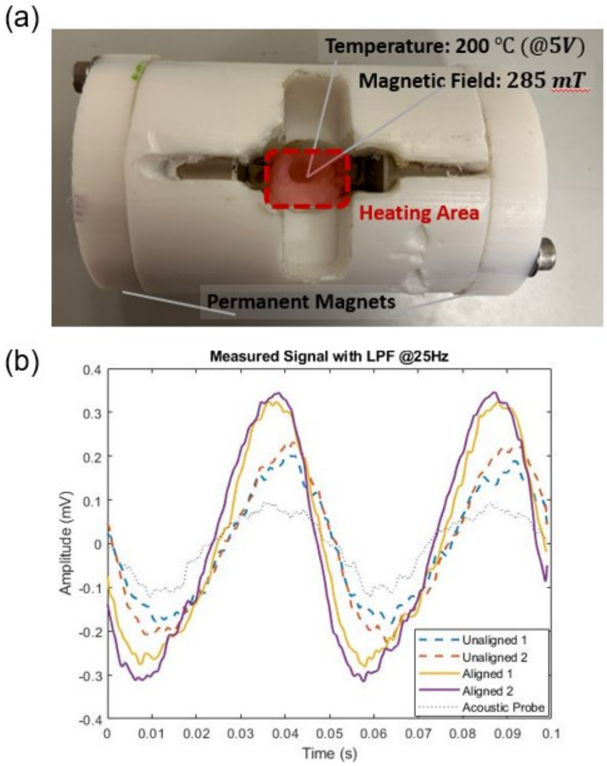

Figure 6-1 (a) The composite material alignment setup (b) Testing results of the block material before and after the alignment.

the sensor by 3.75 times [54]. Combined with the particle alignment in the sensor. The sensitivity of the sensor could be improved more than 3 times [63].

A preliminary investigation of the particle alignment also proved this: A magnetostrictive composite block was attached to the outside layer of the FBG. A prototype of particle alignment setup was fabricated in the lab. Shown in Figure 6-1(a), there is a pair of permanent NdFeB magnets and a heating tube in the center which can heat up the composite material above its glass transition temperature. The softened composite material will allow the particles to align along the chain in a direction.

A polyimide coated fiber with 3^{rd} gratings was embedded into the magnetostrictive block. Additionally, another polyimide coated fiber in series with the previous one was glued on the surface of the magnetostrictive block, to monitor the vibrations and acoustic signals. The comparison of the measured signal was plotted in Figure 6-1 (b). It shows that with the particle alignment, the sensitivity of the fiber can be improved by 50%. Additionally, comparing with the comparison with the acoustic probe, it shows that the vibration of the fiber is not a dominant source of the signal.

Therefore, some future work could focus on the improvement of the sensor sensitivity by particle alignment and improvements on the sensor structures.

Additional Applications of the Magnetic Sensing Fiber

With multiple magnetic sensing points on the fiber, the fiber can serve as a gradiometer to measure the gradient of the magnetic field. A denser array of fiber Bragg gratings can be created to map the magnetic field distributions. Furthermore, the magnetic field distribution can be mapped with intra-grating sensing techniques. Investigation on chirped gratings for intra-grating sensing can be applied to magnetic field sensing.

Another direction is helical magnetostrictive fiber where the soft polymers with and without magnetostrictive particles are drawn. The alternating magnetostrictive fiber could offer chances for better sensitivities and other applications.

Fully Distributive Sensing

In this dissertation's work, a quasi-distributive magnetic field sensor was proposed and tested. However, the idea of integrating the traditional silica fiber sensors into the multimaterial fiber drawing process should be limited to the case of quasi-distributive sensing. A fully distributive strain sensing method can be introduced to demonstrate fully distributive magnetic field sensing capabilities. Examples of fully distributive sensing mechanisms could be Distributive Acoustic Sensing and Brillouin Optical Time-Domain Analysis (BOTDA) can be used in conjunction with the thermal drawing method proposed here. In addition, this thermal drawing method should be limited to the scope of the magnetic field sensing. The composite material opens the options of the active phase for this sensor. This sensor can be applied for other applications such as incorporating pH- responsive material for pH sensing applications.

6.2.2 Double Coil Strain Sensor

Structural and Material Improvement of the Double Coil Fiber

In Chapter 4, we systematically discussed the design considerations of the double coil strain sensors. Although 1 mm and 350 μm^{-1} pitch length, the sensor can be tailored to match the application scenarios. In addition, the material choices of the sensor can also vary according to the application scenarios. We used insulated copper wire as a demonstration, but other conductive materials could be used to make the sensor biocompatible.

Multi-functional Sensing Capabilities

For the sensor we proposed here, we have a ‘two-layer’ structure, where the coil layer was served as the strain sensing component, where the core of the sensor was served purely as the mechanical supports of the strain sensor. However, this stretchable polymer core allows additional complexities. Additional structures can be introduced into the core, such as replacing the core with humidity sensitive materials. As we discussed in Chapter 1, the sensor’s capacitance has limited dependence on the permittivity of the core material. The resistance and permittivity changes of the core material could serve as an additional channel for sensing purposes. Additionally, hallow channels and electrodes can be introduced to the core material to potentially allow drug delivery and electroporation for this sensor [81].

Distributive Sensing Capability of the Strain Sensor

In this dissertation, the double coil fiber sensor was demonstrated for strain sensing capabilities. However, the full length of the sensor here was used, which made the sensor serve as a point sensor, where the strain measured was the overall strain along the entire length of the strain sensor. A distributive strain sensor could be developed based on the same sensor structure, but the capacitance of the sensor was sensed locally. Researchers have demonstrated the distributive sensing capabilities through Frequency Domain Reflectometry by using a Vector Network Analyzer (VNA) [141]. The same sensing interrogation method could potentially be applied to the double coil strain sensor developed here, where the double coil fiber can be viewed as a transmission line as we discussed in previous chapters. The distributive sensing capability is attractive for the sensor's potential application scenarios demonstrated here. For example, the for the wearable applications: the movement and bending of the joints are usually a local effect, with the distributive sensing capabilities, the sensor can plot the deformation of the object in a more precise way. However, as we discussed in the section of the sensor characterizations, the sensor's sensitivity is inversely proportional to the overall capacitance. Therefore, the introduction of the distributive sensing capabilities is at the cost of the sensor's sensitivity.

References

1. J. Hecht, *City of Light: The Story of Fiber Optics*, Sloan Technology (Oxford University Press, 2004).
2. J. M. López-Higuera, *Handbook of Optical Fibre Sensing Technology* (Wiley, 2002).
3. Chennan Hu, Chennan Hu, C. Hu, Z. Yu, Zhihao Yu, and A. Wang, "An all fiber-optic multi-parameter structure health monitoring system.," Optics Express **24**, 20287–20296 (2016).
4. C. Hu, "Two Innovative Applications Combining Fiber Optics and High Power Pulsed Laser: Active Ultrasonic Based Structural Health Monitoring and Guided Laser Micromachining," 150 (n.d.).
5. R. Wang, L. Theis, D. Homa, A. Wang, and G. Pickrell, "Efficient Acoustic-Optical Fiber Coupling with Wire Horn Structure," in *Frontiers in Optics + Laser Science 2023 (FIO, LS) (2023), Paper JM7A.125* (Optica Publishing Group, 2023), p. JM7A.125.
6. Shuo Yang, S. Yang, Daniel Homa, D. S. Homa, H. Heyl, L. Theis, J. Beach, B. Dudding, G. Acord, D. Taylor, G. Pickrell, and A. Wang, "Commercial boiler test for distributed temperature sensor based on wavelength-multiplexed sapphire fiber bragg gratings," **11000**, 1100002 (2019).
7. R. Wang, R. Wang, C. Dou, S. Yang, R. Gnanasambandam, A. Wang, and Z. Kong, "Sub-surface thermal measurement in additive manufacturing via machine learning-enabled high-resolution fiber optic sensing," Nature Communications **Accepted**, (2024).
8. Z. Hileman, J. He, R. Wang, D. Homa, Q. Kong, A. Wang, and G. Pickrell, "Heat-induced Drift Reduction of Time of Flight in Fused Quartz Acoustic Waveguides via Annealing Process," The Journal of the Acoustical Society of America **148**, (2020).
9. J. He, S. Yang, Z. Hileman, R. Wang, D. Homa, G. Pickrell, and A. Wang, "An Acoustic Waveguide With Tight Field Confinement for High Temperature Sensing," IEEE Sensors Journal **20**, 14126–14131 (2020).
10. S. Yang, D. Hu, and A. Wang, "Point-by-point fabrication and characterization of sapphire fiber Bragg gratings," Opt. Lett., OL **42**, 4219–4222 (2017).
11. G. Shi, R. Shurtz, G. Pickrell, A. Wang, and Y. Zhu, "Point-by-point inscribed sapphire parallel fiber Bragg gratings in a fully multimode system for multiplexed high-temperature sensing," Opt. Lett., OL **47**, 4724–4727 (2022).
12. Bo Liu, B. Liu, Bo Liu, B. Liu, Zhihao Yu, Z. Yu, C. Hill, Y. Cheng, Daniel Homa, D. S. Homa, G. Pickrell, and A. Wang, "Sapphire-fiber-based distributed high-temperature sensing system.," Optics Letters **41**, 4405–4408 (2016).
13. G. Keiser, *Optical Fiber Communications*, 4th ed (McGraw-Hill Companies, 2011).
14. H. Bai, S. Li, J. Barreiros, Y. Tu, C. R. Pollock, and R. F. Shepherd, "Stretchable distributed fiber-optic sensors," Science **370**, 848–852 (2020).
15. D. A. Brown, "A symmetric 3x3 coupler based demodulator for fiber optic interferometric sensors," in *Fiber Optic and Laser Sensors IX* (SPIE, 1991), Vol. 1584, p. 328.
16. D. C. Betz, G. Thursby, B. Culshaw, and W. J. Staszewski, "Acousto-ultrasonic sensing using fiber Bragg gratings," Smart Mater. Struct. **12**, 122 (2003).
17. H. Deng, M. Ji, D. Yan, S. Fu, L. Duan, M. Zhang, and Q. Fu, "Towards tunable resistivity–strain behavior through construction of oriented and selectively distributed conductive networks in conductive polymer composites," Journal of Materials Chemistry **2**, 10048–10058 (2014).

18. X. Li, D. Yuanlong, Y. Yu, W. Xinyi, and L. Jingxian, "Microbending optical fiber sensors and their applications," Proceedings of the 2008 International Conference on Advanced Infocomm Technology, ICAIT ’08 (2008).
19. J. Freal, C. Zarobila, and C. Davis, "A microbend horizontal accelerometer for borehole deployment," Journal of Lightwave Technology **5**, 993–996 (1987).
20. P. L. Heinzmann and R. U. Hofstetter, "Temperature Dependence of Plastic Clad Silica (PCS) Fiber Characteristics," in *Optical Fiber Characteristics and Standards* (SPIE, 1986), Vol. 0584, pp. 71–78.
21. S. Hadjiloucas, D. A. Keating, M. J. Usher, W. C. Michie, B. Culshaw, and A. McLean, "Hydrogel based distributed fibre optic sensor for measuring moisture content in soils," in *Conference on Lasers and Electro-Optics Europe (1996), Paper CMM4* (Optica Publishing Group, 1996), p. CMM4.
22. M. P. DeLisa, Z. Zhang, M. Shiloach, S. Pilevar, C. C. Davis, J. S. Sirkis, and W. E. Bentley, "Evanescent Wave Long-Period Fiber Bragg Grating as an Immobilized Antibody Biosensor," Anal. Chem. **72**, 2895–2900 (2000).
23. Y. Liu, S. Li, H. Chen, J. Li, W. Zhang, and M. Wang, "Surface Plasmon Resonance Induced High Sensitivity Temperature and Refractive Index Sensor Based on Evanescent Field Enhanced Photonic Crystal Fiber," Journal of Lightwave Technology **38**, 919–928 (2020).
24. G. Pickrell, W. Peng, W. Peng, and A. Wang, "Random-hole optical fiber evanescent-wave gas sensing.," Optics Letters **29**, 1476–1478 (2004).
25. P. Polynkin, A. Polynkin, N. Peyghambarian, and M. Mansuripur, "Evanescent field-based optical fiber sensing device for measuring the refractive index of liquids in microfluidic channels," Opt. Lett., OL **30**, 1273–1275 (2005).
26. E. Sinchenko, W. E. K. Gibbs, A. P. Mazzolini, and P. R. Stoddart, "The Effect of the Cladding Refractive Index on an Optical Fiber Evanescent-Wave Sensor," Journal of Lightwave Technology **31**, 3251–3257 (2013).
27. P. Di Vita and U. Rossi, "Theory of power coupling between multimode optical fibres," Opt Quant Electron **10**, 107–117 (1978).
28. G. Z. Wang, "Self-referenced fiber optic sensor for microdisplacement measurement," Opt. Eng **34**, 240 (1995).
29. R. O. Cook and C. W. Hamm, "Fiber optic lever displacement transducer," Appl. Opt., AO **18**, 3230–3241 (1979).
30. M. Han, "Theoretical and Experimental Study of Low-Finesse Extrinsic Fabry-Perot Interferometric Fiber Optic Sensors," 142 (n.d.).
31. M. Han and A. Wang, "Mode power distribution effect in white-light multimode fiber extrinsic Fabry-Perot interferometric sensor systems," Opt. Lett., OL **31**, 1202–1204 (2006).
32. J. L. Santos and F. Farahi, *Handbook of Optical Sensors* (CRC Press, 2014).
33. T. Erdogan, "Fiber grating spectra," Journal of Lightwave Technology **15**, 1277–1294 (1997).
34. A. Wang and Z. Yu, *Distributed Fiber Optic Sensor for On-Line Monitoring of Coal Gasifier Refractory Health* (2015), p. 1253131.
35. F. Wang, C. Zhu, C. Cao, and X. Zhang, "Enhancing the performance of BOTDR based on the combination of FFT technique and complementary coding," (n.d.).

36. Lingmei Ma, Bo Dong, B. Dong, A. Wang, Anbo Wang, and Anbo Wang, "Method and apparatus for distributed sensing," (2016).
37. L. Ma, "High-Speed Quasi-Distributed Optical Fiber Sensing Based on Ultra-Weak Fiber Bragg Gratings," 126 (n.d.).
38. K. D. Vos, I. Bartolozzi, E. Schacht, P. Bienstman, and R. Baets, "Silicon-on-Insulator microring resonator for sensitive and label-free biosensing," Opt. Express, OE **15**, 7610–7615 (2007).
39. M. Consales, A. Ricciardi, A. Crescitelli, E. Esposito, A. Cutolo, and A. Cusano, "Lab-on-fiber technology: toward multifunctional optical nanoprobes," ACS Nano **6**, 3163–3170 (2012).
40. V. Beroulle, Y. Bertrand, L. Latorre, and P. Nouet, "Monolithic piezoresistive CMOS magnetic field sensors," Sensors and Actuators A: Physical **103**, 23–32 (2003).
41. J.-W. Jeong, B. Park, H. Keum, S. Kim, J. A. Rogers, and O. Solgaard, "Two-axis MEMS scanner with transfer-printed high-reflectivity, broadband monolithic silicon photonic crystal mirrors," Opt. Express, OE **21**, 13800–13809 (2013).
42. Z. Li, Y. Gu, L. Wang, H. Ge, W. Wu, Q. Xia, C. Yuan, Y. Chen, B. Cui, and R. S. Williams, "Hybrid nanoimprint-soft lithography with sub-15 nm resolution," Nano Lett **9**, 2306–2310 (2009).
43. A. Beyer, A. Godt, I. Amin, C. T. Nottbohm, C. Schmidt, J. Zhao, and A. Gölzhäuser, "Fully cross-linked and chemically patterned self-assembled monolayers," Phys. Chem. Chem. Phys. **10**, 7233–7238 (2008).
44. C. Liberale, G. Cojoc, F. Bragheri, P. Minzioni, G. Perozziello, R. La Rocca, L. Ferrara, V. Rajamanickam, E. Di Fabrizio, and I. Cristiani, "Integrated microfluidic device for single-cell trapping and spectroscopy," Sci Rep **3**, 1258 (2013).
45. A. Cusano, M. Consales, A. Crescitelli, and A. Ricciardi, eds., *Lab-on-Fiber Technology*, Springer Series in Surface Sciences (Springer International Publishing, 2015), Vol. 56.
46. P. Damborský, J. Švitel, and J. Katrlík, "Optical biosensors," Essays Biochem **60**, 91–100 (2016).
47. J. M. Corres, A. Sanz, F. J. Arregui, I. R. Matías, and J. Roca, "Fiber optic glucose sensor based on bionanofilms," Sensors and Actuators B: Chemical **131**, 633–639 (2008).
48. D. Viegas, J. Goicoechea, J. L. Santos, F. M. Araújo, L. A. Ferreira, F. J. Arregui, and I. R. Matias, "Sensitivity Improvement of a Humidity Sensor Based on Silica Nanospheres on a Long-Period Fiber Grating," Sensors **9**, 519–527 (2009).
49. S. Tao, C. B. Winstead, R. Jindal, and J. P. Singh, "Optical-fiber sensor using tailored porous sol-gel fiber core," IEEE Sensors Journal **4**, 322–328 (2004).
50. M. Amjadi, Yong-Jin Yoon, Yong-Jin Yoon, Y.-J. Yoon, and I. Park, "Ultra-stretchable and skin-mountable strain sensors using carbon nanotubes–Ecoflex nanocomposites," Nanotechnology **26**, 375501–375501 (2015).
51. S. Yang, "Femtosecond-Laser-Enabled Fiber-Optic Interferometric Devices," 200 (n.d.).
52. Z. Wang, M. Chen, Y. Zheng, J. Zhang, Z. Wang, J. Yang, Q. Zhang, B. He, M. Qi, H. Zhang, K. Li, and L. Wei, "Advanced Thermally Drawn Multimaterial Fibers: Structure-Enabled Functionalities," Advanced Devices & Instrumentation **2021**, (2021).
53. R. Wang, T. Qiu, Y. Zhang, M. Rein, A. Stolyarov, J. Zhang, G. D. Seidel, B. N. Johnson, A. Wang, and X. Jia, "Fiber-Based Miniature Strain Sensor with Fast Response and Low Hysteresis," Advanced Functional Materials **n/a**, 2403918 (n.d.).

54. J. Peng, S. Zhang, J. Shuhai, Xilong Kang, Hongqiang Yu, Shuming Yang, Shun Wang, and Yaowen Yang, "A highly sensitive magnetic field sensor based on FBG and magnetostrictive composite with oriented magnetic domains," Measurement 110667–110667 (2021).
55. J. Peng, S. Jia, J. Bian, S. Zhang, J. Liu, and X. Zhou, "Recent Progress on Electromagnetic Field Measurement Based on Optical Sensors," Sensors **19**, 2860 (2019).
56. N. Alberto, M. F. Domingues, C. Marques, P. André, and P. Antunes, "Optical Fiber Magnetic Field Sensors Based on Magnetic Fluid: A Review," Sensors **18**, 4325 (2018).
57. S. Quintero, A. Braga, H. Weber, A. Bruno, and J. Araújo, "A Magnetostrictive Composite-Fiber Bragg Grating Sensor," Sensors **10**, 8119–8128 (2010).
58. L. Sun, S. Jiang, and J. R. Marciante, "All-fiber optical magnetic-field sensor based on Faraday rotation in highly terbium-doped fiber," Opt Express **18**, 5407–5412 (2010).
59. N. Li, Y. Chen, C. Zhang, J. Nong, W. Xu, Z. Wang, J. Yang, Y. Yu, and Z. Zhang, "Characterization of Fiber-Optic Vector Magnetic Field Sensors Based on the Magneto-Strictive Effect," Sensors **23**, 7127 (2023).
60. C. Ambrosino, S. Campopiano, A. Cutolo, and A. Cusano, "Sensitivity Tuning in Terfenol-D Based Fiber Bragg Grating Magnetic Sensors," IEEE Sensors J. **8**, 1519–1520 (2008).
61. Z. Shao, X. Qiao, Q. Rong, and A. Sun, "Fiber-optic magnetic field sensor using a phase-shifted fiber Bragg grating assisted by a TbDyFe bar," Sensors and Actuators A: Physical **261**, 49–55 (2017).
62. M. Yang, J. Dai, C. Zhou, and D. Jiang, "Optical fiber magnetic field sensors with TbDyFe magnetostrictive thin films as sensing materials," Opt. Express **17**, 20777 (2009).
63. G. Altin, K. K. Ho, Christopher. P. Henry, and G. P. Carman, "Static properties of crystallographically aligned Terfenol-D∕polymer composites," Journal of Applied Physics **101**, 033537 (2007).
64. A. Dante, J. David, A. Cremonezi, R. Bacurau, C. Carvalho, R. Allil, E. Ferreira, and M. Werneck, "Fiber-Optic Current Sensor Based on FBG and Terfenol-D With Magnetic Flux Concentration for Enhanced Sensitivity and Linearity," IEEE Sensors Journal **20**, 3572–3578 (2020).
65. "Distributed optical fiber dynamic magnetic field sensor based on magnetostriction - PubMed," https://pubmed.ncbi.nlm.nih.gov/24921868/.
66. Y. Du, T. Liu, Z. Ding, K. Liu, B. Feng, and J. Jiang, "Distributed magnetic field sensor based on magnetostriction using Rayleigh backscattering spectra shift in optical frequency-domain reflectometry," Appl. Phys. Express **8**, 012401 (2015).
67. T. Miyazaki and H. Jin, *The Physics of Ferromagnetism* (Springer Science & Business Media, 2012).
68. "Magnetic and Structural Characterization of Fe-Ga Using Kerr Microscopy and Neutron Scattering," https://apps.dtic.mil/sti/citations/ADA596917.
69. W. Heisenberg, "Zur Theorie des Ferromagnetismus," Z. Physik **49**, 619–636 (1928).
70. J. P. Joule, "XVII. On the effects of magnetism upon the dimensions of iron and steel bars," The London, Edinburgh, and Dublin Philosophical Magazine and Journal of Science **30**, 76–87 (1847).
71. A. G. Olabi and A. Grunwald, "Design and application of magnetostrictive materials," Materials & Design **29**, 469–483 (2008).

72. Y. Yamamoto, H. Eda, and J. Shimizu, "Application of giant magnetostrictive materials to positioning actuators," in *1999 IEEE/ASME International Conference on Advanced Intelligent Mechatronics (Cat. No.99TH8399)* (1999), pp. 215–220.
73. C. Lin and Y.-C. Hung, "Viscoelastic effects on the overall responses of Terfenol-D/polymer composites," International Journal of Solids and Structures **262–263**, 112087 (2023).
74. Y.-S. Zhan and C. Lin, "A Constitutive Model of Coupled Magneto-thermo-mechanical Hysteresis Behavior for Giant Magnetostrictive Materials," Mechanics of Materials **148**, 103477 (2020).
75. D.-G. Zhang, M.-H. Li, and H.-M. Zhou, "A general one-dimension nonlinear magneto-elastic coupled constitutive model for magnetostrictive materials," AIP Advances **5**, 107201 (2015).
76. *Handbook of Giant Magnetostrictive Materials* (n.d.).
77. R. Elhajjar, C.-T. Law, and A. Pegoretti, "Magnetostrictive polymer composites: Recent advances in materials, structures and properties," Progress in Materials Science **97**, 204–229 (2018).
78. Y. Pei, D. Fang, and F. Li, "Giant forced volume magnetostriction in polycrystalline Tb0.3Dy0.7Fe1.95 alloys under magnetomechanical loading," Journal of Magnetism and Magnetic Materials **321**, 2783–2787 (2009).
79. R. J. Williams, N. Jovanovic, G. D. Marshall, G. N. Smith, M. J. Steel, and M. J. Withford, "Optimizing the net reflectivity of point-by-point fiber Bragg gratings: the role of scattering loss," Opt. Express, OE **20**, 13451–13456 (2012).
80. M. L. Åslund, N. Jovanovic, N. Groothoff, J. Canning, G. D. Marshall, S. D. Jackson, A. Fuerbach, and M. J. Withford, "Optical loss mechanisms in femtosecond laser-written point-by-point fibre Bragg gratings," Opt. Express, OE **16**, 14248–14254 (2008).
81. Y. Zhang, X. Wu, R. A. Vadlamani, Y. Lim, J. Kim, K. David, E. Gilbert, Y. Li, R. Wang, S. Jiang, A. Wang, H. Sontheimer, D. F. English, S. Emori, R. V. Davalos, S. Poelzing, and X. Jia, "Submillimeter Multifunctional Ferromagnetic Fiber Robots for Navigation, Sensing, and Modulation," Advanced Healthcare Materials **n/a**, 2300964 (n.d.).
82. K. Vedam, "The Elastic and Photoelastic Constants of Fused Quartz," Phys. Rev. **78**, 472–473 (1950).
83. K. Ono, "A Comprehensive Report on Ultrasonic Attenuation of Engineering Materials, Including Metals, Ceramics, Polymers, Fiber-Reinforced Composites, Wood, and Rocks," Applied Sciences **10**, 2230 (2020).
84. R. S. Witte, B. A. Mrowca, and E. Guth, "Propagation of Audiofrequency Sound in High Polymers," Journal of Applied Physics **20**, 481–485 (1949).
85. H. Yin, L. Sun, and J. Chen, "Magneto-elastic modeling of composites containing chain-structured magnetostrictive particles," Journal of the Mechanics and Physics of Solids **54**, 975–1003 (2006).
86. S. Gong, D. T. H. Lai, B. Su, K. J. Si, Z. Ma, L. W. Yap, P. Guo, and W. Cheng, "Highly Stretchy Black Gold E-Skin Nanopatches as Highly Sensitive Wearable Biomedical Sensors," Advanced Electronic Materials **1**, 1400063 (2015).
87. A. Barlian, W.-T. Park, M. Jr, J. Rastegar, and B. Pruitt, "Review: Semiconductor Piezoresistance for Microsystems," Proceedings of the IEEE. Institute of Electrical and Electronics Engineers **97**, 513–552 (2009).

88. S. Egusa, Z. Wang, N. Chocat, Z. Ruff, A. Stolyarov, D. Shemuly, F. Sorin, P. Rakich, J. Joannopoulos, and Y. Fink, "Multimaterial Piezoelectric Fibres," Nature materials **9**, 643–8 (2010).
89. N. Hu, T. Itoi, T. Akagi, T. Kojima, J. Xue, C. Yan, S. Atobe, H. Fukunaga, W. Yuan, H. Ning, Surina, Y. Liu, and Alamusi, "Ultrasensitive strain sensors made from metal-coated carbon nanofiller/epoxy composites," Carbon **51**, 202–212 (2013).
90. W. Obitayo and T. Liu, "A Review: Carbon Nanotube-Based Piezoresistive Strain Sensors," Journal of Sensors **2012**, e652438 (2012).
91. Y. Tong, Z. Feng, J. Kim, J. L. Robertson, X. Jia, and B. N. Johnson, "3D printed stretchable triboelectric nanogenerator fibers and devices," Nano Energy **75**, 104973 (2020).
92. Y. Zhang, X. Li, J. Kim, Y. Tong, E. G. Thompson, S. Jiang, Z. Feng, L. Yu, J. Wang, D. S. Ha, H. Sontheimer, B. N. Johnson, and X. Jia, "Thermally Drawn Stretchable Electrical and Optical Fiber Sensors for Multimodal Extreme Deformation Sensing," Advanced Optical Materials **9**, 2001815 (2021).
93. J. Guo, B. Zhou, R. Zong, L. Pan, X. Li, X. Yu, C. Yang, L. Kong, and Q. Dai, "Stretchable and Highly Sensitive Optical Strain Sensors for Human-Activity Monitoring and Healthcare," ACS Appl Mater Interfaces **11**, 33589–33598 (2019).
94. A. Leber, B. Cholst, J. Sandt, N. Vogel, and M. Kolle, "Stretchable Thermoplastic Elastomer Optical Fibers for Sensing of Extreme Deformations," Advanced Functional Materials **29**, 1802629 (2019).
95. Y. Qu, T. Nguyen-Dang, A. G. Page, W. Yan, T. Das Gupta, G. M. Rotaru, R. M. Rossi, V. D. Favrod, N. Bartolomei, and F. Sorin, "Superelastic Multimaterial Electronic and Photonic Fibers and Devices via Thermal Drawing," Advanced Materials **30**, 1707251 (2018).
96. Dong Wang, D. Wang, B. Sheng, P. Lina, Y. Huang, and Z. Ni, "Flexible and Optical Fiber Sensors Composited by Graphene and PDMS for Motion Detection.," Polymers **11**, 1433 (2019).
97. R. Min, B. Ortega, C. Broadway, X. Hu, C. Caucheteur, O. Bang, P. Antunes, and C. Marques, "Microstructured PMMA POF chirped Bragg gratings for strain sensing," Optical Fiber Technology **45**, 330–335 (2018).
98. I.-L. Bundalo, K. Nielsen, G. Woyessa, and O. Bang, "Long term strain behavior of PMMA-based polymer optical fibers," in *24th International Conference on Optical Fibre Sensors* (SPIE, 2015), Vol. 9634, pp. 1072–1075.
99. L. Lu, Y. Zhou, J. Pan, T. Chen, Y. Hu, G. Zheng, K. Dai, C. Liu, C. Shen, X. Sun, and H. Peng, "Design of Helically Double-Leveled Gaps for Stretchable Fiber Strain Sensor with Ultralow Detection Limit, Broad Sensing Range, and High Repeatability," ACS Applied Materials & Interfaces **11**, 4345–4352 (2019).
100. J. Wu, M. Ziyuan, Z. Hao, J. T. Zhang, P. Sun, M. Zhang, Y. Liu, Y. Cheng, Y. Li, B. Zhong, T. Zhang, T. Zhang, L. Xia, W. Yao, X. Huang, H. Wang, H. Liu, F. Yan, C. E. Hsu, and G. Xing, "Sheath–Core Fiber Strain Sensors Driven by in-Situ Crack and Elastic Effects in Graphite Nanoplate Composites," **2**, 750–759 (2019).
101. Zuoli He, Z. He, G. Zhou, J.-H. Byun, S.-K. Lee, S.-K. Lee, M.-K. Um, B. Park, T. H. Kim, Taehoon Kim, T. Kim, Taehoon Kim, Taehoon Kim, S. B. Lee, and T.-W. Chou, "Highly stretchable multi-walled carbon nanotube/thermoplastic polyurethane composite fibers for ultrasensitive, wearable strain sensors," Nanoscale **11**, 5884–5890 (2019).

102. Y. Wang, J. Hao, Ji Hao, J. Hao, Z. Huang, G. Zheng, K. Dai, C. Liu, and C. Shen, "Flexible electrically resistive-type strain sensors based on reduced graphene oxide-decorated electrospun polymer fibrous mats for human motion monitoring," Carbon **126**, 360–371 (2018).

103. Y. Li, B. Zhou, G. Zheng, X. Liu, T. Li, C. Yan, C. Cheng, K. Dai, C. Liu, C. Shen, and Z. Guo, "Continuously prepared highly conductive and stretchable SWNT/MWNT synergistically composited electrospun thermoplastic polyurethane yarns for wearable sensing," J. Mater. Chem. C **6**, 2258–2269 (2018).

104. Z. Liu, D. Qi, G. Hu, H. Wang, Y. Jiang, G. Chen, Y. Luo, X. J. Loh, B. Liedberg, and X. Chen, "Surface Strain Redistribution on Structured Microfibers to Enhance Sensitivity of Fiber-Shaped Stretchable Strain Sensors," Adv. Mater. **30**, 1704229 (2018).

105. S. Chen, H. Liu, S. Liu, P. Wang, S. Zeng, L. Sun, and L. Liu, "Transparent and Waterproof Ionic Liquid-Based Fibers for Highly Durable Multifunctional Sensors and Strain-Insensitive Stretchable Conductors," ACS Appl. Mater. Interfaces **10**, 4305–4314 (2018).

106. Z. Tang, S. Jia, F. Wang, F. Wang, C. Bian, Y. Chen, Y. Wang, B. Li, B. Li, L. Bo, and Bo Li, "Highly Stretchable Core–Sheath Fibers via Wet-Spinning for Wearable Strain Sensors," ACS Applied Materials & Interfaces **10**, 6624–6635 (2018).

107. J. Zhang, Y. Cao, M. Qiao, L. Ai, K. Sun, Q. Mi, S. Zang, Y. Zuo, X. Yuan, and Q. Wang, "Human motion monitoring in sports using wearable graphene-coated fiber sensors," Sensors and Actuators A: Physical **274**, 132–140 (2018).

108. S. Choi, K. Yoon, S. Lee, H. J. Lee, J. Lee, D. W. Kim, M.-S. Kim, Min Seok Kim, Min Seok Kim, T. Lee, and C. Pang, "Conductive Hierarchical Hairy Fibers for Highly Sensitive, Stretchable, and Water-Resistant Multimodal Gesture-Distinguishable Sensor, VR Applications," Advanced Functional Materials **29**, 1905808 (2019).

109. Z. Cao, R. Wang, T. He, F. Xu, F. Xu, J. Sun, and J. Sun, "Interface-Controlled Conductive Fibers for Wearable Strain Sensors and Stretchable Conducting Wires.," ACS Applied Materials & Interfaces **10**, 14087–14096 (2018).

110. X. Wang, H. Sun, X. Yue, Y. Yu, G. Zheng, K. Dai, C. Liu, and C. Shen, "A highly stretchable carbon nanotubes/thermoplastic polyurethane fiber-shaped strain sensor with porous structure for human motion monitoring," Composites Science and Technology **168**, 126–132 (2018).

111. J. Eom, R. Jaisutti, H. Lee, H. H. Lee, W. Lee, J. S. Heo, J. Y. Lee, J.-Y. Lee, S. K. Park, Y.-H. Kim, Y.-H. Kim, and Yong-Hoon Kim, "Highly Sensitive Textile Strain Sensors and Wireless User-Interface Devices Using All-Polymeric Conducting Fibers," ACS Applied Materials & Interfaces **9**, 10190–10197 (2017).

112. M. Amjadi, K.-U. Kyung, I. Park, and M. Sitti, "Stretchable, Skin-Mountable, and Wearable Strain Sensors and Their Potential Applications: A Review," Advanced Functional Materials **26**, 1678–1698 (2016).

113. Z. Liu, S. Fang, F. A. Moura, J. Ding, N. Jiang, J. Di, M. Zhang, X. Lepró, D. S. Galvao, C. S. Haines, N. Yuan, N. Yuan, S. Yin, D. W. Lee, D. W. Lee, R. Wang, H. Wang, W. Lv, C. Dong, R. C. Zhang, M. Chen, Q. Yin, Q. Yin, Y. T. Chong, Rui Zhang, R. Zhang, X. Wang, X. Wang, M. D. Lima, R. Ovalle-Robles, D. Qian, H. Lu, and R. H. Baughman, "Hierarchically buckled sheath-core fibers for superelastic electronics, sensors, and muscles," Science **349**, 400–404 (2015).

114. J. Lee, S. J. Ihle, G. S. Pellegrino, H. Kim, J. Yea, C.-Y. Jeon, H.-C. Son, C. Jin, D. Eberli, F. Schmid, B. L. Zambrano, A. F. Renz, C. Forró, H. Choi, K.-I. Jang, R. Küng, and J. Vörös, "Stretchable and suturable fibre sensors for wireless monitoring of connective tissue strain," Nat Electron **4**, 291–301 (2021).
115. J. Shintake, Y. Piskarev, S. Jeong, and D. Floreano, "Ultrastretchable Strain Sensors Using Carbon Black-Filled Elastomer Composites and Comparison of Capacitive Versus Resistive Sensors," Advanced Materials Technologies **3**, 1700284 (2017).
116. C. B. Cooper, K. Arutselvan, Y. Liu, D. P. Armstrong, Y. Lin, M. R. Khan, J. Genzer, and M. D. Dickey, "Stretchable Capacitive Sensors of Torsion, Strain, and Touch Using Double Helix Liquid Metal Fibers," Advanced Functional Materials **27**, 1605630 (2017).
117. L. Yu, Y. Feng, D. S/O M Tamil Selven, L. Yao, R. H. Soon, J. C. Yeo, and C. T. Lim, "Dual-Core Capacitive Microfiber Sensor for Smart Textile Applications," ACS Appl. Mater. Interfaces **11**, 33347–33355 (2019).
118. A. Frutiger, J. T. Muth, D. M. Vogt, Y. Menguc, Yiğit Mengüç, A. B. Campo, A. D. Valentine, C. J. Walsh, and J. A. Lewis, "Capacitive Soft Strain Sensors via Multicore–Shell Fiber Printing," Advanced Materials **27**, 2440–2446 (2015).
119. R. Nur, N. Matsuhisa, Z. Jiang, M. O. G. Nayeem, T. Yokota, and T. Someya, "A Highly Sensitive Capacitive-type Strain Sensor Using Wrinkled Ultrathin Gold Films," Nano Lett **18**, 5610–5617 (2018).
120. H. Xu, Y. Lv, D. Qiu, Y. Zhou, H. Zeng, and Y. Chu, "An ultra-stretchable, highly sensitive and biocompatible capacitive strain sensor from an ionic nanocomposite for on-skin monitoring," Nanoscale **11**, 1570–1578 (2019).
121. R. Wang, L. Theis, Y. Zhang, X. Jia, and A. Wang, *Magneto-Strictive Composite Fiber for Quasi-Distributed Magnetic Field Sensing* (2023).
122. A. Massarini and M. K. Kazimierczuk, "Self-capacitance of inductors," IEEE Transactions on Power Electronics **12**, 671–676 (1997).
123. S. Wang, Y. Yang, F. C. Lee, and Q. Li, "Single Stage EMI Filter for Server Power Supply," in *2020 IEEE Applied Power Electronics Conference and Exposition (APEC)* (2020), pp. 2384–2391.
124. V. Fowler, "Analysis of helical transmission lines by means of the complete circuit equations," Trans. IRE Prof. Group Antennas Propagat. **2**, 132–143 (1954).
125. F. Lee, S. Wang, and Q. Li, "Next Generation of Power Supplies-Design for Manufacturability," IEEE Journal of Emerging and Selected Topics in Power Electronics **PP**, 1–1 (2020).
126. A. Massarini, "Analytical Approach to the Calculation of Parasitic Capacitance Between Winding Turns," in *2018 IEEE 4th International Forum on Research and Technology for Society and Industry (RTSI)* (2018), pp. 1–4.
127. C. M. de Miranda and S. F. Pichorim, "A Self-Resonant Two-Coil Wireless Power Transfer System Using Open Bifilar Coils," IEEE Transactions on Circuits and Systems II: Express Briefs **64**, 615–619 (2017).
128. H. Souri, H. Banerjee, A. Jusufi, N. Radacsi, A. A. Stokes, I. Park, M. Sitti, and M. Amjadi, "Wearable and Stretchable Strain Sensors: Materials, Sensing Mechanisms, and Applications," Advanced Intelligent Systems **2**, 2000039 (2020).
129. O. Atalay, A. Atalay, J. Gafford, H. Wang, R. Wood, and C. Walsh, "A Highly Stretchable Capacitive-Based Strain Sensor Based on Metal Deposition and Laser Rastering," Advanced Materials Technologies **2**, 1700081 (2017).

130. Aaron P. Gerratt, A. P. Gerratt, H. O. Michaud, and S. P. Lacour, "Elastomeric Electronic Skin for Prosthetic Tactile Sensation," Advanced Functional Materials **25**, 2287–2295 (2015).
131. D. J. Lipomi, M. Vosgueritchian, B. C.-K. Tee, S. L. Hellstrom, J. A. Lee, C. H. Fox, and Z. Bao, "Skin-like pressure and strain sensors based on transparent elastic films of carbon nanotubes," Nature Nanotechnology (2011).
132. L. Viry, A. Levi, M. Totaro, A. Mondini, V. Mattoli, B. Mazzolai, and L. Beccai, "Flexible Three-Axial Force Sensor for Soft and Highly Sensitive Artificial Touch," Advanced Materials **26**, 2659–2664 (2014).
133. X. Wang, X. Liú, and D. Schubert, "Highly Sensitive Ultrathin Flexible Thermoplastic Polyurethane/Carbon Black Fibrous Film Strain Sensor with Adjustable Scaffold Networks," Nano-Micro Letters **13**, (2021).
134. W. D. Pilkey, D. F. Pilkey, and Z. Bi, *Peterson's Stress Concentration Factors* (John Wiley & Sons, 2020).
135. J. Zhou, Y. Xu, M. A. Lopez, L. Farbaniec, S. Patsias, D. Macdougall, J. Reed, N. Petrinic, D. Eakins, C. Siviour, and A. Pellegrino, "The mechanical response of commercially pure copper under multiaxial loading at low and high strain rates," International Journal of Mechanical Sciences **224**, 107340 (2022).
136. M. K. Kim, S. Lee, I. Yoon, G. Kook, Y. S. Jung, S. S. M. Bawazir, C. Stefanini, and H. J. Lee, "Polypyrrole/Agarose Hydrogel-Based Bladder Volume Sensor with a Resistor Ladder Structure," Sensors **18**, 2288 (2018).
137. D. Yan, T. M. Bruns, Y. Wu, L. L. Zimmerman, C. Stephan, A. P. Cameron, E. Yoon, and J. P. Seymour, "Ultra-compliant carbon nanotube direct bladder device," Adv Healthc Mater **8**, e1900477 (2019).
138. Q. Liu and X. He, "Thermal Analysis of Terfenol-D Rods with Different Structures," Micromachines **14**, 216 (2023).
139. B. Li, T. Zhang, Y. Wu, and C. Jiang, "High-performance magnetostrictive composites with large particles volume fraction," Journal of Alloys and Compounds **805**, 1266–1270 (2019).
140. T. A. Duenas and G. P. Carman, "Particle distribution study for low-volume fraction magnetostrictive composites," Journal of Applied Physics **90**, 2433–2439 (2001).
141. L. Yu, S. Parker, H. Xuan, Y. Zhang, S. Jiang, M. Tousi, M. Manteghi, A. Wang, and X. Jia, "Flexible Multi-Material Fibers for Distributed Pressure and Temperature Sensing," Advanced Functional Materials **30**, 1908915 (2020).